Laser-induced dynamics of liquid tin microdroplets

Dmitry Kurilovich

VRIJE UNIVERSITEIT

Laser-induced dynamics of liquid tin microdroplets

ACADEMISCH PROEFSCHRIFT

ter verkrijging van de graad Doctor
aan de Vrije Universiteit Amsterdam,
op gezag van de rector magnificus
prof.dr. V. Subramaniam,
in het openbaar te verdedigen
ten overstaan van de promotiecommissie
van de Faculteit der Bètawetenschappen
op donderdag 4 april 2019 om 13.45 uur
in de aula van de universiteit,
De Boelelaan 1105

door

Dmitry Aleksandrovich Kurilovich

geboren te Pastavy, Belarus

promotoren:	prof.dr. W.M.G. Ubachs
	prof.dr.ir. R.A. Hoekstra
copromotor:	dr. O.O. Versolato

This thesis was approved by the members of the reviewing committee:

prof.dr. J.F. de Boer (Vrije Universiteit Amsterdam)
prof.dr. D. Bonn (University of Amsterdam)
prof.dr. P. Mora (École Polytechnique, France)
prof.dr. J.H. Snoeijer (University of Twente)
prof.dr. W.J. van der Zande (Radboud University and ASML)

The research reported in this thesis was carried out at the Advanced Research Center for Nanolithography (ARCNL), a public-private partnership between the University of Amsterdam (UvA), Vrije Universiteit Amsterdam (VU Amsterdam), the Netherlands Organization for Scientific Research (NWO), and the semiconductor equipment manufacturer ASML.

Cover: (Front) A shadowgraph image (front view corrected for the parallax angle) of a tin microdroplet a few μs after nanosecond laser pulse impact. (Back) Stroboscopic time series of expanding tin microdroplets, representing two types of laser targets obtained with laser pre-pulses (impacting from the left) of different pulse length relevant for plasma sources of extreme ultraviolet light.

ISBN: 978-94-92323-27-9

Contents

Chapter 1

Introduction

Micro-electronic devices are the core of many tools we use in our everyday life. Their performance has been pushed by the semiconductor industry over past decades since the invention of the transistor (Nobel Prize for Shockley, Bardeen and Brattain in 1956) and its development into an integrated circuit (Nobel Prize for Alferov, Kroemer and Kilby in 2000). The development of shrinking the sizes of electronic elements leading to ever denser packing of integrated circuitry led Gordon Moore, founder of Intel company, in 1965 to the observation and prediction that the number of transistors on a microelectronic chip doubles every year [1]. This is represented in Fig. 1.1(left). In 1975 the statement was revised to a doubling every two years [2].

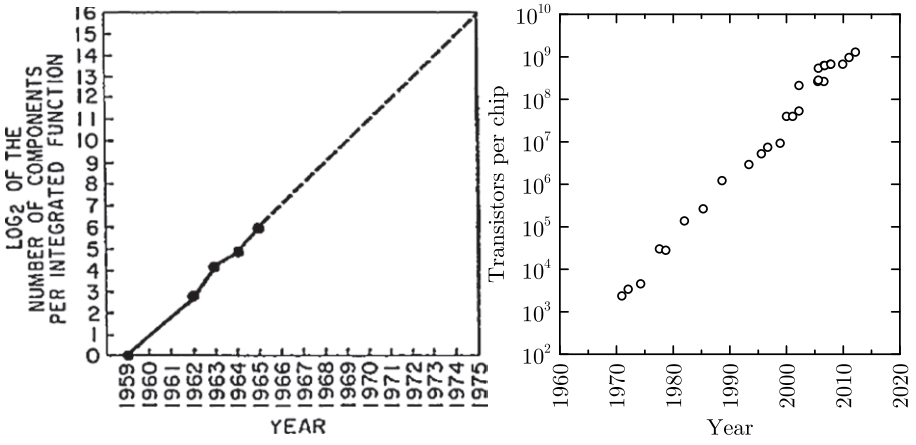

FIGURE 1.1: A trend of the amount of components per integrated circuit (left) predicted by G. Moore in 1965 (reprinted from Ref. [1]) and (right) as observed over the past five decades (adapted from Ref. [3]).

Moore's prediction that this rapid development would sustain at the same pace over years to come has become known as Moore's law. This empirical law evolved from a prediction to a driving principle for the chip-manufacturing industry, and eventually even to a roadmap, the International Technology Roadmap for Semiconductors, with participation of industry associations on three different continents [3, 4]. Indeed, as is shown in Fig. 1.1(right) Moore's law has been kept alive over the past five decades [3, 5]. A sustained increase of the density of elements on computer chips remains a challenge to industry and ignites technologies and scientific developments beyond the state-of-the-art.

One of the crucial processes underlying this trend is photolithography [6, 7]. It is a photochemical process where a coated silicon wafer covered with a layer of photoresist is exposed to light through a mask with a specific structure [8]. This structure corresponds to a future circuit on a layer of a semiconductor chip. After the exposure and subsequent development, the photoresist forms a planar structure that leaves only a certain area on the wafer exposed to the next steps, such as etching, ion implantation, and deposition. In this chain of repetitive manufacturing steps (see Fig. 1.2) photolithography plays a key role by ensuring the transfer of desired structures on the nanometer scale. The Critical Dimension (CD), or resolution, is the minimum feature size that can be printed in the photoresist. It is conventionally written as:

$$\mathrm{CD} = k_1 \times \frac{\lambda}{\mathrm{NA}}. \tag{1.1}$$

Here, k_1, typically 0.3–0.4, is a parameter that depends on the characteristics of a specific lithography process, such as the photoresist, type of the mask and its pattern; λ is the wavelength of the exposing light, and NA is the numerical aperture of the exposure tool. Steady progress in shrinking the minimum size

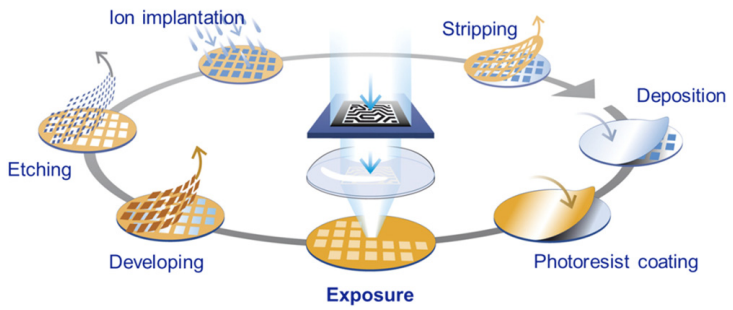

FIGURE 1.2: Main manufacturing steps of a semiconductor device (reproduced from Ref. [9]).

of the elements on a chip is supported by improvement of all three parameters. The wavelength went through several steps of reduction: 365 nm, 248 nm, 193 nm, and, the most recent one, 13.5 nm [10]. The photolithography process and the chemical species of the photoresist depend on the wavelength of the light chosen to expose the wafer. For each system with a specific wavelength, the numerical aperture experienced several improvement steps as well. For example, for the 193-nm-wavelength systems, the latest big step was made by introducing the immersion technique with NA>1, which made it possible to produce modern chips with feature sizes down to 10 nm.

EUV lithography

After over 20 years of research and development, lithography in the extreme-ultraviolet wavelength range (EUVL) is now being used by the main semiconductor manufacturers [11]. In 2018, EUVL became possible for high-volume manufacturing (HVM) after passing the threshold of EUV light source power of 250 Watts [12]. State-of-the-art sources of extreme-ultraviolet light employ tin plasma as an emitting medium in which a certain charge state population is reached by interaction with a high-intensity 10-μm-wavelength pulse from a CO_2 laser [13]. The produced light with a spectral peak at 13.5 nm is collected and transferred by means of Mo/Si multilayer mirrors. Due to their limited reflectance (max $\sim 70\%$) and a small bandwidth ($\pm 1\%$), only a small fraction of the produced light can be effectively used for lithography. After bouncing from several mirrors that are needed to image and demagnify the pattern of the mask (reticle), the intensity of the EUV radiation drops significantly before it reaches the photoresist layer on the wafer. A continuous demand for ever more powerful light sources provides an ongoing challenge to industry as well as to the scientific community. Profound understanding of the atomic plasma processes during the laser-matter interaction is crucial to increase the conversion efficiency (CE) of the drive laser energy into EUV radiation in the aforementioned "in-band" 2% bandwidth around 13.5 nm.

Another challenge is the lifetime of the source, which is affected by many parameters, but primarily by the degradation of the first mirror. This first, "collector" mirror focuses the in-band EUV light that is emitted in the laser-facing hemisphere, to the other optic elements inside the lithography tool. Its location in the vicinity of the plasma could potentially result in very fast contamination caused by both neutral and charged particles (debris) originating from the laser-matter interaction [13–16]. A continuous flow of hydrogen gas is directed inside the vessel in order to capture the high influx of tin debris. By exchanging the momentum in multiple collisions with energetic tin ions, the hydrogen molecules slow down the ionic debris and redirect it toward the vacuum exhaust. Hydrogen was chosen as a compromise between low stopping power per particle (in view of its low atomic mass) and the

high transmissivity for EUV light. Moreover, hydrogen radicals formed near the primary plasma can etch away any tin deposited on the collector mirror, forming a stannane gas (SnH_4) that should also be removed from the collector mirror before its dissociation. Another approach, a magnetic guidance technique has also shown its benefit in redirecting high-energy tin ions from the mirror. However, this requires high magnetic fields and a hydrogen flow is still needed for debris mitigation [17].

In case of laser interaction with a solid tin target, a significant amount of tin is ejected as debris particles harmful for the source performance [17, 18]. Therefore, to reduce contamination of the EUV source, several other geometries for tin targets were explored, delivering reduced amounts of redundant "fuel". Target concepts as sprays, rotating cylinders or disks, and tin jets were tested [19]. However, it was shown that the most practical way of delivering tin is in the form of mass-limited spherical microdroplet targets. Limiting the available tin mass interacting with the laser pulse by providing the tin in small, isolated droplets results in a significant reduction of debris inside the source vessel.

For a stable and efficient interaction with the laser pulse the droplets, obtained by a controlled coalescence of small droplets originating from a breakup of a liquid tin jet, should be produced with reproducible temporal and spatial characteristics. Moreover, the laser-droplet interaction event can affect the shape and position of the subsequent droplet, which in turn may result in a reduction of the produced EUV light. It was found that the droplet stream should have a large velocity ($\sim$100 m/s) in order to ensure high power operation at the required high, 50-kHz repetition rate [18]. All these requirements have significant impact on the design of the EUV source.

The high-power CO_2 lasers that were chosen to drive the tin plasma in EUV light sources have a wavelength of 10.6 μm. The main reasons for that were high conversion efficiency of the laser light of this wavelength into the desired 13.5($\pm$1%) nm, and availability of such high-power laser for industrial applications. To provide an optimum coupling between the drive laser light and the tin mass, the spherical liquid droplet is typically first deformed into some suitable target shape. For this purpose, in current industrial systems a separate pulse, a so called "pre-pulse" is used [18] (see Fig. 1.3). This pulse, with a duration of a few tens of nanoseconds at an intensity sufficient to ablate a small fraction of the tin droplet ($\sim$1%), is capable of producing tin plasma on the laser-facing side of the droplet. Formed within the duration of the laser pulse, this plasma eventually expands, giving a rise to a pressure kick to the remaining part of the droplet [20–22]. Such an impact expands the droplet and accelerates its center-of-mass away from the laser interaction zone. By choosing the appropriate laser intensity, the droplet can be expanded into a thin disk-like shape that in a couple of microseconds after

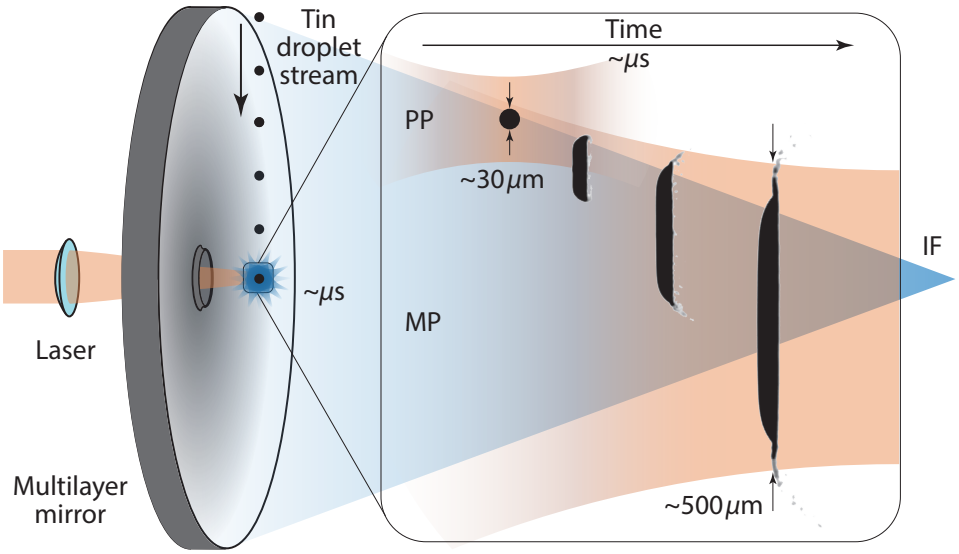

FIGURE 1.3: Simplified schematics of the laser-droplet interaction in EUV light sources. A spherical microdroplet hit by a laser pre-pulse (PP). The droplet is propelled and reshaped into a (tilted) disk target suitable for the main-pulse laser irradiation (MP). Highly-ionized, EUV emitting tin plasma is created as a result of the high energy main-pulse laser impact. A multilayer mirror (left) collects the light emitted in the laser-facing hemisphere ($\sim 2\pi$ solid angle) and focuses it at the intermediate focus (IF).

the pre-pulse matches the beam size of the second, main laser pulse ($\sim$500 μm). The main pulse carries intensity ($\sim 10^{11}$ W/cm^2) that is optimal for producing ion charge states of tin that efficiently contribute to the light emission around 13.5 nm (Sn^{8+}–Sn^{14+}) [23].

The EUV sources currently used by the semiconductor manufacturers utilize pre-pulses of 10-μm wavelength and duration of several tens of nanoseconds produced by the same CO_2 laser system that produces main pulses. More than 20 kW of the input laser power is needed to produce EUV light at the level for HVM [18]. Therefore, the industry considers using separate, more efficient laser systems for pre-pulse, thus leaving all CO_2-laser power for EUV generation. One of the possible substitutes is a solid-state laser system emitting light at 1-μm wavelength. Due to the shorter wavelength, the ablation of tin droplets is more efficient. There are several other advantages of using separate laser system for pre-pulses, such as separate beam paths, meaning better light isolation between pre-pulse and main pulse, and the capability of a simplified spatial and temporal shaping. Moreover,

it becomes possible to use a different pulse duration.

Recent developments [17, 18] produced tentative evidence for improved source performance when replacing the ns-pre-pulse with a ps-pulse laser. The physics dramatically changes switching from nanosecond to these picosecond laser pre-pulses. Such very short laser pulses can produce strong shock waves that propagate in the tin droplet, and focus right in the center of the droplet, where they lead to explosive cavitation and spallation with absolutely spectacular results [24–30]. Such volumetric, finely dispersed target shapes are expected to be able to provide benefits regarding main pulse absorptivity and EUV emissivity when compared to the disk-type shapes created by nanosecond laser pulses.

This broad scope of pre-pulse physics, with the aim of producing suitable target shapes in tin microdroplet-based laser-driven plasma sources, provides an ideal environment for combining industrial innovations with attractive scientific questions that range from the physics of dense plasma to fluid dynamic deformations.

Thesis outline and summary

This work aims to advance the understanding of the underlying physics of the laser target formation in state-of-the-art and future laser-produced plasma sources of EUV light. An experimental setup, an EUV light source based on tin droplets was constructed at ARCNL to perform studies under industrially relevant conditions as found in next-generation EUV lithography machines. It utilizes both commercial and home-built solid-state laser systems to perform high-resolution measurements of the fluid and plasma dynamics governing the target formation. The detailed description of the setup is provided in Chapter 2 of this thesis.

In Chapter 3, the first experimental results are presented as obtained with the setup, discussing the dynamics of tin microdroplets as a result of an ablative impact of 10-ns 1-μm laser pulses visualized by short-pulse stroboscopic shadowgraphy imaging tools. The droplet propulsion is captured in a scaling law of the plasma-imparted momentum over three decades in laser energy. The fluid-dynamic response is described by an analytical model that also shows scalability of our results with the results from the water-droplet experiments carried out at the University of Twente [31]. These findings enable optimization of the laser-droplet coupling important for reaching high CE in EUV sources.

Further, Chapter 4 provides a more detailed insight in the plasma physics underlying the plasma propulsion of the droplet, combining an extensive set of experimental results with results of radiation-hydrodynamic simulations with the RALEF-2D code [32, 33]. Good agreement was found between the experiment and simulation for the majority of the explored laser energies, revealing a scaling law

of the plasma-propulsion velocity of droplets with laser energy. Further, we perform a careful examination of the underlying physics trying to derive the obtained scaling from the existing analytical theories and conclude that none of them can be directly applied to our system.

The efficient operation of an EUV source highly depends on the stability and reproducibility of the produced laser targets. Combining an analytical modeling of the plasma pressure impact on a spherical droplet with experimental observations, Chapter 5 discusses the sensitivity of the target tilt angle, propulsion and expansion to the alignment of the laser beam with respect to the droplet. Then, our validated model is used to predict sensitivities for several practical cases directly relevant for current industrial EUV light sources.

In Chapter 6, the results from two different experimental systems, with millimeter-sized methyl ethyl ketone droplets (performed in the Physics of Fluids group at the University of Twente) and tin microdroplets (performed in the EUV Plasma Processes group ARCNL) are used in a complementary manner to understand in detail the fragmentation of laser-impacted liquid droplets.

The impact of shorter laser pulses, 15 ps in duration, that results in cavitation-driven expansion of tin microdroplets is discussed in Chapter 7. This type of target is shown to be beneficial for EUV generation in some cases but still requires further investigation of its dynamics. Combining an experimental approach with an analytical description, the observed tin mass distributions obtained from droplets of two different sizes are shown to be governed by a single dimensionless parameter, the Weber number. A summary phase diagram (target size—laser energy) is provided, capturing different behavior of the expanding tin droplets that depends on the imparted laser energy.

The results obtained in this thesis enable a more thorough understanding of physics underlying two main prepulse approaches and pave the way for even more comprehensive studies of the final-state mass and velocity distributions after fragmentation of the target material.

Chapter 2

Experimental setup

A dedicated high-vacuum setup with a droplet generator was constructed to enable high-quality experiments on tin-microdroplet-based laser-produced plasma. It comprises a vacuum system with optimal optical access, microdroplet generator, synchronization and triggering systems, drive lasers, and shadowgraph imaging systems. These parts will be presented in this chapter.

2.1 Vacuum system

A detailed schematic of the experimental setup is shown in Fig. 2.1. The drawing shows a side view of the cylindrical (DN200CF) stainless-steel vacuum vessel, with a stream of droplets located on its vertical axis. The vessel has 24 equispaced entrance ports (DN35CF) located on its circumference, 12 in the horizontal plane and another 12 at a 30° angle with respect to the horizontal plane, all precisely aligned onto the droplet's position in the center of the chamber. Such a geometry enables the alignment of a drive laser beam through a horizontal port and ensures in vacuo measurements with tools aligned at various angles with respect to the laser propagation axis. These tools are photodiodes to measure the "in-band" EUV radiation emitted in a 2% wavelength bandwidth around 13.5 nm, EUV (∼5–25 nm) and optical (∼200–800 nm) spectrometers, multiple ion probes and ion charge-energy spectrometers, as well as quartz-crystal microbalance sensors. The droplet generator is situated on the top flange of the vacuum chamber where it is mounted on an edge-welded port aligner that enables steering the droplet stream.

Further, following the droplet stream, the chamber is attached to a high vacuum line (DN100CF). At the lower part of the vacuum line, the droplet stream hits a tin catcher sitting at the bottom of a cross piece (DN100CF). The tin catcher is a cylindrical volume heated by a resistive coil installed to ensure tin capture even when coming from a highly off-axis stream of droplets. A viewport is mounted on one of the flanges of the cross piece to enable visual inspection of the tin catcher.

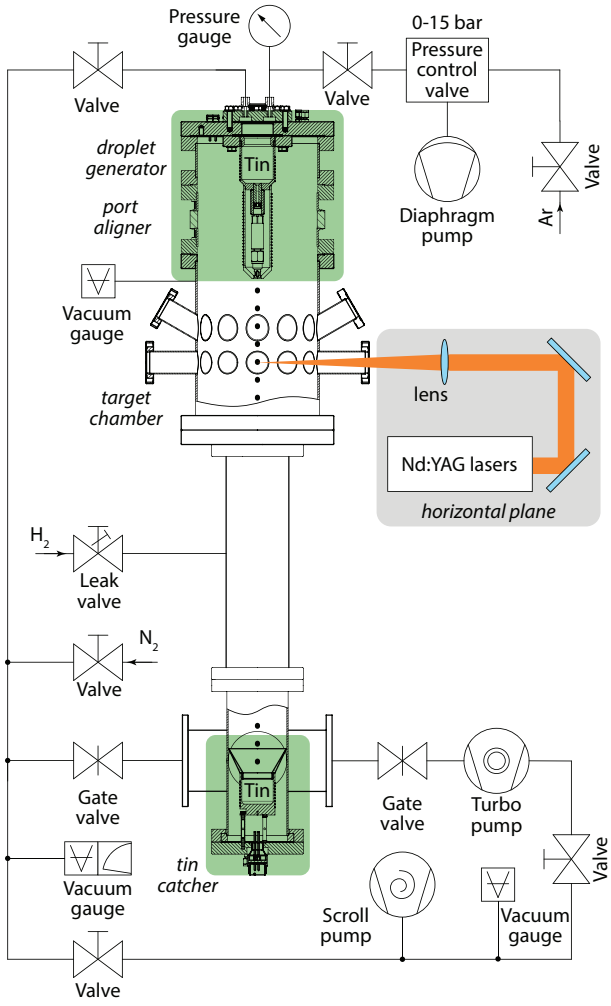

FIGURE 2.1: A sketch of the experimental setup with a vertical cut-out view of the vacuum system, tin droplet generator, and tin catcher.

Through this viewport, the droplet stream can be detected with the naked eye. Another flange of the cross piece is attached to a horizontally aligned T-piece continuing the vacuum line. The T-piece is connected with the high vacuum line through a pneumatically actuated ultra-high-vacuum gate valve, to a 300 l/m turbo-molecular pump (nEXT300T by Edwards) backed with a scroll pump (nXDS10i by Edwards). The other side of the T-piece is connected to the by-pass vacuum line, separated by a manually actuated UHV gate valve (DN35CF), and connected to the same scroll pump. The by-pass line provides an option to vent the chamber and to pump it down without the necessity of disabling the turbo pump. For venting purposes, the vacuum system has a connection to a nitrogen gas line. Pressure in the vacuum system is monitored with a wide-range pressure gauge (WRG-SL-DN40CF by Edwards) that combines a Pirani type for the upper pressure range, with an inverted magnetron type for the lower range. Typically obtained base pressures in the chamber were $\sim 10^{-7}$ mbar. Buffer gas (H_2 or Ar) fed from a gas tank can be added in a controlled manner by means of a variable leak valve (DN35CF) that is directly attached to the chamber. In this case, for a better accuracy, the pressure can be monitored by a capacitance-type vacuum gauge (DN16CF Ceravac CTR 100N 10 Torr by Leybold).

2.2 Microdroplet generator

The droplet generator is shown in the top part of Fig. 2.1. It includes a heated high-pressure molybdenum tank loaded with tin, a replaceable nozzle assembly with a filter and a piezo-actuated capillary, and a heater for the nozzle assembly. The nozzle assembly is attached to the bottom of the tin tank through a VCR fitting connection sealed with a replaceable plastic ring. The top flange of the tank has two feedthrough connections to a high-pressure argon gas and vacuum lines. Prior to the start of an experiment, the tank is loaded with solid tin in form of shots (99.995% purity) and/or cylindrical bulks (99.999% purity), at a maximum load capacity of $\sim$1 kg. Once the tank is filled with tin and pumped down to a suitable vacuum pressure ($< 10^{-3}$ mbar) and the pressure in the main vessel reached a value below 5×10^{-7} mbar, the heating process is started by means of resistive heating elements connected to power supplies (SM70-AR-24 by Delta Elektronika). Temperature values of the tank, nozzle heater, and the tin catcher are monitored by thermocouple probes (Type K by RS Pro), the readout of which is fed to programmable digital controllers (E5AC by OMRON) connected to the heating power supplies. Such a system enables controlled and stressless, slow (2°C/min) heating of the delicate elements of the droplet generator. The typical temperature of the droplet generator set during experiments is 260°C, which is well above the melting point of tin (232°C). The temperature of the tin catcher is typically higher

($> 270°C$), since the catcher's cone-shaped extension, that acts as a radiator, can be expected to have a lower temperature than that measured at the location of the thermocouple probe. Its temperature needs to be high enough to avoid producing structures of solidified tin.

After the desired temperature is reached and stabilized, the tank volume is disconnected from the vacuum line and pressurized with high-purity (99.9999%) argon gas at pressures of up to 15 bar as measured by an analog manometer (by WIKA) directly attached to the tin tank. The pressure p_{Ar} in the tank is regulated by an electro-pneumatic proportional pressure control valve (QB1SANEEZP290PSG by Proportion-Air) controlled by an external voltage supply. This valve is connected to a diaphragm pump (MP 201 T by Ilmvac) and, through a pressure reducer, to an argon gas tank. An empirically measured pressure-voltage dependence is shown in Eq. (2.1), where p_{Ar} is the argon pressure (with respect to the vacuum) in bar, and U is the voltage (in Volts) applied to the pressure control valve.

$$p_{Ar} = 1.4 + 1.96 \times U. \tag{2.1}$$

When a certain argon pressure above the bath of molten tin is reached, a liquid jet from the nozzle assembly propagates inside the vacuum chamber. Since the liquid stream is subjected to Plateau-Rayleigh instabilities [34], it breaks up into a set of small droplets. To control this process, the nozzle's capillary is driven by an annular piezo-crystal element powered by a waveform generator (33500B Series by Agilent) that applies a square-pulse modulation to the stream. With such a modulation, the stream breaks into a sequence of small droplets that have a velocity distribution leading to their coalescence, reaching the drive laser focus in the form of equidistantly spaced, mono-disperse microdroplets. Parameters of the modulating signal that can be used to adjust the droplet formation are frequency, duty cycle, and the amplitude. Typically, the droplet generator is run at several 10 kHz modulation frequency.

The tin flow through the nozzle orifice increases with the applied argon pressure. Keeping the applied modulation frequency constant, a flow increase results in larger inter-droplet distance due to higher droplet velocity (see Subsection 2.6). This distance is important, since the laser-droplet interaction might disturb the next droplet, resulting in disturbance of its shape and position at the moment of the next laser pulse [18, 35, 36].

Additionally, larger tin flows create larger droplets produced by the droplet generator. Droplet size also depends on the diameter of the nozzle orifice. The setup can be operated with a wide range of droplet diameters by adjusting three main parameters, such as size of the nozzle's orifice, or, during operation, frequency of the stream modulating signal and the argon gas pressure in the tank. Generally,

the expression for the droplet diameter D_0 (in μm) can be written as

$$D_0 = B \times f^{-\frac{1}{3}} \times p_{Ar}^{\beta}, \tag{2.2}$$

where p_{Ar}(bar) is the argon gas pressure, f (kHz) is the frequency of the signal applied to the nozzle's piezo element; empirical parameters B and β depend on the orifice size of the nozzle. The $-1/3$ power originates from straightforward mass conservation. In Section 2.6 these dependences are discussed in more detail, applied to the experimental setup.

2.3 Synchronization and trigger system

Although the coalesced microdroplets are produced at a constant repetition rate, a jitter in their velocity causes uncertainty of the droplet position at the moment of the arrival of the drive laser pulse. To solve this problem, a droplet detection system that actively triggers the timing of the drive laser pulse is required, maintaining reproducible interaction with each droplet. Such a system is implemented in the experimental setup and described in the following.

At a distance of ∼200 mm from the nozzle's orifice, and ∼3 mm above the laser-droplet interaction zone, droplets pass through a sheet of 633-nm wavelength laser light obtained by focusing an expanded beam of a 22.5 mW helium-neon laser (HNL225R-EC by Thorlabs) by means of a cylindrical plano-convex lens with 200 mm focal length. The laser sheet normal is aligned along the droplet stream and has transverse dimensions (FWHM) of 2000 μm×30 μm. Passing through the laser sheet, each droplet scatters light. This light is detected by a photo-multiplier tube (PMT, Hamamatsu H10492) installed at a 60° angle with respect to the He-Ne laser beam and has a 633-nm laser line filter (Thorlabs) in front of it in order to suppress stray light from the plasma. The electronic signal from the PMT is filtered by a low-pass electric filter and is displayed on a 200-MHz bandwidth oscilloscope (Keysight DSOX3024A), the trigger output signal of which is used for triggering the other equipment involved in the experiment. Reduction of a multi-kHz PMT signal down to a 10-Hz signal suitable for triggering the (10 Hz) laser systems and other equipment is achieved by introducing a hold-off time delay (∼ 99 ms) on the trigger output of the oscilloscope. In addition, in this configuration, a certain point on the time trace of the PMT signal can be chosen as a trigger time thus giving one more option to adjust the timing of the trigger pulse with respect to the droplet position. The trigger pulse from the oscilloscope is fed to a programmable transitor-to-transitor logic (TTL) pulse generator that provides a 10-Hz repetition rate output either from the oscilloscope or, in case the input signal is not detected in time, from its own internal clock. This additional internal trigger ascertains

that lasers are fired at regular intervals to keep a constant thermal load even if, for example, a droplet is missed. Further, this 10-Hz signal triggers the delay system consisting of two multi-channel digital delay generators (DG645 by Stanford Research Systems) connected in series. These delay generators are required for triggering the equipment used in the experiment. Accurate alignment of the laser sheet, followed by an appropriated timing of the output delay channel of the first delay generator that triggers the Nd:YAG drive laser, is crucial to establish the laser-droplet interaction occurring in the center of the vacuum chamber. Since the droplets are ejected downward along the vertical axis of the chamber, changing the timing of the drive laser pulse can be used for systematic studies related to the off-center laser-droplet interaction (see Chapter 5). The second delay generator is connected through a trigger divider device that can be set to skip N trigger pulses. This further reduction of the repetition rate is necessary for the correct operation of the data acquisition system that is not able to process a 10-Hz data influx from all measuring equipment at the same time.

2.4 Drive laser systems

Experiments presented in this thesis involved two Nd:YAG drive laser systems, one with a fixed pulse duration of 10 ns, and another one providing pulses of 15 ps duration. These two laser systems give rise to very different laser-droplet interactions. In the case of ns-long pulses, disk-like targets are obtained (Chapters 3, 4, 5, 6). For the ps-long pulses, volumetrically distributed targets are produced through laser-induced cavitation (Chapter 7). In the following, the main performance characteristics of these lasers are discussed.

Nanosecond drive laser system

In our experiments producing disk-like targets we used 1064 nm wavelength pulses from a seeded Nd:YAG laser operating at a 10-Hz repetition rate (Quanta-Ray 250 Pro by Spectra-Physics). The laser consists of an oscillator (two flashlamp-pumped Nd:YAG rods) providing a maximum energy per pulse of ∼400 mJ, and the amplification stage (another two flashlamp-pumped Nd:YAG rods) increasing the output up to ∼1.3 J. This laser's output has a flat-top spatial profile and a Gaussian-like temporal profile with a full-width at half-maximum of 10 ns. The injection seeding ensures single longitudinal mode operation of the laser, associated with a smooth temporal profile. The pulse duration is measured with a 150-ps rise(fall) time detector (DET025AL by Thorlabs) connected to a 1-GHz bandwidth oscilloscope (MSO9104A by Keysight). Before reaching the droplet, light emitted by the laser propagates through a number of optical components. First, the laser beam has

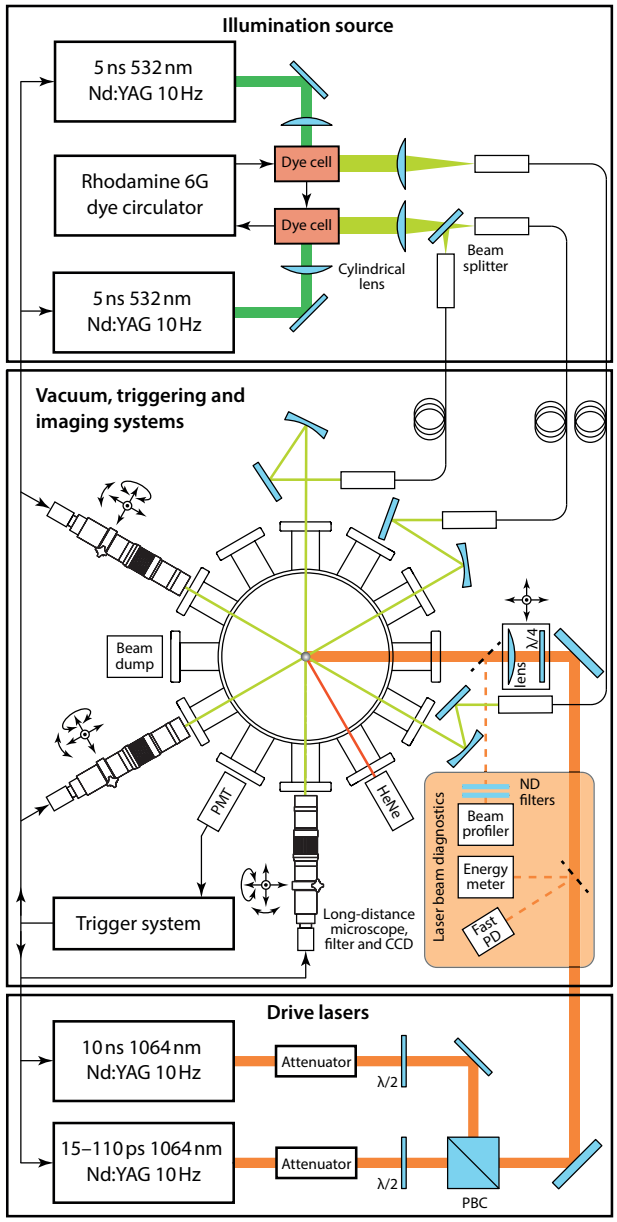

FIGURE 2.2: Schematic representation of the experimental setup comprising a vacuum system with optimal optical access, microdroplet generator, synchronization and triggering systems, drive lasers, and shadowgraph imaging systems.

an unpolarized component in its spatial structure. We employ a combination of a 2" thin-film polarizer (TFP), a half-wave ($\lambda/2$) plate, and again a TFP to remove this unwanted component. In order to adjust the laser beam energy, another combination of a $\lambda/2$ plate and a TFP is used. Changing the laser energy in this manner, the spatial profile of the laser beam stays unaltered within the full range of energies. The maximum attenuation of the laser beam by means of this system is determined by the polarization extinction ratio provided by the TFP. Therefore, to make very low-energy experiments feasible, two more TFPs are installed, transmitting the laser beam with linear polarization parallel to the horizontal plane. For the experiments requiring a different polarization setting, an optional $\lambda/2$ waveplate can be installed to adjust the angle of the linear polarization, or, to obtain a circular polarization of the laser light, a $\lambda/4$ waveplate can be installed with an appropriate alignment of its optical axis.

To reach high intensity of the laser light, the beam is focused down by means of a plano-convex lens with anti-reflective (AR) coatings at 1064 nm on both sides. The spatial intensity distribution is measured with a beam profiler CCD camera (Beamage-4M by Gentec). The obtained distribution has a Gaussian profile shape with ellipticity of $> 95\%$ (the ratio between the minor axis and the major axis). The beam enters the vacuum chamber through its AR-coated window and hits a droplet. Such a laser impact results in ablation and ionization of the droplet material. The thus obtained plasma quickly expands in the vacuum, transferring its momentum also to the rest of the liquid target. The generated plasma pressure propels and deforms the droplet (see Chapters 3, 4, 5, 6). In case of a perfectly circular Gaussian-like beam profile, the droplet expands into a circular disk [20, 21].

Picosecond drive laser system

The experiments with cavitation-driven expansion of tin microdroplets (see Chapter 7) were performed with a Nd:YAG laser system capable of producing laser pulses of 1064 nm wavelength with a duration ranging 15–100 ps and maximum energy per pulse of 200 mJ at a 10-Hz repetition rate. The laser system is described in more detail in Ref. [37]. For the experiments discussed in Chapter 7, the pulse duration was set to 15 ps and the laser beam was attenuated by means of a combination of a $\lambda/2$ waveplate and a TFP. The focused laser beam has a Gaussian spatial profile with an ellipticity of $\sim 90\%$. As in the beam path of the nanosecond drive laser system, the beam polarization can be set to be linear, with a certain angle of polarization, or circular.

In the experiments with both ns and ps laser pulses, laser energies are measured with a calibrated energy meter (QE25LP-H-MB-QED-D0 by Gentec). To check the linearity of the sensor's response within the whole range of the energies relevant for

our experiments, several tests with a set of neutral density filters were performed. The tests proved excellent linearity well within the instrumental uncertainty (±3%) stated by the manufacturer. Possible offset errors in the low energy range are below 20 μJ.

2.5 Shadowgraph imaging of tin microdroplets

Visualisation of the dynamics of micrometer-sized droplets requires a high-speed imaging system. Due to the reproducible nature of the experiments, such dynamics can be captured in a stroboscopic manner with a low-repetition rate short-pulse illumination. The experimental setup discussed in this chapter is equipped with stroboscopic shadowgraphy systems enabling three-side imaging of tin microdroplets after laser impact.

2.5.1 Illumination scheme

Generally, a shadowgraphy setup consist of an illumination source, imaging objective, filter, and a light sensitive device (CCD). In the following, two types of illumination sources used for this dissertation are described.

Near-infrared coherent light source

The shadowgraphy system used in the earlier stages of the experiment (the results of which are reported in Chapters 3, 4, 5, 6) utilized an 850-nm wavelength pulsed diode laser (IL30C15 by Power Technology Inc.) to produce backlight illumination. The pulse duration is adjustable within the range of 15–30 ns. Due to the diode's structure, the illumination background of the images has a vivid modulation that fluctuates from pulse to pulse and therefore cannot be reduced with a simple background subtraction function (see Fig. 2.3(a)).

Dye-based illumination source with limited coherence

The increase in the resolution and the overall quality of the shadowgraphy images, comparing Chapters 3, 5 with 4, 6, and 7, was made possible by switching to another illumination source of a better quality. A dye laser (Quanta-Ray PDL-2 by Spectra-Physics) was chosen for this purpose. It consists of three dye cells (oscillator, pre-amplifier, and amplifier) connected in series and flushed with Rhodamine 6G dye dissolved in ethanol at a 2 l/min pumping rate by a dye circulator (RD 1000 by Radiant Dyes Laser Acc.). Being pumped by a 5-ns 532-nm laser pulses from a Nd:YAG laser (Continuum Surelite III), the dye emits light with spectral peak around 560 nm wavelength with the same pulse length. The prism disperser and

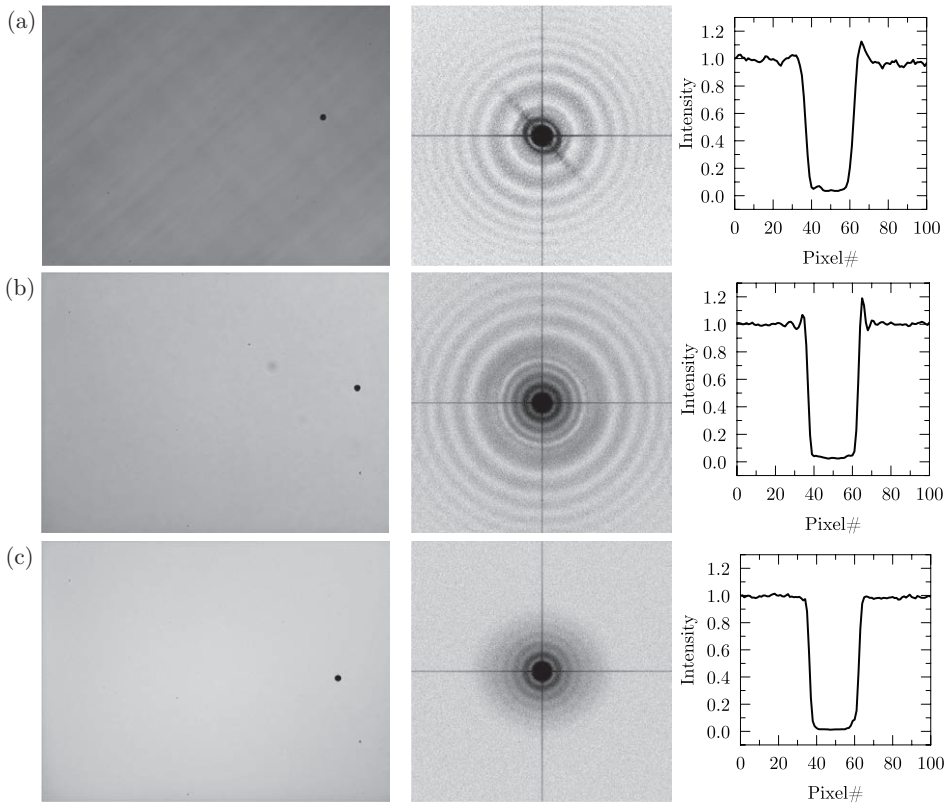

FIGURE 2.3: (Left) Examples of shadowgraphy images of tin microdroplets obtained with different illumination systems with (middle) corresponding fast Fourier transform spectra (individually normalized for visibility), and (right) horizontal intensity profiles along the droplet's equator. (a) 850-nm light illumination. (b) Illumination with single-cell 560 nm light transferred via a 600-μm-core fiber. The asymmetry in the intensity profile across the droplet is caused by a small misalignment of the illumination light source with respect to the imaging system. (c) Same light source as (b) but the light is transferred via a 3-mm PMMA fiber.

the wavelength selection grating of the laser were blocked to produce the light with limited temporal coherence to produce a speckle-free illumination background. In this manner, the pulses coming from the oscillator into the pre-amplifier consist of amplified spontaneous emission (ASE) and are further amplified in the amplification cell. To reduce spatial coherence, the output light was focused into a

600-μm-diameter-core multimode fiber. With such an illumination source, the images gained in quality, although still having a clear diffraction pattern around the imaged object (see Fig. 2.3(a)). In order to further decrease the temporal coherence of the light, all but the pre-amplification dye cell were removed. Produced in this manner, the illumination light consists of ASE and dye fluorescence. The images with this illumination source were used in some experiments presented in Chapters 4 and 7. Further improvement of the shadowgraphy system was achieved by reducing the spatial coherence. The output light was coupled into a 3-mm diameter PMMA fiber with the fiber-coupling optics being installed directly after the cell. The shadowgraphy images obtained with this illumination source clearly show an improvement in reducing the diffraction pattern (see Fig. 2.3(c)).

The most recent experiments that are not discussed elsewhere in this thesis required two light sources triggered separately with a controlled delay between the two pulses. For this purpose, a second dye cell was used in the aforementioned way, being pumped with a separate Nd:YAG laser (Continuum Surelite III). The output of the first cell is split into two fiber couplers for shadowgraphy at 90° and 150° with respect to the drive laser beam propagation direction and the light from the second cell is used for the one at 210°. This configuration of the illumination source is shown in Fig. 2.2(top).

Transferred to the experimental setup via optical fiber, the light is collimated and aligned through a vacuum viewport onto the droplet by a combination of a plano-convex lens (30 mm focal length) and a 2"-diameter concave mirror (200-mm focal length). The described conditions result in a high resolution ($\sim$4 μm) of the imaging system together with a speckle-free image background.

At the opposite side of the chamber the light, partially obscured by the droplet, passes through a long-distance microscope (Model K2 DistaMax with CF-1/B objective and NTX tube (2x) by Infinity), a single-band bandpass filter at 560 nm wavelength with a 20 nm FWHM bandwidth from Semrock and falls onto a CCD camera (MANTA G-145B NIR by Allied Vision) with the sensor size of 1388×1088 pixels. Each objective with an attached camera is placed on a five-axis (x, y, z, yaw, pitch) mount enabling precise alignment on the droplets.

Spatial calibration of the shadowgraphy imaging system is performed by imaging a transparent resolution target (R1L1S1P by Thorlabs) at the location of the droplet stream. The target, with dimensions of 18 mm×18 mm×1.5 mm, contains several elements for resolution and distortion tests, including three square grids, 20×20 arrays with 100, 50, and 10 μm pitch. In order to avoid an uncertainty caused by a possible non-orthogonal placement of the calibration target with respect to the imaging axis, the vertical dimension of the grids was used to measure the magnification of the imaging system. The magnification is determined by the working distance of the microscope objective and its configuration, and for most of

the experiment discussed here was close to 1.85 μm/pixel.

2.5.2 Image analysis

The research presented here requires time-resolved measurements of the droplet dynamics that includes tracking the position, size, and tilt angle of the produced targets, as seen on the images obtained with the shadowgraphy system. Typically, each measurement contains a sequence of about 1000 images from each camera. To process such a large amount of data, an automized script based on the MATLAB Image Processing toolbox was prepared. The main steps of the image analysis can be described as: normalization based on an image with the corresponding illumination background, binarization with a fixed threshold value, detecting relevant objects on the binarized images and applying functions to measure their dimensions and other properties.

To determine the correct value of the threshold intensity of the droplet profile to measure its diameter in the experiments, a cylindrical platinum wire with diameter similar to the droplet size is placed at the droplet position and imaged with the same shadowgraphy system. Prior to the calibration procedure, the diameter of the wire was measured with a scanning electron microscope (SEM) to be 49.78(9) μm, with the uncertainty given by the variation of the wire size along its length. By correlating this value to the outline of the wire profile on the shadowgraph images with known pixel dimensions (see previous subsection), a corresponding intensity threshold value of $\sim$28% was obtained. However, the shape of the wire profile on the shadowgraphy images appears to be different from the droplet's profile. Therefore, this calibration can provide only a first estimate of the intensity threshold value. Moreover, this value could be sensitive to illumination setting of a particular experiment. We estimate systematic uncertainties on the measurement of the droplet size from these, and other sources of error to be below a combined 10% relative value. The here described method was applied to the measurements described in Chapters 3–6.

To characterize the shadowgraphy system with the low-coherence illumination (see Fig. 2.3(c)), more detailed measurements of the correct value of the threshold corresponding to the real droplet size were performed by imaging droplet streams ejected by the droplet generator (DG) with a $\sim$4.5 μm nozzle size at varied parameters. Measurement results of the droplet diameter D_0 obtained within a wide range of modulation frequencies f are shown in Fig. 2.4. Taking into account mass conservation, each data set is fitted with a simple power-law function $A \times f^{-\frac{1}{3}}$. By comparing goodness of each fit, one can obtain the value of the threshold that is valid within the explored range of droplet sizes. We find that a threshold value of 40% minimizes χ^2.

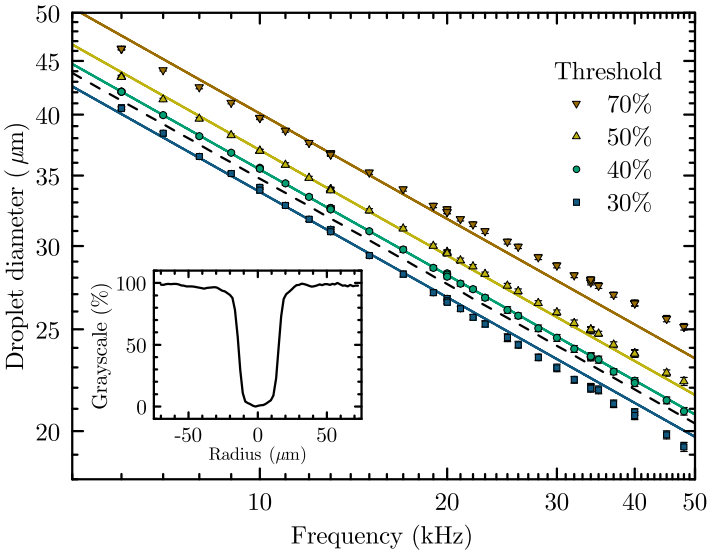

FIGURE 2.4: Results of the image analysis of shadowgraphy images of tin microdroplets ejected by a ∼4.5 μm nozzle at 12 bar argon gas pressure. Droplet diameters are measured as a function of nozzle frequency obtained at different values of the threshold value. Solid lines represent a power-law fits $A \times f^{-\frac{1}{3}}$. Inset is a typical line-out graph along the droplet equator. The black dashed line depicts the results of the measurement of tin consumption (see main text).

Another method was applied to determine the droplet size by measuring the tin consumption from the start of streaming until its end. The DG with a similar nozzle size (a value of 4.48 μm accurately quoted by the manufacturer) was loaded with 883.4 g of tin, while the argon pressure was maintained at 12 bar. After 158 h and 40 min the droplet streaming ended leaving ∼4 g of residual tin in the tank. This corresponds to a mass flow rate of 1.54×10^{-3} g/s, giving a value for $A = 74.9\,\mu\text{m}\,\text{kHz}^{\frac{1}{3}}$. Using this value, the droplet diameter D_0 (μm) for a specific frequency f (kHz) can be obtained. The corresponding power-law function is displayed in Fig. 2.4 as a black dashed line. The agreement with the values obtained with the varied threshold method (see above) is excellent. A small systematic deviation of about 2% is visible, which can be attributed to systematic uncertainties, e.g., in establishing the imaging magnification.

2.6 Characterization of the droplet stream

Characterization of the droplet stream is one of the crucial tasks on the way to reaching desirable and stable conditions for the experiments on laser-droplet interaction. After calibrating the shadowgraphy imaging, an imaged droplet stream can be characterized in terms of droplet size, droplet and jet velocities, and inter-droplet distance. Figure 2.5(a) shows the results of the size measurement of the droplets of different streams. Here, the pressure of the DG was set at five different values and the nozzle frequency was scanned within each pressure setting. Solid lines represent power-law fits with the exponent fixed at $-1/3$. The only free fit parameter, A, corresponds to the measured droplet velocity as a function of the argon gas pressure in the DG and the obtained values for it are shown in Fig. 2.5(b). The fit (red line) is represented by the empirical equation

$$\upsilon_d = K_\upsilon \times p_{Ar}^{\beta}, \tag{2.3}$$

where υ_d is the droplet velocity, p_{Ar} is the argon gas pressure, and K_υ and β are the free fit parameters.

The mass flow rate through the nozzle orifice can be written as

$$\dot{m} = \frac{4\pi}{3}\rho(D_0/2)^3 f = \frac{A^3}{6}\pi\rho, \tag{2.4}$$

where A is the fit parameter from Fig. 2.5(a). On the other hand,

$$\dot{m} = \upsilon_j R_j^2 \pi\rho, \tag{2.5}$$

where υ_j and R_j are the velocity and radius of the liquid tin jet, respectively, and ρ is the density of liquid tin. Therefore, the expression for the jet velocity can be written as

$$\upsilon_j = \frac{A^3}{6R_j^2}. \tag{2.6}$$

Values for the jet velocity as function the droplet velocity can be obtained assuming $R_j \approx 0.9 \times 4.5/2 \approx 2\,\mu$m and taking the corresponding values of A (see Fig. 2.5(c)). The numerical factor of 0.9 is a typical value for the discharge coefficient [38] for the here relevant Reynolds numbers ($\sim$100). Several studies of liquid jets [39–41] agree on the same relation between jet and droplet velocities, that can be written as

$$\upsilon_j = \frac{\upsilon_d + \sqrt{\upsilon_d^2 + \upsilon_c^2}}{2}, \tag{2.7}$$

where the capillary velocity $\upsilon_c = \sqrt{\frac{4\sigma}{\rho R_j}}$. For a jet radius $R_j \approx 2\,\mu$m and the tin surface tension $\sigma = 0.532\,$N/m, the above equation is plotted in Fig. 2.5(c) as a

dashed red line. We find good agreement with the experimentally determined data within its ±5% uncertainty.

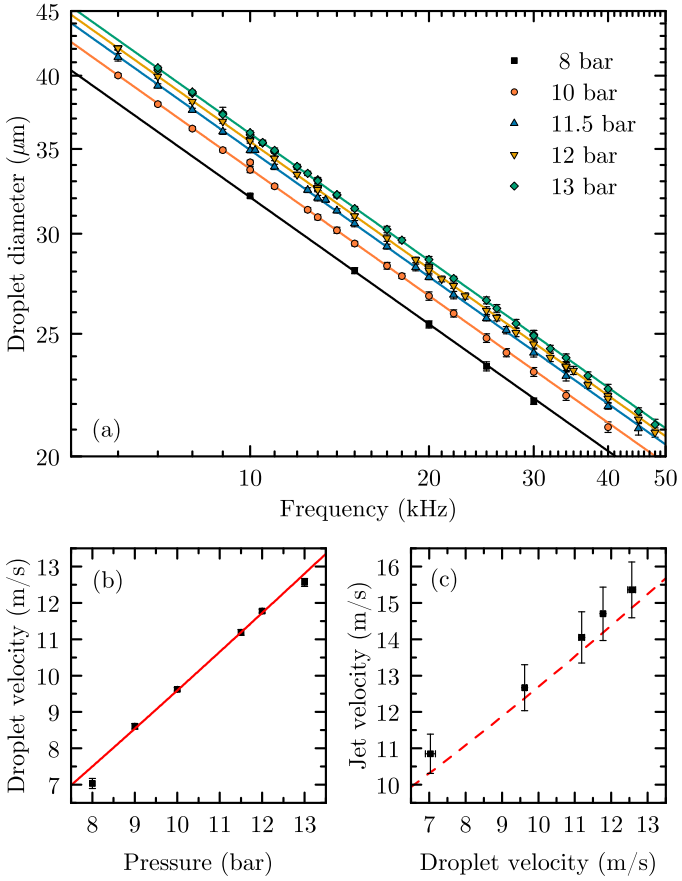

FIGURE 2.5: (a) Droplet diameter obtained from shadowgrams (threshold value of 40%) as a function of the nozzle modulation frequency for different values of argon gas pressure in the tin tank. (b) Measured droplet velocity as a function of argon pressure. Only the droplet velocity was obtained in the measurements at 9 bar. The solid red line shows a power-law fit Eq. (2.3). (c) Jet velocity derived from the fits shown in (a) as a function of the droplet velocity. Vertical error bars represent systematic uncertainty from the threshold determination in the image analysis. The red dashed line is obtained from Eq. (2.7).

2.7 Outlook

To enable even better optical access, a new experimental setup called DALEK was designed and constructed. It will be used in future experiments. Experiments benefit from having more access ports aligned onto the laser-droplet interaction zone. The new design includes 12 extra ports (DN35CF) below the horizontal plane, aligned with axes of the top ports. This new geometry enables possibility of using more diagnostics that require the line-of-sight alignment through the plasma. This new system will also soon be upgraded to having a larger volume of the available tin in the tank. To comply with this upgrade, the new tin catcher has a larger volume as well.

To increase the resolution of the shadowgraphy system, microscope objectives with shorter working distance, and thus higher numerical aperture, could be used. As the size of the vacuum chamber puts constraints on this parameter, the new design of the chamber accommodates for using re-entrant viewports. Such a viewport (DN63CF) has a cylindrical tube extending inside vacuum, with a sealed, replaceable window at the end. The diameter of the tube allows for placing the microscope closer to the object plane. At a working distance of $\sim 120\,\mathrm{mm}$, the obtainable resolution should be $< 2\,\mu\mathrm{m}$.

These improvements in the experimental setup will enable more detailed studies of the laser-produced plasma with a more comprehensive characterization of the pre-pulse induced tin droplet deformation.

Chapter 3

Plasma propulsion of a metallic microdroplet and its deformation upon laser impact

D. Kurilovich, A. L. Klein, F. Torretti, A. Lassise, R. Hoekstra, W. Ubachs, H. Gelderblom, and O. O. Versolato, Phys. Rev. Appl. **6**, 014018 (2016).[1]

The propulsion of a liquid indium-tin micro-droplet by nanosecond-pulse laser impact is experimentally investigated. We capture the physics of the droplet propulsion in a scaling law that accurately describes the plasma-imparted momentum transfer over nearly three decades of pulse energy, enabling the optimization of the laser-droplet coupling. The subsequent deformation of the droplet is described by an analytical model that accounts for the droplet's propulsion velocity and the liquid properties. Comparing our findings to those from vaporization-accelerated mm-sized water droplets, we demonstrate that the fluid dynamic response of laser-impacted droplets is scalable and decoupled from the propulsion mechanism. By contrast, the physics behind the propulsion of liquid metal droplets differs from that of water. It is studied here in detail, and under industrially relevant conditions as found in the next-generation nanolithography machines.

[1] Dmitry Kurilovich and Alexander L. Klein contributed to this chapter as part of their PhD theses, tin data is acquired by Dmitry Kurilovich and water data by Alexander L. Klein

3.1 Introduction

Micro-droplets of tin can be used to create extreme ultra-violet light (EUV), *e.g.* in next-generation nano-lithography machines [13, 42], where the droplets serve as mass-limited targets [23, 43] for a laser produced plasma (LPP). In such machines these droplets, several 10 μm in diameter, are targeted by a focused nanosecond-pulse laser at intensities that lead to optical breakdown and the creation of a high-density and high-temperature plasma [13, 23, 44]. Line emission from electron-impact-excited highly charged tin ions in the plasma provides the EUV light [13, 23]. For certain applications, it is beneficial to apply a dual-pulse sequence in which a laser "prepulse" is used to carefully shape the droplet into a thin sheet that is considered advantageous for EUV production with the subsequent, much more energetic, "main pulse" [13, 43, 45]. Maximizing the conversion efficiency of such EUV sources, while minimizing the amount of fast ionic and neutral debris that limit EUV optics lifetime (see [13, 45, 46] and references therein) requires a careful control over the droplet propulsion and its shape. This in turn requires a profound understanding of the coupling of the laser to the droplet as well as the droplet's fluid dynamic response to such a laser pulse impact. While the propulsion and deformation of water droplets due to laser-pulse impact has been studied in detail [31], the interaction between liquid metal droplets and a pulsed laser, although of direct relevance to EUV lithography, has remained unexplored. This interaction is governed by plasma dynamics with its distinct scaling laws [47–49], providing a fundamentally different way of momentum exchange to the droplet.

Here, we present an analysis of the response of liquid indium-tin droplets to laser-pulse impact in a setting very close to the one used in the generation of EUV light for the industrial application. We show that the droplet response to laser impact is governed by two physical processes that occur at completely different, and therewith separable, timescales. First, the interaction of the nanosecond laser pulse with the metal generates a plasma [48, 50] and induces propulsion of the droplet. Second, fluid dynamic effects govern the shape-evolution of the droplet, which takes place on a microsecond time scale. We reveal in detail the mechanism behind metal-droplet propulsion by laser impact and present a scaling law for the propulsion speed as a function of laser energy that captures the onset of plasma formation. This scaling law enables us to optimize the laser-droplet coupling for EUV generation purposes. Next, we discuss the remarkable analogies between metal- and water-droplet [31] propulsion by laser impact. We demonstrate that even though the metal-droplet propulsion mechanism is completely different from that of water droplets, the fluid-dynamics response is identical and well described by a universal analytical model.

3.2 Experimental methods

Figure 3.1 shows a detailed description of the experimental set-up. We use a eutectic indium-tin alloy (50In-50Sn of 99.9% purity with liquid density $\rho = 6920\,\mathrm{kg/m^3}$ at 250° C [51]), a substance almost equivalent to pure tin in terms of atomic mass, density, and surface tension, but with a conveniently low melting point. Droplets are dispensed from a droplet generator at ∼10-kHz repetition rate, with final radii $R_0 \approx 25\,\mu\mathrm{m}$ and are falling down at a speed of ∼12 m/s in a vacuum vessel. No significant acceleration under gravity occurs on the time scale relevant for the experiment. The droplets relax to a spherical shape before they pass through a horizontal light sheet produced by a helium-neon laser. The light scattered by the droplets is used to trigger an injection-seeded Nd:YAG laser operating at 10-Hz repetition rate that emits a pulse at its fundamental wavelength of $\lambda = 1064\,\mathrm{nm}$ with a duration of $\tau_p \approx 10\,\mathrm{ns}$ full width at half maximum (FWHM), focused down to a circular Gaussian spot. We studied the propulsion for two different focusing conditions: ∼115 μm and ∼50 μm FWHM at the position of the droplet. In the first and main case of ∼115 μm FHWM, the width is larger than the droplet diameter in order to decrease the sensitivity to laser-to-droplet alignment and to provide a pressure profile required for obtaining a flat thin sheet [21]. The finite geometrical overlap thus obtained precludes the full laser pulse energy from reaching the target. The energy of the laser pulse is varied in a manner that does not affect the transversal mode profile of the laser beam.

Imaging of the droplet is obtained by employing two pulsed laser diodes (PLDs). One of these is aligned orthogonally to the Nd:YAG laser light propagation direction to provide side-view images. The other PLD is angled at 30° to it (see Fig. 3.1) for a (tilted) front view. In both cases, the PLD light passes through a band pass filter before it falls onto the CCD chip of a camera through a long-distance microscope. The shadowgraphic images thus obtained are used to track size, shape, and velocity of the droplet expansion in the direction along the Nd:YAG laser impact and perpendicular to the falling droplet. A stroboscopic time series of different droplets at various time delays (see Fig. 3.2) with an arbitrary number of frames is constructed by triggering once per Nd:YAG shot, each time with an increasing delay.

3.3 Results

The response of the In-Sn droplet to laser impact is shown in Fig. 3.2. The laser pulse generates a plasma that expands away from the droplet surface. As a result, the droplet is accelerated to a speed $U \sim 0.5 - 350\,\mathrm{m/s}$ on a time τ_a given by the lifetime of the generated plasma, which is known to be smaller than a few τ_p [52].

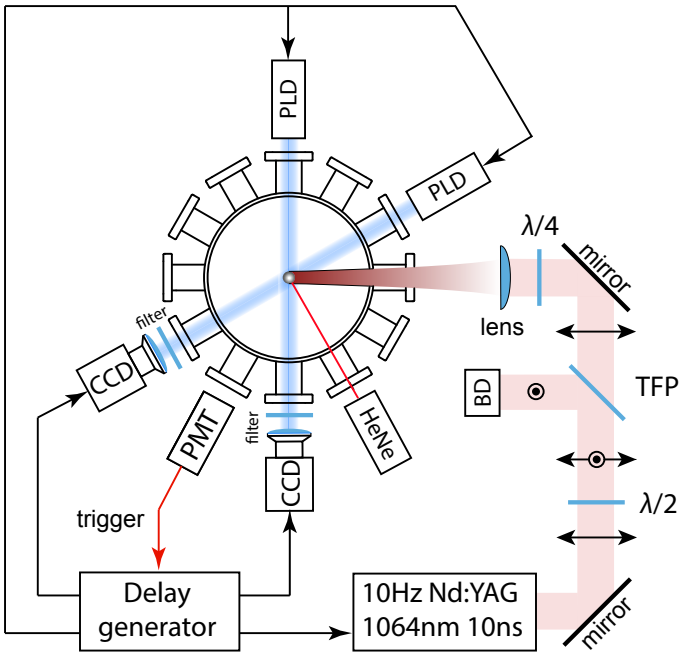

FIGURE 3.1: Sketch of the experimental setup in top view. Depicted is a vacuum vessel, typically at 10^{-7} mbar, with its many optical access ports. Droplets are dispensed from a nozzle (not shown) held at a temperature of 250° C. A horizontal light sheet produced by a helium-neon (HeNe) laser enables the triggering of the experiment: the light scattered by the falling droplet is detected by a photomultiplier tube (PMT) that sends a signal to a delay generator. This delay generator, in turn, triggers an injection-seeded Nd:YAG laser that emits a pulse at $\lambda = 1064\,\mathrm{nm}$ with a duration of $\tau_p \approx 10\,\mathrm{ns}$ (FWHM). A 1000-mm (500-mm) focal-length N-BK7 lens produces a circular Gaussian focus of size $\sim$115 μm (50 μm) FWHM at the position of the droplet. The circle and arrow symbols along the optical axis indicate the direction of polarization of the laser beam. The energy of the laser pulse is controllable through the use of a half-wave plate ($\lambda/2$), a thin film polarizer (TFP), and a beam dump (BD). Before the focusing lens, a quarter-wave plate ($\lambda/4$) produces a circular polarization. The delay generator also triggers the pulsed laser diodes (PLD, at 850-nm wavelength; $\sim$15 ns pulse length) one of which is aligned orthogonally to the Nd:YAG laser light propagation direction. The other PLD is angled at 30° to it. In both cases, the PLD light passes through a band pass filter before it falls onto the CCD chip of a camera through a long-distance microscope and produces a shadowgraph. The magnifications are 2.0(2) μm/pixel and 2.8(3) μm/pixel for the orthogonal and 30° shadowgraphs, respectively.

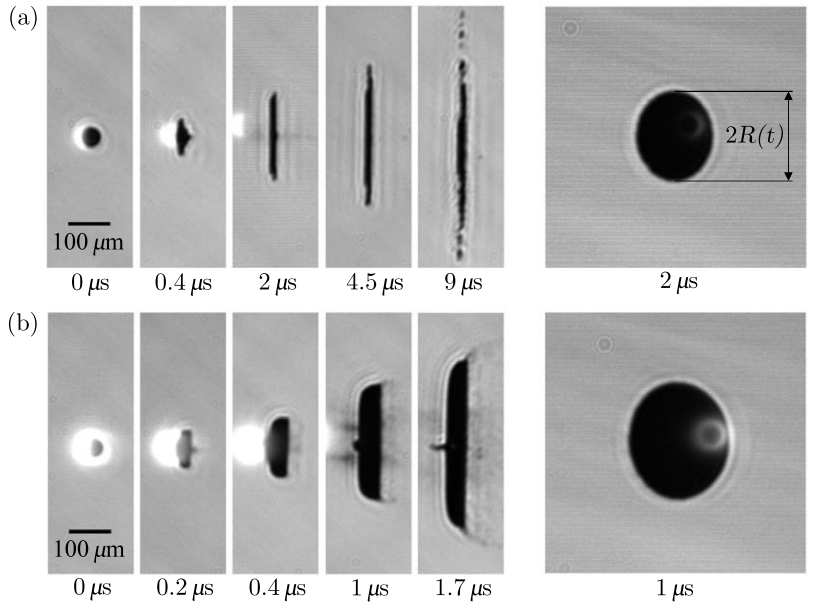

FIGURE 3.2: Shadowgraphy images of In-Sn droplets in side and (tilted) front view (see Fig. 3.1). (a) Expansion of an In-Sn droplet as viewed from the side. Droplets are irradiated with a ∼115 μm FWHM focused 10-ns Nd:YAG laser pulse impinging from the left with a total pulse energy of 7 mJ. The stroboscopic droplet expansion sequence is constructed from shadowgraphs of different droplets at different time delays. A 30 degree view is provided on the right. (b) The same as (a) but for a 70 mJ energy pulse, which gives rise to a faster expansion (note the different time scales). The white glow visible to the left of the expanding droplet is plasma light. Images have been vertically aligned to center on the expanding droplet.

The subsequent deformation of the droplet occurs on the much longer inertial timescale $\tau_i = R_0/U \approx 1\,\mu$s (here, U is taken from the case shown in Fig. 3.2(a)). The deformation is eventually slowed down by surface tension on the capillary timescale $\tau_c = \sqrt{\rho R_0^3/\gamma} \approx 14\,\mu$s. The time scales relevant to this problem can thus be ordered [31]

$$\tau_p < \tau_a \ll \tau_i < \tau_c, \tag{3.1}$$

which illustrates the clear separation of timescales between plasma generation as a cause for the propulsion on the one side and the fluid-dynamic response on the other side. Below, we discuss first the droplet propulsion mechanism and second the droplet deformation.

3.3.1 Droplet propulsion

Using the shadowgraph images of the type shown in Fig. 3.2 we study the propulsion of the droplet as a function of the laser pulse energy, which is varied between 0.4 and 160 mJ. Figure 3.3 shows that, over the nearly three decades of laser pulse energy studied in this work, the velocity of the droplet ranges from below 1 m/s to above 300 m/s and appears to follow a power-law type scaling with the laser pulse energy impinging on the droplet, E_{OD}. It is a fraction of the total pulse energy E given by the geometrical overlap of laser focus and droplet. The similarity of the data obtained for the two different focusing conditions shows that E_{OD} is indeed the relevant parameter describing the scaling of U in the present study. Significant deviations from this simple parametrization are expected for foci much smaller than the droplet [21]. To explain the observed scaling, we first discuss the mechanism through which the laser interacts with the metal.

The interaction of a high-intensity laser pulse with the droplet is governed by plasma dynamics[2]. As soon as a plasma is generated, inverse bremsstrahlung absorption [47] strongly decreases the initially high reflectivity of the metallic surface down to negligible values. This facilitates the further ablation of the target material. Analogous to the work on water droplets [31], we relate the propulsion speed U of the micro-droplet (mass M) to the amount of ablated mass m through momentum conservation

$$MU = mv, \tag{3.2}$$

where v is the velocity of the ejected mass along the axis of propulsion. The spatial distribution of this ejected mass peaks in the direction back towards the laser [53]. In the present intensity regime, simulations predict v to range from 5–15×10^3 m/s [54] and to be a function of the laser intensity. Experimentally, $v \approx 8.5 \times 10^3$ m/s at a laser intensity of 2×10^{11} W/cm^2 [46] which we take as a first estimate of the value for v in the following. The ablated mass m can be obtained employing a semi-empirical mass ablation law [55, 56]:

$$m = A \times \pi R_0^2 \times \left[\left(\frac{I}{I_0} \right)^{5/9} \left(\frac{\lambda_0}{\lambda} \right)^{4/9} Z^{3/8} \right] \times \tau_p, \tag{3.3}$$

with laser-pulse intensity I and I_0=10^{11} W cm^{-2}, wavelength λ and λ_0=1 μm, and atomic number Z=49–50 (for indium-tin). The term in square brackets is based on an analytical treatment of the one-dimensional expansion of a plasma from a plane

[2] The typical impulse p_l exerted on the droplet in the limit of fully absorbed light scales as $p_l \propto E/c$, with E the energy of the absorbed light and c the speed of light. Even at the highest pulse energies assuming a maximum fraction of absorbable light of ∼0.5, given by the geometrical overlap of laser and droplet in the case of the 50 μm FWHM focus, this impulse would yield a typical droplet speed $U \approx 0.5$ m/s which is negligible with respect to the observed speeds.

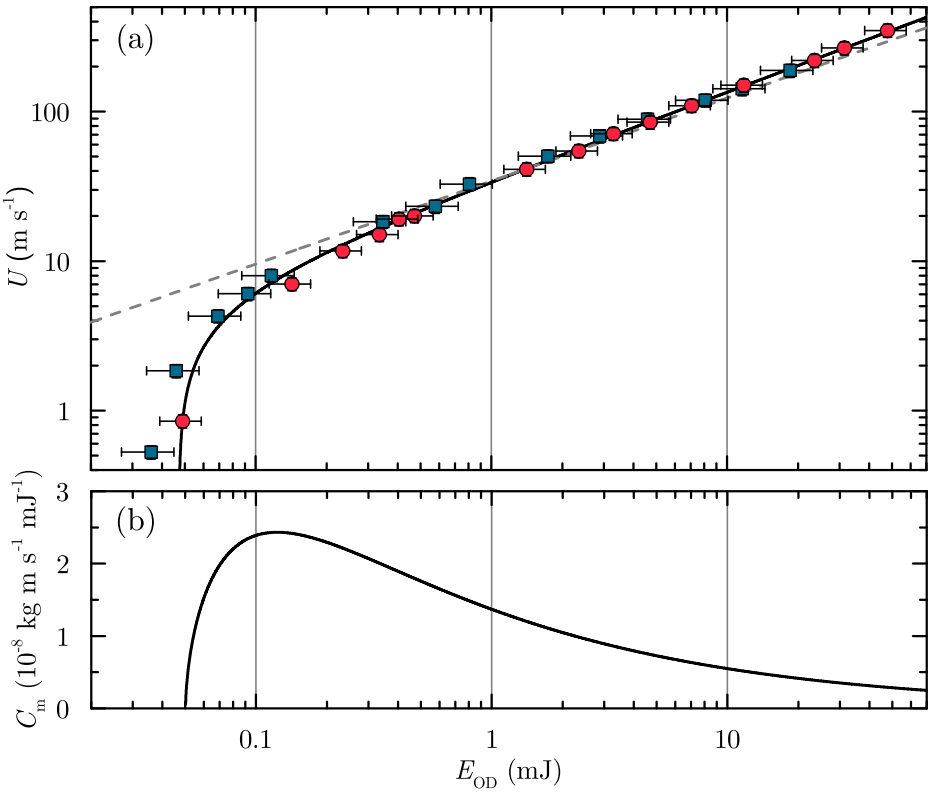

FIGURE 3.3: (a) Propulsion velocity U of In-Sn droplets as a function of total laser-pulse energy impinging on the droplet E_{OD} for two different focusing conditions. Blue squares represent the data obtained at a ∼115 μm FWHM focus; red circles represent the ∼50 μm case. Uncertainties (∼10%; 1σ) for the velocity are smaller than the symbol size; E_{OD} is obtained with a ∼25% (20%) uncertainty in case of ∼115 μm (50 μm) FWHM focus. The gray dashed line represents a fit of Eq. (3.4) to the concatenated data excluding pulse energies below 0.2 mJ. The black solid line depicts a fit of Eq. (3.7) to the concatenated data. (b) Momentum coupling coefficient C_m obtained from the fitted curve shown as a black solid line in (a).

surface [57]. The empirical constant A was determined to be $3.0 \cdot 10^3\,\mathrm{g\,cm^{-2}\,s^{-1}}$ for Sn for intensities ranging 10^{11}–$10^{12}\,\mathrm{W\,cm^{-2}}$ [56]. Using this value for A in Eq. (3.3), we obtain an ablated mass fraction of 0.1% for the 7 mJ example shown in Fig. 3.2(a). However, the input for A as well as for v above was obtained experimentally at laser intensities one to two orders of magnitude higher than are used in the current investigations. Therefore, we will leave their product as a free fit parameter in the following.

The model (Eqs. (3.2 and 3.3)) predicts a power-law dependence of the propulsion velocity on the laser intensity, which can be translated into a dependence on the total laser energy impinging on the droplet E_{OD} for direct comparison to our measurements by virtue of the relation $I \propto E_{\mathrm{OD}}$, obtaining

$$U = B \cdot E_{\mathrm{OD}}^{5/9}. \tag{3.4}$$

The result of a single fit of Eq. (3.4) to both data sets, excluding low pulse energies $E_{\mathrm{OD}} < 0.2\,\mathrm{mJ}$, yields excellent agreement of this power-law with the data as is shown in Fig. 3.3. This agreement shows that E_{OD} is the correct parameter in scaling the data for the two focusing conditions. We obtain a proportionality constant $B = 34(5)\,\mathrm{m\,s^{-1}\,mJ^{-5/9}}$. Employing the empirical values from literature for A and v in Eqs. (3.2 and 3.3) we obtain a prediction of $\sim 9\,\mathrm{m\,s^{-1}\,mJ^{-5/9}}$. A discrepancy was to be expected as the laser intensities in our experiments fall mostly outside the validated range [56] for Eq. (3.3) and for the estimate of v. Moreover, we disregarded the spherical geometry of the system. In light of these shortcomings, the agreement of the simple power law of Eq. (3.4) with both data sets is striking.

Power-law scaling of the momentum imparted by an expanding plasma has been extensively studied in the context of plasma thrusters as well as nuclear fusion (e.g., see [48, 50]). Empirically, from experiments on planar solid targets, it is found [48] that the ratio of the plasma pressure p and laser intensity I was excellently reproduced by the relation

$$p/I \propto (I\lambda\sqrt{\tau_p})^n, \tag{3.5}$$

with exponent $n = -0.30(3)$ common to all studied materials [48, 50]. This scaling law is found to be valid over a very broad range of target and laser parameters, including the intensities and wavelengths relevant for EUV sources. Employing the scaling relation $U \propto I^{5/9}$ from Eq. (3.4) and linearizing $U \propto p \cdot \tau_p$, we obtain $n = -4/9 \approx -0.44$ from Eq. (3.5). On comparison with the value of n valid for planar solid targets, we note that the difference could well reflect the change in target geometry from plane to spherical surfaces. The proof of the validity of this scaling law (Eq. (3.5)) for the current geometry with respect to λ and τ_p is left for future work.

At lower values of energy-on-droplet E_{OD} in Fig. 3.3, below $\sim$0.2 mJ, the data no longer follow the power law. This is due to the physics governing the *onset* of the plasma formation upon the laser ablation of the metal. The laser fluence at the threshold of ablation is given by [58, 59]

$$F_{\mathrm{th}} = \rho \Delta H \sqrt{\kappa \tau_p} \approx 0.6\,\mathrm{J\,cm^{-2}}, \tag{3.6}$$

with latent heat of vaporization $\Delta H \approx 2.2\,\mathrm{MJ\,kg^{-1}}$ (taking the average of In and Sn in the mixture, both values being within 10% of this average) and thermal diffusivity $\kappa \approx 16.4\,\mathrm{mm^2/s}$ [60]. At the onset, inverse bremsstrahlung does not yet play a role and we have to take into account the reflectivity $\mathcal{R}$ of the surface[3], and multiply Eq. (3.6) with the factor $1/(1-\mathcal{R})$ [63]. For simplicity we take $\mathcal{R}$ to be constant during the duration of the pulse. From these considerations, we obtain the prediction $F_{\mathrm{th}} \approx 5\,\mathrm{J\,cm^{-2}}$, identical to the $\sim$5 J cm^{-2} from plasma modeling [54]. This threshold laser fluence translates into a minimum necessary pulse energy. Such a threshold energy can be straightforwardly included in our model by incorporating an offset pulse energy $E_{\mathrm{OD},0}$, such that the expression for the droplet velocity reads

$$U = \widetilde{B} \cdot (E_{\mathrm{OD}} - E_{\mathrm{OD},0})^{\alpha}. \tag{3.7}$$

Here, the power α is taken as a free parameter since generally $v = v(I)$ [54] and its scaling with intensity could influence the momentum scaling relation given by Eq. (3.4). A single fit of Eq. (3.7) to the full energy range of the concatenated data set (see Fig. 3.3(a)) yields a power $\alpha = 0.59(3)$, consistent with the postulated power of 5/9. The obtained power is also in excellent agreement with recent work of Basko et al. [49] which improved on previous work [47] by analytically treating radiative loss, mostly ignored in literature [49], as well as the charge state distribution of complex ions. A proportionality constant $\widetilde{B} = 35(5)\,\mathrm{m\,s^{-1}\,mJ^{-\alpha}}$ is obtained similar to the result from the fit of Eq. (3.4) above. For the offset we find $E_{\mathrm{OD},0} = 0.05(1)$ mJ, from which we in turn obtain $F_{\mathrm{th}} = 2.4(8)\,\mathrm{J\,cm^{-2}}$ by dividing the offset energy by πR_0^2. This value is in reasonable agreement with the simple estimate that yielded $\sim$5 J cm^{-2}. We conclude that all data are excellently described by a single fit of our model to the data, predicting the power-law scaling of U with E_{OD} in Eq. (3.7) now including a threshold energy. The accurate measurement of the plasma propulsion of a free-falling metallic droplet provides a novel method which enables the detailed differentiation of competing models, and to pinpoint underlying physical processes.

[3] The optical constants are, for pure tin in absence of laser light, $n = 3.92$, $k = 8.65$ (from [61] at 1.2 eV at 523 K) yielding a reflectivity of $\mathcal{R} = 84\%$. For indium a reflectivity of $\mathcal{R} = 91\%$ is obtained from $n = 1.84$, $k = 8.38$ (from [62] at 1.1 μm at 295 K). An estimate of the eutectic optical response is obtained from the averaging the reflectivities, yielding an absorption $1 - \mathcal{R} = 13\%$.

Propulsion efficiency

Having found an adequate description of the plasma propulsion mechanism over the complete measurement range, we can now derive an optimum condition for the laser-induced droplet propulsion. The momentum coupling coefficient $C_\mathrm{m} \equiv p/I = (MU)/E$ [48] given by Eq. (3.5) is a figure of merit in plasma propulsion providing a measure for the propulsion efficiency in terms of total imparted momentum MU per unit laser energy E. Efficient propulsion implies an efficient momentum to kick the droplet. This kick initiates the expansion of the droplet into a thin sheet (see below). Propulsion and expansion speeds are coupled, and their ratio is a function of the focusing conditions [21]. Industrial needs could dictate the minimum size of the focus, as it influences the laser-to-droplet alignment stability. This will further influence the energy efficiency due to the geometrical overlap of laser focus and droplet. For both focusing conditions, however, we can define optimum conditions under which a minimum amount of laser pulse energy (on droplet) is required to reach a given velocity. Less energy is then available to produce, *e.g.*, fast ionic and neutral debris that could limit machine lifetime [13]. Given the offset power law (Eq. (3.7)), C_m can be obtained as a function of pulse energy-on-droplet E_OD (see Fig. 3.3(b)) reaching a maximum at $E_\mathrm{OD,max} = E_\mathrm{OD,0}/(1-\alpha)$ at which point a minimum amount of energy is used to achieve a given velocity. A sequence of optimal pulses, spaced just a few τ_a apart to allow the plasma to recombine, could then be used to achieve a specified velocity. Of course, the relation between the energy-on-droplet E_OD and total laser pulse energy E is given by the geometrical overlap of laser and droplet. Our data (Fig. 3.3(b)) thus indicate that the total energy efficiency is highest, at $E_\mathrm{OD,max}$, for the smallest spot size used in this work.

Indium-tin-plasma vs water-vapor propulsion

Our description of the plasma propulsion of In-Sn micro-droplets shows striking analogies with recent work on water droplets [31]. In that work, mm-sized water droplets are dyed to efficiently absorb 532 nm light from a Nd:YAG laser pulse, at intensities well below the threshold for optical breakdown to avoid plasma generation. Instead, water vapor is expelled at its thermal speed and accelerates the droplet. In the dyed-water experiments, laser light is absorbed in a thin layer of thickness δ, given by the optical penetration depth. This layer first needs to be heated from room temperature T_0 to boiling point T_b, yielding an expression for the threshold fluence $F_\mathrm{th,w} = \rho_\mathrm{w}\,\delta\,c\,(T_b - T_0)$ [31], where c is the specific heat capacity of water and ρ_w is its density. Any additional energy leads to vaporization of the liquid, expelling mass at a thermal velocity $u \approx 400\,\mathrm{m/s}$ which leads to the propulsion of the water droplet. When comparing the onset for propulsion of water

droplets to the threshold fluence for In-Sn (Eq. (3.6)), one observes that for water, the mass affected by the laser is set by the optical penetration depth, whereas for In-Sn it is set by the thermal penetration depth $\sqrt{\kappa\tau_p}$. The energy density required for droplet propulsion is given by the sensible heat for water, and by the latent heat ΔH for In-Sn. The In-Sn droplet surface is shielded from the laser light by the plasma that develops at time scales well shorter than the pulse length. Laser light is absorbed by this plasma layer, heating it to high temperatures (several 10 eV). As a result, a relatively small amount of mass ablated is expelled at high velocities $v \gg u$, thus mass-efficiently propelling the droplet. In conclusion, even though the physical mechanism behind the propulsion of In-Sn and water droplets is different, both processes are described by the forceful directive expulsion of material at a given velocity from a thin layer facing the laser light.

As we will demonstrate below, the fluid-dynamic response to the laser impact described here and in Ref. [31] is completely independent from the exact mechanism of propulsion. Mapping the system to the dimensionless numbers governing fluid dynamics allows for an identical treatment of said response for indium-tin and water. The efficiency of the plasma propulsion process enables the study of the response of the metallic droplet over a much larger parameter space than for water, including the industrially relevant large-Weber-number subspace [43] which the previous experiments on water droplets [31] were unable to probe.

3.3.2 Droplet deformation

The expansion of the droplet for the 115 μm focusing case is studied by changing the time delay between the pulse from the Nd:YAG laser and the shadowgraphy lasers in steps of 100 ns. A stroboscopic movie of the deformation dynamics is thus obtained (see Fig. 3.2) with an adequate temporal resolution. We measure the expanded radius of the droplet over time as shown in Fig. 3.4(a) using the side view shadowgraphs, in which the droplet motion is captured within the depth of field of the imaging optics at all time delays. In addition, the front view shadowgraphs are used to make sure the droplet expands into an axisymmetric shape. For comparison, we also include data from mm-sized water droplets, the deformation of which takes place on a time and length scale several orders of magnitude larger than for the In-Sn data (see inset in Fig. 3.4(a)). However, by appropriately rescaling the data by the initial droplet radius R_0 as the characteristic length scale and the capillary time $\tau_c = \sqrt{\rho R_0^3/\gamma}$ as the characteristic time scale for the droplet expansion and subsequent retraction, we can represent all data in one graph: Fig. 3.4(b). For indium-tin, $\tau_c \approx 14\,\mu$s given its surface tension $\gamma = 538$ mN/m [51]. The expansion dynamics of the droplet can be described in terms of the Weber number $\mathrm{We} = \rho R_0 U^2/\gamma$ [21, 31], a dimensionless number that is a measure for the relative importance of the droplet's kinetic energy compared to its initial surface energy.

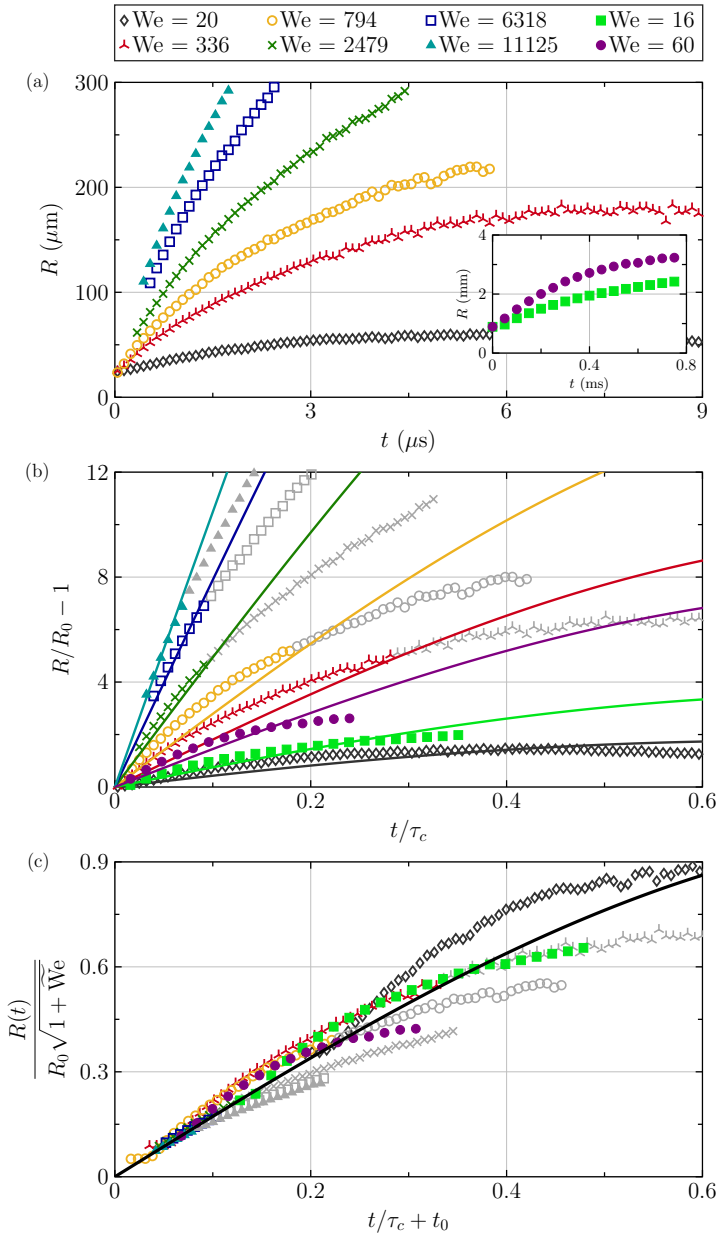

FIGURE 3.4: (Continued on the following page.)

FIGURE 3.4: (Figure is found on the previous page.) Radial expansion of In-Sn and water droplets as function of time. (a) Dimensional plot of the experimental data for In-Sn droplets determined from shadowgraphy (see Fig. 3.2), with Weber numbers calculated using the droplet velocities from Fig. 3.3. The inset shows data for mm-sized water droplets taken from a previous study [31]. (b) Experiments (markers) and theory (solid lines, Eq. (3.8)) in a dimensionless representation. The data points are depicted in gray from the time onward at which formation of ligaments becomes apparent and comparison with the present theory is no longer relevant. Comparison between model and water data taken from Ref. [21]. (c) Experimental data (markers) and theory (solid line) collapsed to a universal curve using a scaled Weber number $\widetilde{\mathrm{We}}$ and time offset t_0 (see main text).

In the limit where the droplet expands into a flat, thin sheet that subsequently recedes due to surface tension an analytical expression can be found for the radius R as function of time t (for the derivation see [21])

$$\begin{aligned}\frac{R(t)}{R_0} &= \cos\left(\sqrt{3}t/\tau_c\right) + \\ &\left(\frac{2}{3}\right)^{1/2}\left(\frac{E_{k,d}}{E_{k,cm}}\right)^{1/2}\mathrm{We}^{1/2}\sin\left(\sqrt{3}t/\tau_c\right),\end{aligned} \tag{3.8}$$

where the parameter $E_{k,d}/E_{k,cm}$ is the partition of the total kinetic energy given to the droplet by the laser impact into a deformation kinetic energy $E_{k,d}$ and propulsion kinetic energy of the droplet's center-of-mass $E_{k,cm}$. This parameter depends on the laser beam profile and can be determined analytically [21]. For all practical purposes in the present study, the laser beam profile can be considered flat, which gives $E_{k,d}/E_{k,cm} = 0.5$ [21]. The water data [31] was obtained with a relatively more focused laser beam, for which $E_{k,d}/E_{k,cm} = 1.8$ was calculated. Figure 3.4(b) shows that the model prediction is in good agreement with the experimental data taking into account that it is derived from first principles and does not incorporate any fitting parameter. In the comparison, we truncate the experimental data where the formation of ligaments becomes apparent in the front view images, as at this point in time the assumption of a thin sheet of constant mass is clearly violated.

With the analytical expression at hand, the indium-tin and water data can be collapsed onto a universal curve by employing a trigonometric identity to rewrite Eq. (3.8) to

$$\frac{R(t)}{R_0\sqrt{1+\widetilde{\mathrm{We}}}} = \sin\left(\sqrt{3}(t/\tau_c + t_0)\right), \tag{3.9}$$

introducing an offset time t_0 and a scaled Weber number $\widetilde{\mathrm{We}}$ that depends on the energy partition ratio $E_{k,d}/E_{k,cm}$:

$$\begin{aligned} \widetilde{\mathrm{We}} &= \frac{2}{3}\frac{E_{k,d}}{E_{k,cm}}\mathrm{We}, \\ t_0 &= \frac{1}{\sqrt{3}}\tan^{-1}\left(\widetilde{\mathrm{We}}^{-1/2}\right). \end{aligned}$$

The data scaled with Eq. (3.9) indeed overlap completely and agree with the now single theoretical prediction (see Fig. 3.4(c)). This collapse demonstrates that the expansion dynamics, given the above scaling relation, are successfully described by a single dimensionless parameter which spans nearly three decades in our experiments. This range includes the conditions relevant for industry [43], enabling the direct application of the results presented in Fig. 3.4 in work on plasma sources of EUV light.

3.4 Conclusions

We demonstrated that a micron-sized free-falling In-Sn micro-droplet hit by a high-intensity 10 ns-long laser pulse is propelled by a plasma pressure "kick". The propulsion dynamics can be well understood in terms of a power law that describes the dependence on the laser-pulse energy and incorporates an offset parameter to account for the threshold of plasma generation over nearly three decades of laser pulse energy. This scaling law provides a useful tool to optimize the momentum coupling of the laser to the target. The description of the propulsion as a short recoil pressure is analogous to that presented in [31], where a millimeter-sized water droplet is accelerated by the directional emission of vapor upon the absorption of light from a short laser pulse. We find remarkable one-to-one correspondences between the two propulsion mechanisms, including the description of an analogous onset effect, even though the physical origins of the propulsion are completely different. Continuing its flight, the droplet expands until fragmentation occurs. By a proper rescaling, we show that all indium-tin and water data can be collapsed onto a universal curve that is accurately described by a previously developed analytical model, here applied for the first time under industrially relevant conditions. The results and scaling laws presented in this work provide a tool to optimize and control the droplet shaping by laser pulse impact for EUV lithography applications.

Chapter 4

Power-law scaling of plasma pressure on laser-ablated tin microdroplets

D. Kurilovich, M. M. Basko, D. A. Kim, F. Torretti, R. Schupp, J. C. Visschers, J. Scheers, R. Hoekstra, W. Ubachs, and O. O. Versolato, Phys. Plasmas **25**, 012709 (2018).

The measurement of the propulsion of metallic microdroplets exposed to nanosecond laser pulses provides an elegant method for probing the ablation pressure in dense laser-produced plasma. We present the measurements of the propulsion velocity over three decades in the driving Nd:YAG laser pulse energy, and observe a near-perfect power law dependence. Simulations performed with the RALEF-2D radiation-hydrodynamic code are shown to be in good agreement with the power law above a specific threshold energy. The simulations highlight the importance of radiative losses which significantly modify the power of the pressure scaling. Having found a good agreement between the experiment and the simulations, we investigate the analytic origins of the obtained power law and conclude that none of the available analytic theories is directly applicable for explaining our power exponent.

4.1 Introduction

High-density laser-produced plasmas find many applications, ranging from inertial confinement fusion [64–66], over the propulsion of small spacecrafts [67, 68], to sources of extreme ultraviolet (EUV) light for nanolithography [13, 18, 19, 42, 69]. The thermodynamic and radiation transport properties, particularly of high-Z laser-produced plasmas (LPPs), are extremely challenging to measure because of the transient nature of these plasmas, combined with complex equations of state and atomic plasma processes. One thermodynamic variable — the pressure — can, however, be elegantly obtained by measuring the propulsion velocity of metallic liquid microdroplets as a result of a laser-pulse impact [20, 70]. In an industrially relevant setting for EUV light production such droplets are irradiated by relatively long ($\sim$ 10–100 ns) laser pulses at modest intensities ($\sim 10^9$–10^{12} W/cm^2), where the laser absorption takes place mostly through the inverse bremsstrahlung mechanism.

If the pulse length is large compared to the hydrodynamic time scale of the ablation flow, a quasi-stationary regime sets in, where the structure of the ablation front only slowly varies in time. The structure of such quasi-stationary ablation fronts has been extensively studied under various simplifying assumptions for more than 40 years [47, 64, 71–76]. However, none of these theoretical works is directly applicable to our system. One of the reasons is the treatment of energy transport by thermal radiation. Another reason is departure from the ideal-gas equation of state (EOS) due to multiple temperature-dependent ionization of the target material. These two effects are of major importance for tin ($Z = 50$) targets at the here considered irradiation intensities [49]. A significant further issue is the non-trivial geometry of the laser-target configuration in our experiments, where a spherical target is irradiated from only one side and an essentially two-dimensional (2D) ablation flow develops. It is likely to alter the scaling laws obtained within one-dimensional (1D) models.

Here, we present measurements of the propulsion velocity of free-falling microdroplets of liquid tin and two of its alloys over three decades in the driving Nd:YAG laser pulse energy, operating at its fundamental wavelength of 1064 nm. The propulsion velocity is obtained by means of high-resolution stroboscopic shadowgraphy techniques. Our data exhibit a remarkable, near-perfect power law dependence of the propulsion velocity on the laser pulse energy, when allowing for a certain threshold energy below which no propulsion occurs. Furthermore, we provide results of simulations performed with the RALEF-2D [32, 33, 77] radiation-hydrodynamic code and compare these critically to the experimental data. We find very good agreement between the simulations and the experimental power law in cases well above the threshold energy, but establish a significant disagreement regarding the threshold behavior itself.

Next, we investigate whether the obtained power law can be derived within the conventional approach based on the approximation of a steady-state planar ablation flow, but corrected for the strong radiative loss. Interestingly, we conclude that none of the analytic theories available in the literature is directly applicable for explaining the power exponent observed in our experiments. We interpret this as evidence that our scaling belongs to a more complex class of scalable phenomena. Two- or three- dimensional effects, possibly combined with an essentially non-steady-state behavior, are crucial. Inevitably, the respective power-law exponents can only be calculated by solving numerically an appropriate system of partial differential equations.

4.2 Experiment

4.2.1 Experimental setup

The experimental setup is described in detail in Ref. [20] and is summarized in the following. Droplets of pure liquid tin (99.995%), or one of its alloys with indium (50%) or antimony (5%), are dispensed from a piezo-driven droplet generator at a repetition rate $\simeq 10\,\mathrm{kHz}$ with a flight speed of $\simeq 12\,\mathrm{m/s}$ in a vacuum environment ($\simeq 10^{-7}\,\mathrm{mbar}$). The droplets relax to a spherical shape with a fixed initial diameter D_0, which slightly varied between different experimental campaigns but stayed in the range $D_0 = 2R_0 \approx 45$–$47\,\mu\mathrm{m}$, where R_0 is the droplet radius.

The produced droplets pass through the focus of an auxiliary He-Ne laser beam, whose scattered light triggers an injection-seeded Nd:YAG drive laser, operating at a 10-Hz repetition rate. The drive laser pulse, emitted at a $\lambda = 1064\,\mathrm{nm}$ wavelength, is circularly polarized and has a Gaussian temporal shape with a duration $t_p = 10.0\,\mathrm{ns}$, defined as the full-width at half-maximum (FWHM). By using an appropriate plano-concave lens, the laser beam is focused down to a circular Gaussian spot. The experiments were performed for three different focusing conditions with spot sizes of $d_{foc} = 50$, 100, and $115\,\mu\mathrm{m}$ (FWHM). Note that due to a finite geometrical overlap, the droplets in all cases capture only a fraction of the full laser pulse energy. The pulse energy is varied over three decades, spanning the range 0.15–300 mJ, as measured by using calibrated energy meters, in a manner that does not affect the transversal mode profile of the laser beam.

The position of the laser-impacted droplet is obtained from shadowgraphs generated by pulsed backlight in combination with long-distance microscopes and CCD cameras. This system provides front-view (at 30° with respect to the drive-laser light propagation direction) and side-view (at 90°) images. By varying the time delay of the backlight pulse with respect to the drive laser pulse, stroboscopic images

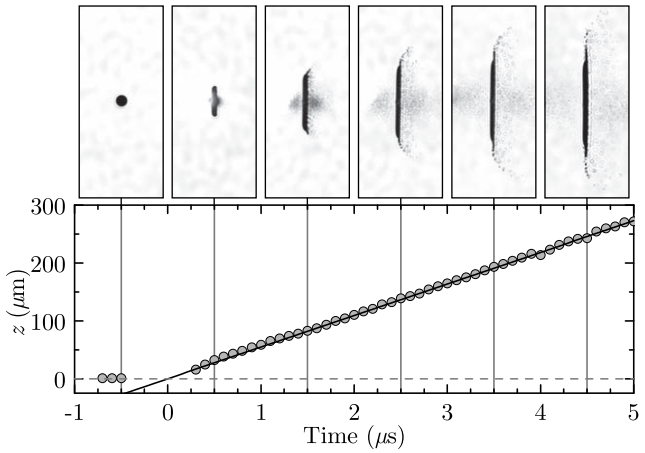

FIGURE 4.1: (Top) Stroboscopic side-view shadowgraph images ($350\,\mu$m×$800\,\mu$m) of subsequent tin microdroplets obtained before and after the interaction with a laser pulse. The laser pulse arrives from the left at $t = 0\,\mu$s. The images represent the case of $E_{od} \approx 2\,$mJ, $D_0 \approx 45\,\mu$m and $d_{foc} \approx 100\,\mu$m (FWHM). (Bottom) The plot shows the time-dependent position of center-of-pixels of images (circles) along the laser propagation axis z as obtained from the image analysis. The undesired capture of the plasma light causes the disruption of the image analysis at $t \lesssim 0.25\,\mu$s. Each data point is an average of ten unique images obtained at the same time delay. The solid line shows a linear fit to the data points. The slope of this line corresponds to the propulsion velocity of the microdroplets.

of consequent droplets are obtained (see Fig. 4.1). The analysis of the images is realized by a code that recognizes the center-of-pixels of the propelled and deformed droplet. Knowing the time delay between the backlight shots with a nanosecond accuracy, the droplet propulsion velocity is obtained from the slope of a linear fit to the time-dependent position of the center-of-pixels.

4.2.2 Experimental results

The measured values of the propulsion velocity U are plotted in Fig. 4.2 versus the *energy-on-droplet* E_{od} that is defined as the fraction of the incident laser energy E given by the geometrical overlap of the spatial beam profile in focus and the droplet; in particular, for a Gaussian beam and a spherical droplet we have

$$E_{od} = E\left(1 - 2^{-D_0^2/d_{foc}^2}\right). \tag{4.1}$$

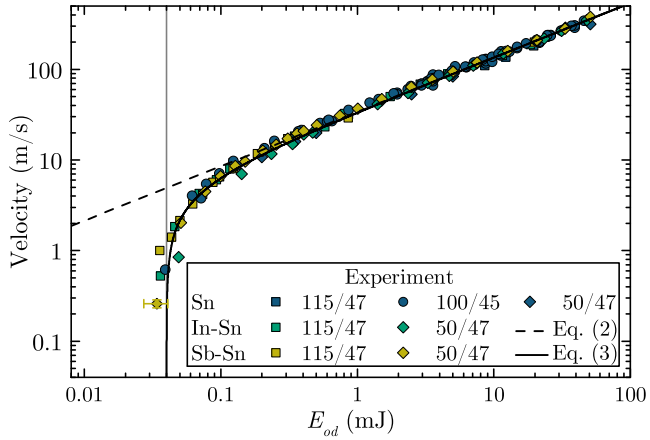

FIGURE 4.2: Measured propulsion velocity U of Sn, In-Sn, and Sb-Sn droplets as a function of the laser energy E_{od} impinging onto the droplet. The experimental uncertainties have the same values (20–25% along the E_{od}-axis and 10% along the U-axis) for all measurements. For better visibility the uncertainties are shown only at the lowest laser energy. The focus diameter $d_{foc}\,(\mu\text{m})$ and the droplet diameter $D_0\,(\mu\text{m})$ for different experimental series are indicated in the legend as d_{foc}/D_0. The dashed line represents a fit of Eq. (4.2) to the concatenated data for $E_{od} \geq 0.2\,\text{mJ}$. A fit of Eq. (4.3) to the full range is depicted as the solid line. The vertical line at $E_{od} = 0.04\,\text{mJ}$ corresponds to the threshold for droplet propulsion as inferred from this fit.

The thus defined energy-on-droplet appears to be a very convenient parameter, characterizing the effective portion of the laser pulse energy that gives rise to a given value of the propulsion velocity U. It also enables the comparison of the results of measurements for different focal spot sizes. As seen from Fig. 4.2, using this energy parametrization all data fall on a single curve.

Figure 4.2 further demonstrates that, above a certain threshold region of $E_{od,a} \approx 0.1 - 0.2\,\text{mJ}$, the dependence $U(E_{od})$ is well represented by a power law

$$U = K_U E_{od}^{\alpha}, \tag{4.2}$$

with constant values of the proportionality factor $K_U\,(\text{m}\,\text{s}^{-1}\text{mJ}^{-\alpha})$ and the exponent α. A fit of a power law to the full concatenated data set, using the energy range $E_{od} \geq E_{od,a}$, yields α =0.60(1). Fitting separately to the individual experimental data sets yields a weighted value of 0.60(1), an identical number, that is bounded by a minimum obtained value of 0.56 and a maximum of 0.63. We note that fitting only the data with a 50-μm focus size gives a slightly larger power, at 0.62(1). This value, however, is still consistent with the aforementioned result of

the fit of the full concatenated data set. Similarly considering only the data from the 100- and 115-μm size focus cases, yields a power of 0.59(1), consistent with the average of 0.60(1) which is the number used in the comparisons in the following. The value obtained for K_U is, in all cases, consistent with $34(3)\,\mathrm{m\,s^{-1}mJ^{-\alpha}}$, where the quoted uncertainty is the error in obtaining the absolute magnification of the imaging system.

For $E_{od} < E_{od,a}$, the $U(E_{od})$ curve deviates downward from the simple power law described by Eq. (4.2), with a threshold at $E_{od} = E_{od,0}$. The parameter range $E_{od,0} < E_{od} < E_{od,a}$ corresponds to a transition regime between the onset of the ablation flow at $E_{od} = E_{od,0}$, and the fully ablative stage at $E_{od} > E_{od,a}$. To incorporate the threshold behavior, the entire set of the experimental points in Fig. 4.2 is fitted by a single shifted power law, defined as

$$U = K_U(E_{od} - E_{od,0})^{\alpha}. \tag{4.3}$$

The value of the offset energy $E_{od,0}$ is obtained by fitting Eq. (4.3) to the experimental data with K_U and α fixed to the values determined above, i.e. $34\,\mathrm{m\,s^{-1}mJ^{-\alpha}}$ and 0.60 respectively. The result is shown in Fig. 4.2 and yields a value of $E_{od,0} = 0.04(1)\,\mathrm{mJ}$. Remarkably, the naive form of Eq. (4.3) is able to capture all the data to excellent accuracy.

These values are consistent with, and in fact nearly identical to, the values found in our previous work ($\alpha = 0.59(3)$, $K_U = 35(5)\,\mathrm{m\,s^{-1}mJ^{-\alpha}}$, $E_{od,0} = 0.05(1)\,\mathrm{mJ}$), dealing with a much smaller data set for solely indium-tin droplets [20]. Consequently, the here demonstrated excellent reproducibility of the data strongly improves the statistical significance of our findings and the broad applicability of the power law. It presents a solid basis for drawing conclusions on the underlying physics.

As is explained in more detail in Section 4.3, the energy $E_{od,a}$ marks the lower boundary of a distinct pattern of laser ablation. Under such conditions, the hot plasma with $T \gtrsim 5$–$10\,\mathrm{eV}$ envelopes the entire front-illuminated (laser-facing) hemisphere of the droplet, the velocity field across the laser absorption zone approaches that of a quasi-spherical flow, and all the laser flux contributing to E_{od} is efficiently absorbed in the ablated plasma cloud by the inverse bremsstrahlung mechanism. Accordingly, we designate the regime above $E_{od,a}$ as the *fully ablative regime*. In this regime the peak laser intensity on target spans the range $10^9\ \mathrm{W/cm^2} < I_l < 3 \times 10^{11}\ \mathrm{W/cm^2}$.

4.3 Simulation

4.3.1 RALEF-2D code

The simulations reported in this work have been performed with the two-dimensional (2D) radiation-hydrodynamics code RALEF [32, 33], which has lately been extensively used to simulate laser-driven, droplet-based EUV sources for nanolithography applications [49, 77, 78]. The hydrodynamics module of RALEF is based on the upgraded version of the CAVEAT package [79], where the second-order Godunov-type algorithm on an adaptive quadrilateral grid is used. The thermal conduction and the spectral radiation transfer (in the quasi-static approximation) are treated within a unified symmetric semi-implicit scheme [32, 80] with respect to time discretization. To describe the spatial dependence of the spectral radiation intensity, the classical S_n method is used, combined with the method of short characteristics [81] to integrate the radiative transfer equation.

The equation of state (EOS) of tin is constructed by using the FEOS model [82] that provides, within a unified model, an adequate and thermodynamically consistent description of high-temperature plasma states together with the low-temperature liquid-gas phase coexistence region. The model for thermal conductivity is based on a semi-empirical expression for the transport cross section of the electron-ion collisions [83], which enables a smooth matching of the Spitzer plasma conductivity to that of metals near normal conditions.

All the simulations are performed for a spherical droplet of pure tin with initial radius $R_0 = 25\,\mu$m and initial density $\rho_0 = 6.9\,\mathrm{g/cm^3}$, assuming that slight differences between the physical properties of pure Sn and its two alloys used in the experiments are insignificant. The adaptive numerical mesh has a topological structure as displayed in Fig. 4.3. It extends with 360 zones over the π interval of the polar angle θ, and with 350 radial zones over the interval $20\,\mu\mathrm{m} \le r \le 1\,\mathrm{mm}$. This totals to 142 200 mesh cells over the simulated half-circle in the rz plane. The mesh is progressively refined in the radial direction towards the droplet surface to resolve the skin layer of the liquid tin. The minimum cell thickness of this layer is 4.5 nm. The outer region $25\,\mu\mathrm{m} \le r \le 1\,\mathrm{mm}$ is initially filled with a tenuous tin vapor at a density of $\rho_{v0} = 10^{-10}\,\mathrm{g/cm^3}$.

In all the simulation runs, the same Gaussian temporal power profile of the 1064 nm laser pulses is used, with the pulse duration $t_p = 10\,\mathrm{ns}$ (FWHM), peaking at $t = 1.5t_p = 15\,\mathrm{ns}$. The spatial laser profile is also Gaussian, with two values of the focal spot diameter (FWHM): $d_{foc} = 115\,\mu$m (series A) and $d_{foc} = 50\,\mu$m (series B). The propagation and absorption of the laser light are calculated within a hybrid model [84], which accounts for refraction in the tenuous corona. In addition,

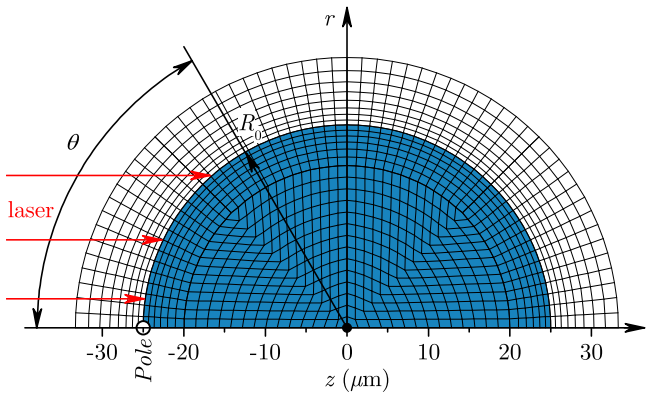

FIGURE 4.3: Schematic view of a spherical tin droplet of radius $R_0 = 25\,\mu$m (shaded), projected onto the computational domain with the outer radius of 1 mm (not shown here) in the rz-plane. The depicted view is a crude version of the numerical mesh used in the simulation, assuming unpolarized incident laser light.

it ensures a physically correct description of reflection from the critical surface, including the Fresnel reflection from the metal-vacuum interface. Lastly, the incident light is assumed to be unpolarized.

For all cases in the fully ablative regime, radiative energy transport is important. Radiation generation and transport is treated with the same opacity model as in Ref. [78], where the conversion efficiency into the 13.5-nm EUV emission is investigated for a CO_2-laser-driven plasma. The angular dependence of the radiation intensity is modeled with the S_6 quadrature, while the spectral dependence is simulated with 28 discrete spectral groups of variable width. Two spectral groups belong to the 2% band at 13.5 nm, where the strongest emission from the Sn plasma is expected at sufficiently high laser intensities.

4.3.2 Simulation results

Droplet propulsion

The calculated propulsion velocity U for various E_{od} values is plotted in Fig. 4.4. In the RALEF code, it is computed as the velocity of the center of mass, comprising all the material with the density in excess of 1 % of its maximum value at the time $t = t_f = 200$ ns. Similarly to the experimental results, for $E_{od} > 0.1 - 0.2$ mJ, the dependence $U(E_{od})$ is almost a perfect power law: the deviations of the calculated

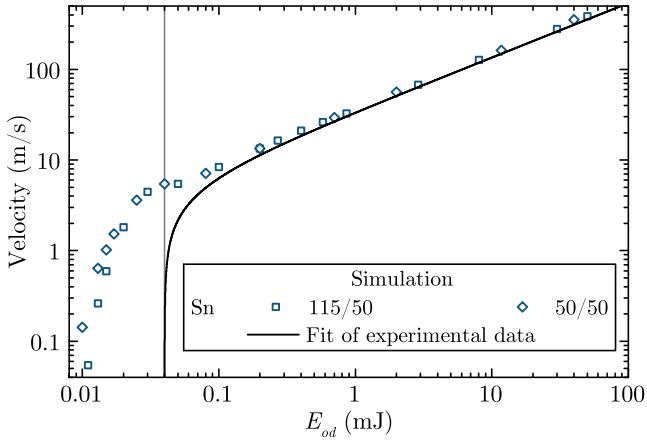

FIGURE 4.4: Dependence of the propulsion velocity U on E_{od} calculated with the RALEF-2D code. The focus diameter d_{foc} (μm) and the droplet diameter D_0 (μm) for different simulation series are indicated in the legend as d_{foc}/D_0.The black curve represents the best fit to the experimental points (see Fig. 4.2). The vertical line at $E_{od} = 0.04\,\mathrm{mJ}$ corresponds to the threshold for droplet propulsion as inferred from that fit.

points from Eq. (4.2) with the best-fit values of

$$K_U = 36.0(3)\,\mathrm{m\,s^{-1}mJ^{-\alpha}}, \quad \alpha = 0.610(5), \tag{4.4}$$

calculated for the combined set of points from series A and B in the range $E_{od} \geq 0.2\,\mathrm{mJ}$, do not exceed $\pm 2.5\%$ — which is practically the intrinsic accuracy of the simulations. Fig. 4.4 confirms that within the same $\pm 2.5\%$ accuracy the energy-on-droplet E_{od} proves indeed to be an adequate universal parameter, which unites the $d_{foc} = 115\,\mu$m and $d_{foc} = 50\,\mu$m points into virtually a single curve. For the variation of the coefficient K_U with the droplet size R_0 and the laser pulse duration t_p, we refer to the Appendix.

Judging from Fig. 4.4, the agreement between the calculated and the measured U values in the fully ablative regime could hardly be better: the deviations from the best experimental fit do not exceed 11%, which lies within the experimental errors. However, the droplet diameter $D_0 = 50\,\mu$m, used in the simulations, slightly exceeds the actual values of $D_0 \approx 45$–$47\,\mu$m. For instance, the correction to a smaller value $D_0 = 46\,\mu$m would raise the calculated U values in the fully ablative regime in Fig. 4.4 by some 20%, leaving the power α unchanged. The fact that the model tends to slightly overestimate the propulsion velocity can, on the one hand, be attributed to a systematic experimental uncertainty, combining possible

measurement errors in the spatial beam profile and the droplet diameter. Alternatively, the RALEF simulations may, for example, systematically underestimate the radiation energy losses, whose modeling could still noticeably be improved.

All in all, a very good agreement between the simulation and the experiment is found in the fully ablative regime. Particularly, concerning the scaling exponent α, the best-fit experimental value $\alpha = 0.60(1)$ is practically the same as the theoretical value in given Eq. (4.4). This provides a strong evidence that the RALEF code sufficiently accurately accounts for the key physical processes governing the Sn plasma dynamics in this regime. Therefore, it can be used to extract additional information about the relative role of these processes.

At the low energies $E_{od} < 0.1\,\mathrm{mJ}$, the simulation results begin to significantly deviate from the experimental values. Here, we have to deal with the initial phase of the onset of ablation, which is controlled by physical processes that are quite distinct from those governing the fully ablative regime. The key role in this initial phase should belong to an adequate modelling of laser-optical properties and propagation of a non-steady thermal wave across a thin surface layer of tin. Under such conditions, this layer is driven into a non-trivial thermodynamic state of superheated metastable liquid, followed by a phase transition into a state of dense hot vapor. We leave the full investigation of this regime for future work.

Plasma characterization in the fully ablative regime

A general perception of the plasma dynamics in the fully ablative regime can be obtained from Fig. 4.5, which displays the 2D density and temperature distributions for the two cases of $E_{od} = 0.2\,\mathrm{mJ}$ and $30\,\mathrm{mJ}$ at time $t = 15\,\mathrm{ns}$, coinciding with peak laser power. As is seen in Figs. 4.5(b) and (c), a characteristic feature of the fully ablative regime is a stabilized geometry of the plasma flow across the laser absorption zone. The latter manifests itself in Figs. 4.5(e) and (f) as the region with highest plasma temperatures. Note that the peak temperature in the ablative regime varies with E_{od} over a wide range of $5\,\mathrm{eV} \lesssim T \lesssim 100\,\mathrm{eV}$. In all cases with $E_{od} \geq E_{od,a}$, in the middle of the pulse, the plasma plume attains a size of several R_0 and occupies the entire 2π of the solid angle above the illuminated droplet hemisphere; the velocity field stabilizes to a quasi-steady, quasi-spherically diverging pattern; the laser-absorption zone itself reaches its maximum size, which becomes practically independent of E_{od}. Intuitively, it is clear that once the 2D (or 3D) geometry of the plasma flow and laser absorption settles down to a stable pattern, the principal ablation parameters (like the characteristic pressure, temperature, ablation velocity, etc.) can be expected to become scalable. On the other hand, in the low-energy cases with $E_{od} < E_{od,a}$ (see Figs. 4.5(a) and (d)), intense laser absorption takes place in a narrow plasma plume near the target pole while a large portion of the incident flux contributing to E_{od} is reflected from a cooler and

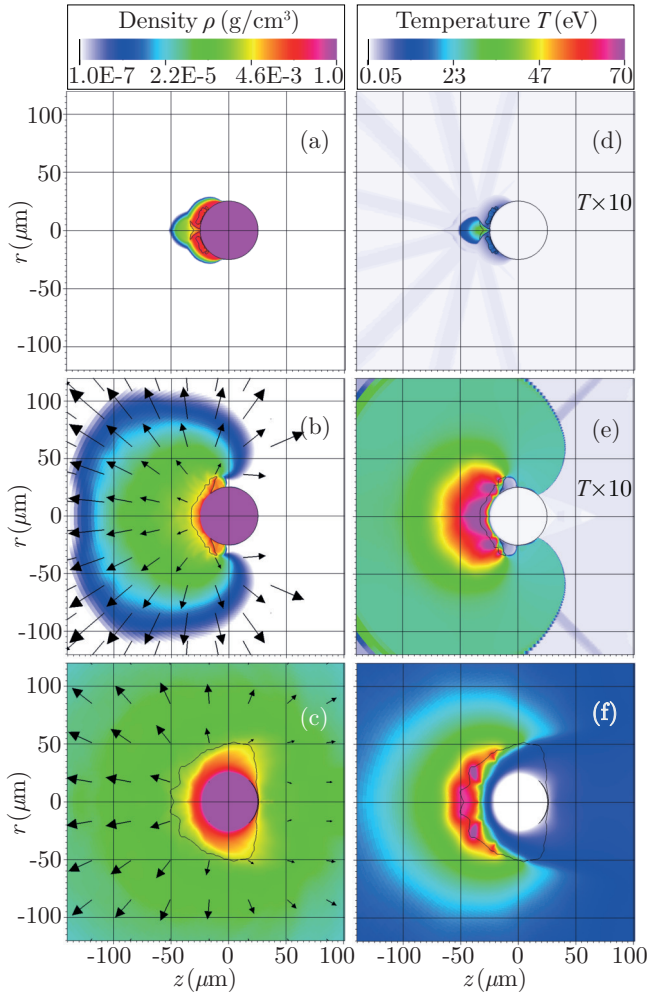

FIGURE 4.5: Calculated 2D density and temperature color maps for the cases E_{od} = 0.06 mJ (a, d), 0.2 mJ (b, e), and 30 mJ (c, f) $d_{foc} = 115\,\mu$m at $t = 15$ ns when the laser power peaks. The black curve is the isocontour of the free electron density $n_e = 0.1 n_{cr} = 10^{20}\,\mathrm{cm}^{-3}$. Black arrows in (b, c) indicate the velocity field in the outflowing plasma.

sharper liquid-vapor boundary at $\theta \gtrsim 40°$–$50°$. Therefore, the ablation parameters from these low-energy cases cannot be expected to be scalable in the same way as those in the fully ablative regime.

Fig. 4.5 also demonstrates that the ablation flow is subject to hydrodynamic instabilities, the most salient of which appears to be the self-focusing instability due to laser refraction in the underdense plasma, inherent in the laser deposition model [84]. The resulting irregular fluctuations of the plasma parameters in space and time manifest themselves as "spotty" temperature distributions and "wavy" n_e isocontours in Fig. 4.5. The temporal variation of the ablation pressure at a fixed location, illustrated in Fig. 4.6 for the target pole, becomes especially violent for low E_{od} values.

Although the self-focusing instability has a clear physical origin, the amplitude of the ensuing fluctuations tends to be overestimated in the present RALEF simulations (especially on length scales comparable to, or smaller than the laser wavelength λ) due to the absence of diffraction effects in the laser propagation model [84]. However, when averaged over space and time, the impact of this "noise" on the calculated U values turns out to be negligible, i.e. on the level of $\pm 1\%$, as ascertained by dedicated computer runs. Having verified it in 2D, we expect no more than only a moderate, by about a factor of 1.5, increase of this effect in the full 3D approach. This is similar to what has firmly been established for the nonlinear stage of the Rayleigh-Taylor instability [85].

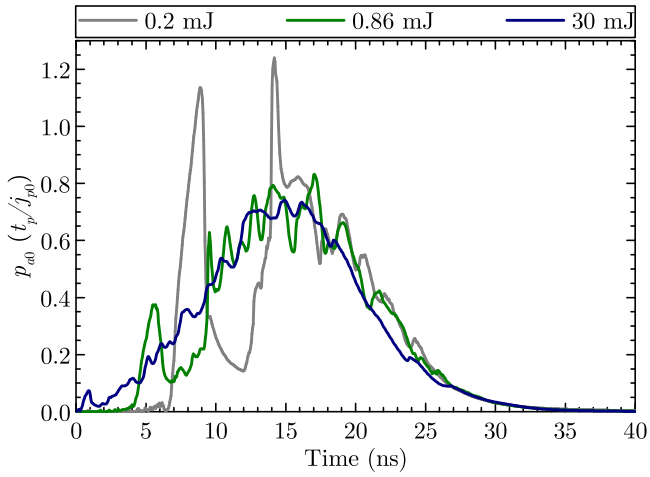

FIGURE 4.6: Calculated temporal dependence of the ablation pressure at the droplet pole $p_{a0}(t)$ normalized by the quotient t_p/j_{p0} of the laser pulse length and the pressure impulse for three values of E_{od} and $d_{foc} = 115\,\mu$m.

Ablation pressure

The ablation-plasma parameter most directly related to the propulsion velocity U is the ablation pressure. More specifically, the velocity U can be determined from the relationship

$$MU = P, \tag{4.5}$$

where M is the total mass, and P is the total momentum of the liquid tin at a certain moment $t_f \gg t_p$. As the entire simulated configuration is axisymmetric, the total momentum vector P lies along the z axis. In our case, the results become insensitive to t_f for $t_f \gtrsim 100\,\text{ns}$, thus we present results for $t_f = 200\,\text{ns}$. From the simulations, we learn that the ablated mass fraction δ_M, defined as the relative fraction of the total tin mass with $\rho < 0.1\,\text{g/cm}^3$, does not exceed 10% for the entire range of $E_{od} \leq 40$ mJ (see Tables 4.1 and 4.2). The subsequent deformation of the ablated surface is not significant (see Fig. 4.5). Then, the propulsion momentum P can be evaluated as

$$P = 2\pi R_0^2 \int_0^\pi j_p(\theta) \sin\theta \cos\theta \, d\theta, \quad j_p(\theta) = \int_0^{t_f} p_a(t,\theta)\, dt, \tag{4.6}$$

where $p_a(t,\theta)$ is the ablation pressure at the spherical droplet surface as a function of time t and polar angle θ, and $j_p(\theta)$ is the local impulse of the ablation pressure. Note that θ is measured with respect to the negative direction of the rotation axis z, as is shown in Fig. 4.3.

Equations (4.5) and (4.6) can be used to relate the established scaling of U with E_{od} in Fig. 4.2 to existing analytic scaling laws for the ablation pressure p_a. However, all the previous analytic results on the scaling of p_a with the incident laser flux I_l have been obtained under a few assumptions. It is assumed that the ablation flow either (i) has a 1D planar geometry (p_a is constant in space), or (ii) is in a steady state (p_a is independent of time), or both [75]. Unfortunately, neither of these assumptions can be considered as adequate for our situation. Nonetheless, the effects of the spatial, along the droplet surface, and the temporal variations of the ablation pressure $p_a(t,\theta)$ can be separated as follows.

One can rewrite Eq. (4.6) as

$$P = \pi R_0^2 \, j_{p0} \, \langle \bar{j}_{p\theta} \rangle, \quad j_{p0} \equiv j_p(0) = \int_0^{t_f} p_a(t,0)\, dt, \tag{4.7}$$

where

$$\langle \bar{j}_{p\theta} \rangle = 2 \int_0^\pi \bar{j}_p(\theta) \sin\theta \cos\theta \, d\theta, \quad \bar{j}_p(\theta) \equiv j_p(\theta)/j_{p0}. \tag{4.8}$$

Our simulations demonstrate that in the fully ablative regime the dimensionless *spatial form-factor* $\langle \bar{j}_{p\theta} \rangle$ of the pressure impulse barely depends on the incident laser flux when the focal spot is fixed (see Tables 4.1 and 4.2). For $d_{foc} = 115\,\mu$m, for instance, it fluctuates in the range $\langle \bar{j}_{p\theta} \rangle \approx 0.57$–$0.59$, remaining virtually constant within our simulation accuracy. Hence, as long as we can neglect small variations of the mass M and size R_0 of the irradiated droplet, the problem of the analytic derivation of the scaling of U with E_{od} is reduced to the derivation of the analogous scaling for the local (at the pole) pressure impulse j_{p0}. Before tackling this issue, we provide some additional information on the angular dependence of the ablation pressure that might be helpful for a general analysis of the hydrodynamic response of liquid droplets to laser pulses [20, 21].

TABLE 4.1: Calculated ablation parameters (propulsion velocity U, ablated mass fraction δ_M, radiative loss fraction ϕ_r, laser absorption fraction $f_{la,od}$, spatial form-factor of ablation pressure $\langle \bar{j}_{p\theta} \rangle$) for a selection of laser energies with $d_{foc} = 115\,\mu$m.

E_{od} (mJ)	0.2	0.86	2.88	8.06	30
U (m/s)	13.5	32.7	67.4	128	280
δ_M	0.006	0.009	0.016	0.034	0.085
ϕ_r	0.23	0.35	0.51	0.64	0.74
$f_{la,od}$	0.83	0.91	0.93	0.92	0.96
$\langle \bar{j}_{p\theta} \rangle$	0.595	0.571	0.567	0.580	0.585

TABLE 4.2: Same as Table 4.1 but for $d_{foc} = 50\,\mu$m.

E_{od} (mJ)	0.2	0.7	2.0	11.75	40
U (m/s)	13.4	29.4	56.2	162	354
δ_M	0.006	0.008	0.013	0.042	0.093
ϕ_r	0.22	0.33	0.44	0.63	0.69
$f_{la,od}$	0.77	0.89	0.94	0.93	0.97
$\langle \bar{j}_{p\theta} \rangle$	0.503	0.508	0.508	0.529	0.568

Fig. 4.7 shows several angular profiles of the normalized pressure impulse $\bar{j}_p(\theta)$, calculated with the RALEF code. Despite the fact that the $\bar{j}_p(\theta)$ curve for the highest-energy case $E_{od} = 30\,$mJ is clearly broader than those for lower pulse energies, its integral (see Eq. (4.8)) remains practically the same because of the negative contribution from the backward hemisphere $\theta > 90°$. A salient local rise of $\bar{j}_p(\theta)$ at $\theta \gtrsim 150°$ for the 2-mJ case is explained by the plasma flowing around the droplet and accumulating on its horizontal axis. It leaves a local cloud of relatively

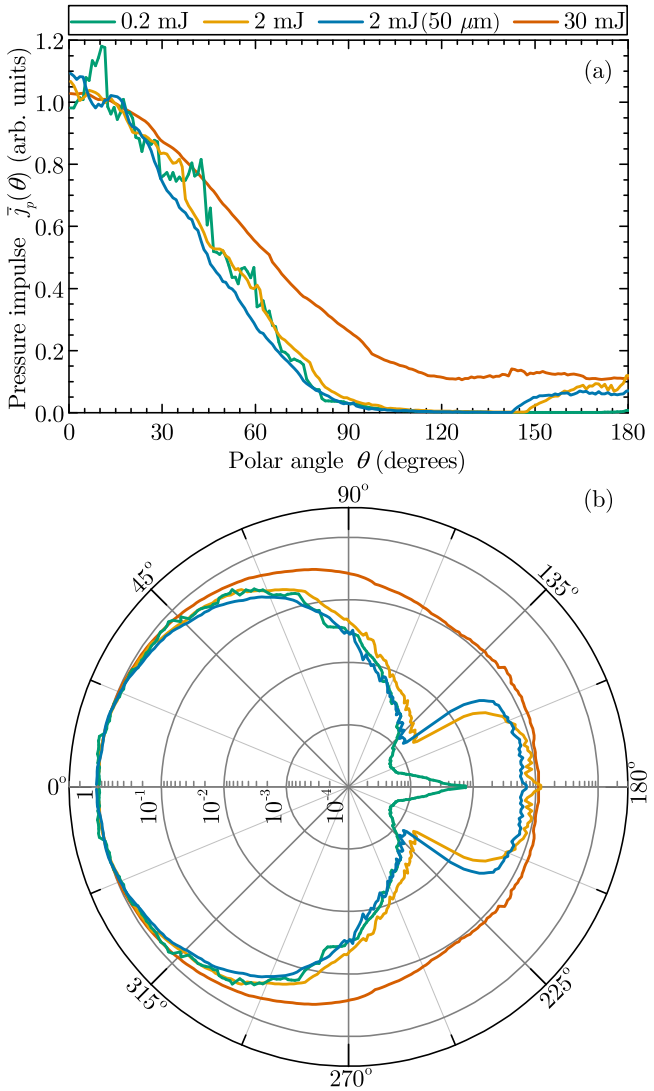

FIGURE 4.7: (a) Calculated variation of the normalized pressure impulse $\bar{j}_p(\theta)$ along the surface of the spherical droplet. The polar angle θ is measured relative to the direction towards the drive laser. Shown are three cases with E_{od} = 0.2, 2.0, and 30 mJ for the focal spot d_{foc} = 115 μm, and, for comparison, one case with E_{od} = 2.0 mJ for d_{foc} = 50 μm. (b) Same as (a) but in the polar plot representation with the radial coordinate in logarithmic scale.

dense and hot vapor, which exerts a noticeable backward pressure onto the droplet for some 30–50 ns after the laser has already been off. We further note that, for the same $E_{od} = 2\,\mathrm{mJ}$, a tighter laser focus (the $d_{foc} = 50\,\mu\mathrm{m}$ curves) produces an only slightly narrower pressure profile $\bar{j}_p(\theta)$.

4.4 Analytic scaling laws

Having found an excellent agreement between the experiment and simulations, we will attempt to derive the obtained scaling law analytically on the basis of an appropriately simplified model. Additional information, available from the simulations, provides guidance for working out such a model.

Analytic scaling laws are usually derived for the ablation pressure p_a as a function of the *hydrodynamically absorbed flux* I_{lh} ($\mathrm{W/cm^2}$), assumed to be constant in time and fully converted into the kinetic and internal energy of the ablated material [75]. To simplify the argumentation, we focus our attention on the simulations (series A) with a fixed spot size $d_{foc} = 115\,\mu\mathrm{m}$. Then, because all the pulses have the same temporal profile, the polar incident flux $I_{l,0}(t)$, the incident laser energy E, and the energy-on-droplet E_{od} are all directly proportional to one another, as well as to the polar energy fluence $F_{l,0} = \int I_{l,0}(t)\,dt$. Consequently, an approximate analytic scaling of U with E_{od} could be obtained by (i) relating the incident laser fluence $F_{l,0}$ to the hydrodynamically absorbed one $F_{lh,0}$, and (ii) making an assumption that the time-integrated quantities j_{p0} and $F_{lh,0} = \int I_{lh,0}(t)\,dt$ scale with one another in the same way as p_a and I_{lh} in a steady-state planar 1D ablation front, for which analytic results are available. Here, we assume that the droplet mass M and the 2D form-factor $\langle \bar{j}_{p\theta} \rangle$ in Eqs. (4.5) and (4.7) are constant. Note that assumption (ii) is by no means obvious, and might, in fact, be rather inaccurate.

4.4.1 Laser absorption and radiative losses

There are two main loss mechanisms that reduce the incident laser energy fluence $F_{l,0}$ to the hydrodynamically absorbed one $F_{lh,0}$, namely, partial reflection of the laser light and radiative losses. Accordingly, since $F_{l,0}$ is directly proportional to E_{od}, we can, following our logic, introduce a *hydrodynamically absorbed energy-on-droplet*

$$E_{od,h} = f_{la}(1 - \phi_r)E_{od}. \tag{4.9}$$

In Eq. (4.9) f_{la} is the laser energy absorption fraction, and ϕ_r is the fraction of the absorbed laser energy which escapes from the plasma by thermal emission. Having introduced effective corrections for the laser reflection and radiative losses by means of Eq. (4.9), we take the next step and relate the resulting scaling of j_{p0}

with $E_{od,h}$ to an analytic scaling of p_a with I_{lh} predicted by an appropriate 1D model. If a close agreement were found, we could accept the invoked 1D model as an appropriate one for the interpretation of our experiments.

Strictly speaking, both factors f_{la} and $(1-\phi_r)$ in Eq. (4.9) must be calculated at the target pole. But, even a simplest analytic model for evaluating f_{la} and ϕ_r would be too cumbersome for the present work [49]. Instead, we take their values from the RALEF simulations. The problem, however, is that the local polar value of ϕ_r cannot be extracted from the simulations. Moreover, it is an ill-defined quantity because of the non-local nature of radiation transport. Thus, we are forced to use the integral values of ϕ_r, calculated for the whole plasma volume and listed in Tables 4.1 and 4.2. For the laser absorption, whose impact on the scaling is considerably less important ($\Delta\alpha \approx 0.03$), we also use the integral values of $f_{la} = f_{la,od}$, calculated for the laser energy fluence over the cross-section πR_0^2 of the droplet. These values are consistent with the integral values of ϕ_r and exhibit weaker instability variations than the local polar values $f_{la,0}$.

First of all, we note that the calculated values of ϕ_r, ranging from $\simeq 20\%$ to $\gtrsim 70\%$ as E_{od} increases from 0.2 mJ to 40 mJ, provide clear evidence of the important role played by radiative losses in our situation. For the scaling exponent it is important that the coefficient $(1-\phi_r)$ changes by about a factor of 2.5–3 over the considered range of E_{od}, which implies an exponent shift by $\Delta\alpha \approx 0.17$.

Fig. 4.8 shows the dependence of the calculated pressure impulse j_{p0} on the incident, E_{od}, and hydrodynamically absorbed, $E_{od,h}$, energy-on-droplet. Solid lines represent the respective power-law fits, that yield the following exponents.

$$j_{p0} \propto E_{od}^{0.583\pm0.005} \propto E_{od,h}^{0.724\pm0.014}. \tag{4.10}$$

The results of the fits significantly differ from one another. This difference of $\Delta\alpha \approx 0.14$ provides a quantitative measure of the influence of radiative losses on the discussed scaling law. In fact, this influence is even stronger ($\Delta\alpha \approx 0.17$) since the two factors f_{la} and $(1-\phi_r)$ in Eq. (4.9) change in opposite directions (see Tables 4.1 and 4.2). Clearly, it is the second exponent $\alpha = 0.724(14)$ that should be compared with the known analytic scalings for $p_a(I_{lh})$. A noticeably larger statistical uncertainty in this exponent (±0.014 versus ±0.005, thus comparable to the experimental error), related to the goodness of fit, is apparently caused by using the integral values of ϕ_r and f_{la}, which "feel" the 2D ablation geometry of a spherical droplet.

Note that the exponent $\alpha = 0.583(5)$ for the $j_{p0}(E_{od})$ dependence differs slightly from the previously quoted value of $\alpha = 0.610(5)$ for the $U(E_{od})$ scaling (see Section 4.3.2). This difference of $\Delta\alpha \approx 0.03$ arises from the fact that the remaining liquid mass M in Eq. (4.5) decreases by about 9% as E_{od} increases from 0.2 mJ to 30 mJ, and less impulse is needed to attain a given velocity U.

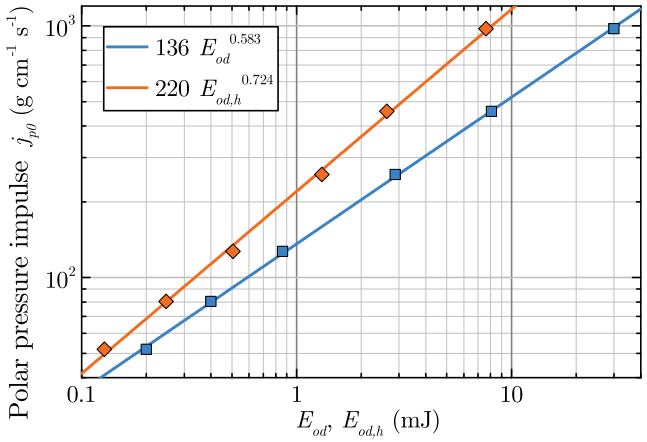

FIGURE 4.8: Calculated pressure impulse j_{p0} at the illuminated droplet pole as a function of the energy-on-droplet E_{od} for the $d_{foc} = 115\,\mu$m case, and of the radiatively-corrected energy-on-droplet $E_{od,h}$.

4.4.2 Effects of the equation of state

Well-known theoretical models of 1D quasi-stationary ablation fronts, based on the ideal-gas equation of state (EOS) with the adiabatic index $\gamma = 5/3$, yield two limiting scaling laws for the ablation pressure. Namely, the one for the case where laser absorption occurs in an infinitely thin layer at the critical surface [47, 71, 74] (case I), and the other one for the case where laser light is absorbed in an extended region by the inverse bremsstrahlung mechanism before reaching the critical surface [47, 86, 87] (case II),

$$p_a \propto \begin{cases} I_{lh}^{2/3}, & \text{case I (ideal-gas EOS)}, \\ I_{lh}^{7/9} L^{-1/9}, & \text{case II (ideal-gas EOS)}. \end{cases} \tag{4.11}$$

In case II, an additional relevant parameter enters the scaling, which is the density-gradient length L in the absorption zone. For quasi-spherical (or cylindrical) diverging flows, where a steady-state solution with a sonic point exists, L should be set equal to the radius of the sonic point [86]. In the planar geometry, where no steady-state solution is possible [86], one can assume the laser to be absorbed in a non-steady rarefaction wave in expanding plasma, where $L \propto c_s t$, and c_s is the characteristic sound velocity. In this way, one arrives at yet another well-known analytic scaling $p_a \propto I_{lh}^{3/4} t^{-1/8}$, applicable to non-steady planar ablation flows with the ideal-gas EOS [47, 71, 86, 88].

All the above analytic scalings with rational-number exponents, based on the ideal-gas EOS, can definitely be applied to interpretation of experiments on low-Z targets (like plastic foils) that are fully ionized by a sufficiently high laser energy flux. None of them, however, can be employed in our case, where a temperature-dependent ionization of tin ($Z = 50$) changes the appropriate planar analytic scalings in Eq. (4.11) to [49]

$$p_a \propto \begin{cases} I_{lh}^{0.56}, & \text{case I (Sn EOS)}, \\ I_{lh}^{0.64} L^{-0.18}, & \text{case II (Sn EOS)}. \end{cases} \tag{4.12}$$

The experimental situation analyzed here lies between these two cases but closer to case II. We compare the exponent $\alpha = 0.724(14)$ in Eq. (4.10) with $0.56 \lesssim \alpha \lesssim 0.64$ in Eq. (4.12). The effect of variation of the density-gradient scale L with the laser intensity I_{lh} for case II is small and only enhances the discrepancy because L can only grow with I_{lh}. From comparison between Figs. 4.5(b) and (c) one infers that the radius of the absorption zone increases by no more than a factor of 1.7 as E_{od} increases from 0.2 mJ to 30 mJ, implying an effective reduction of the scaling exponent by $\Delta\alpha \approx -0.02$.

Thus, a good agreement with the appropriate analytical scaling could have been claimed if Fig. 4.8 demonstrated $j_{p0} \propto E_{od,h}^{\alpha}$ with $0.56 \lesssim \alpha \lesssim 0.62$ — which is obviously not the case. A superficial observation that the scaling (4.10) of j_{p0} with $E_{od,h}$ is very close to the theoretical result $p_a \propto I_{lh}^{3/4}$ (with $t \approx t_p$ being fixed) should be qualified as incidental. Summarizing, we conclude that the scaling (4.2), (4.4) of the propulsion velocity U with the energy-on-droplet E_{od}, established in this work, cannot be derived from the previously published 1D analytic models of the laser ablation fronts.

4.5 Conclusion

Having performed an extensive series of experiments with Nd:YAG laser pulses at different focusing conditions, we have found that within a certain range of laser-pulse energies, covering more than three decades in magnitude, the propulsion velocity of tin droplets scales as a power law $U \propto E_{od}^{\alpha}$ of the energy-on-droplet E_{od} (the incident laser energy intercepted by the cross-section of the droplet). The theoretical analysis, based on 2D simulations with the radiation-hydrodynamics RALEF code, has revealed that the scalability range corresponds to a fully developed regime of laser ablation, where the zone of laser absorption (by inverse bremsstrahlung) in the ablated plasma settles to a stable configuration. For droplets with radii $R_0 \approx 25\,\mu$m it starts at $E_{od} \gtrsim 0.1$–0.2 mJ. The scaling exponent $\alpha = 0.610(5)$, obtained from the RALEF results, agrees perfectly with the experimental value of

$\alpha = 0.60(1)$. The performed analysis demonstrates how the propulsion of metallic microdroplets by a laser-pulse impact can be a good probe for the plasma ablation pressure.

It should be noted that our study was done under a rather unique combination of conditions. A spherical target composed of a high-Z material was irradiated from one side and propelled by an essentially 2D ablation flow. Since the vast majority of previous measurements of the laser ablation pressure were done on low-Z planar targets or on pellets with spherically symmetric irradiation geometry (see, e.g., Refs. [89–93]), we chose to avoid direct comparison of our results to those obtained in these other works, as spurious coincidence of two numbers from different experiments could obfuscate the underlying physics. Instead, we focused our efforts on analyzing the main physical effects that determine our scaling power.

A thorough examination, facilitated by additional information from the RALEF simulations, of the physical processes governing the fully ablative regime in our series of experiments has revealed that the scaling law cannot be directly derived from any of the existing analytic models of quasi-steady 1D ablation fronts. Moreover, this cannot be done even after the effects of radiation energy losses and realistic EOS of tin have been accounted for. The cause must be a complex, essentially 2D (or even 3D) structure of the ablation plasma flow, where the non-local energy transport by thermal radiation in both lateral and radial directions plays an important role. An additional complication comes from the finite pulse length $t_p = 10\,\mathrm{ns}$. It is difficult to justify the steady-state approximation, usually implied by analytic evaluation of the scaling exponent, when t_p remains fixed. While the timescale of flow relaxation [49] to a quasi-steady state is comparable with t_p at $E_{od} = 0.2\,\mathrm{mJ}$, it decreases by about a factor of 3–4 at the upper end $E_{od} = 30$–$50\,\mathrm{mJ}$ of the explored range.

In conclusion, the established scaling of the plasma-propulsion velocity U of tin microdroplets with laser energy E_{od} belongs to a class of scaling laws where theoretical evaluation of the scaling exponent requires the numerical solution of partial differential equations that capture the relevant physical effects in two- or three-dimensions.

Appendix: Dependence of the propulsion velocity on the droplet size and laser pulse duration

Having established the scaling Eqs.(4.2) and (4.4) of the propulsion velocity U with the energy-on-droplet E_{od}, one can, following the logic of Section 4.3.2 and making some reasonable assumptions, evaluate the dependence of U on the droplet radius R_0 and the laser pulse duration t_p. This might be useful for practical applications.

First of all, we suppose that the exponent α in Eq. (4.2) does not vary with R_0 and t_p, and only the dimensional coefficient K_U changes. If, when varying R_0, we keep the values of the polar energy fluence $F_{l,0} = \int I_{l,0}(t)\,dt$ and of the ratio R_0/d_{foc} fixed, both the polar pressure impulse j_{p0} and the form-factor $\langle \bar{j}_{p\theta} \rangle$ should remain practically unchanged. Then, having noted that in Eq. (4.5) $M \propto R_0^3$ and, as it follows from Eq. (4.7), $P \propto R_0^2$, we obtain $U = K_U E_{od}^{\alpha} \propto R_0^{-1}$. Finally, because for fixed $F_{l,0}$ and R_0/d_{foc} one has $E_{od} \propto R_0^2$, we arrive at

$$K_U \propto R_0^{-1-2\alpha}. \tag{4.13}$$

Similarly, we can deduce the scaling with the pulse duration t_p by assuming that the Gaussian pulse profile is simply stretched in time by a factor a ($t_p \to a t_p$), with the peak laser intensity kept fixed. Then, because the local (polar) ablation pressure $p_a(t, 0)$ depends primarily on the local laser intensity, one can surmise that the corresponding pressure pulse will also be simply stretched in time by the same factor a. As a result, the propulsion velocity would scale as $U \to aU$. Since E_{od} in Eq. (4.2) is directly proportional to t_p, the factor K_U should scale as

$$K_U \propto t_p^{1-\alpha}. \tag{4.14}$$

Finally, rounding off the K_U and α values from Eq. (4.4), we obtain

$$K_U \approx 36 \left(\frac{25\ \mu\mathrm{m}}{R_0} \right)^{2.2} \left(\frac{t_p}{10\ \mathrm{ns}} \right)^{0.4} \mathrm{m\,s^{-1}mJ^{-\alpha}}. \tag{4.15}$$

Several dedicated RALEF simulations have confirmed that the above assumptions and relationships are obeyed with a good accuracy provided that R_0 and t_p do not deviate too far from the central values in Eq. (4.15).

Chapter 5

Laser-to-droplet alignment sensitivity relevant for laser-produced plasma sources of extreme ultraviolet light

S. A. Reijers, D. Kurilovich, F. Torretti, H. Gelderblom, and O. O. Versolato, J. Appl. Phys. **124**, 013102 (2018).[1]

We present and experimentally validate a model describing the sensitivity of the tilt angle, expansion and propulsion velocity of a tin micro-droplet irradiated by a 1 μm Nd:YAG laser pulse to its relative alignment. This sensitivity is particularly relevant in industrial plasma sources of extreme ultraviolet light for nanolithographic applications. Our model has but a single parameter: the dimensionless ratio of the laser spot size to the effective size of the droplet, which is related to the position of the plasma critical density surface. Our model enables the development of straightforward scaling arguments, in turn enabling precise control the alignment sensitivity.

[1] Dmitry Kurilovich and Sten A. Reijers contributed to this chapter as part of their PhD theses, the experimental part is provided by Dmitry Kurilovich and the modelling part by Sten A. Reijers.

5.1 Introduction

Microdroplets of liquid tin are used to create extreme ultraviolet light (EUV) for next-generation nanolithography [13, 17, 18, 42] that is currently being introduced in high-volume manufacturing. These droplets, several 10 μm in diameter, serve as mass-limited targets [23, 43] for creating a laser-produced plasma (LPP) in EUV light sources. In such machines, a prepulse laser beam hits a tin droplet to obtain an extended disk-like target [20, 21] that increases coupling with the next pulse. Subsequently, the target is irradiated by a focused nanosecond-pulse laser at intensities that lead the creation of a high-density plasma [13, 23, 44]. Line emission from electron-impact-excited highly charged tin ions in the plasma provides the EUV light peaking at 13.5 nm [13, 23]. Maximizing the conversion efficiency (CE) of laser light into the required EUV light of such sources requires a careful control over the target shape. This shape is very sensitive to the precise alignment of the prepulse laser to the initially spherical droplet [70, 94]. Any deviation from the optimum location for laser impact will produce a suboptimal target tilt and decrease the target radial expansion, as shown in Fig. 5.1. Moreover, reflections of the laser light from the incorrectly tilted surface of the target back towards the laser itself may be detrimental to laser operation stability. In spite of its obvious relevance, the precise relation between such laser-to-droplet (L2D) alignment and the resulting target tilt has so far remained poorly explored aside from activities by Tsygvintsev et al. [95] and the recent work by Hudgins et al. [70] who combine modeling with experimental efforts. Due to experimental constraints, however, their model predictions for the tilt sensitivity could not be validated under conditions of controlled misalignment.

Here, we present and experimentally validate an intuitive model describing L2D alignment sensitivity. The model is based on a single parameter: the dimensionless ratio of the laser spot size to the effective size of the droplet target, which we relate to the position of the plasma critical density surface [49, 96, 97] and sets the typical length scale for the problem. Our model enables the development of straightforward scaling arguments, which in turn enable the minimization of detrimental alignment sensitivity. We focus our studies on industrially relevant 1-μm-wavelength Nd:YAG laser pulses and experimentally validate our model predictions for two different laser spot sizes over a wide range of laser pulse energies. Furthermore, we apply the validated model to predict sensitivities for several practical cases that are immediately relevant for current state-of-the-art industrial droplet-based EUV light sources.

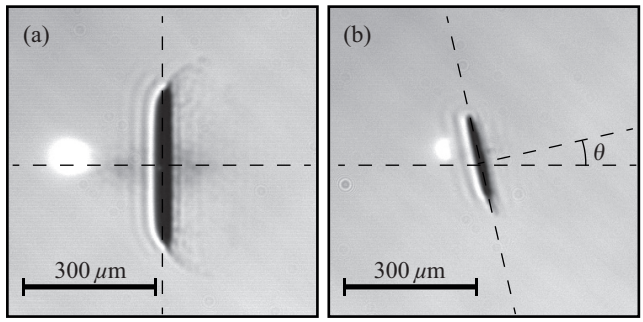

FIGURE 5.1: Side-view shadowgraphy images taken 2 μs after a 40 mJ pulse with 115 μm diameter (FWHM) spot impinged on a droplet from the left at (a) optimal alignment and at (b) a misalignment of $\Delta x \approx 100\,\mu$m leading to a tilt angle θ, accompanied by a decrease in total propulsion velocity and radial expansion. The white glow visible at the original droplet position is plasma light, where the deformed droplet has moved further downwards and sideways (see main text).

5.2 Experiment

Our experimental setup has previously been described in detail [20]. For clarity, the most important characteristics are repeated here. A droplet generator was operated in a high-vacuum chamber ($\sim 10^{-7}$ mbar) and held at constant temperature of $\sim 260°$ C. The nozzle produced a 13.4 kHz train of $\sim 43\,\mu$m diameter (radius $R_0 \approx 21.5\,\mu$m) droplets of 99.995% purity tin. The droplets were irradiated by 1064-nm wavelength, 10 ns (full-width-at-half-maximum: FWHM) long pulses of a Nd:YAG laser operated at 10 Hz repetition rate.

The laser pulse energies were varied between ~ 1 and ~ 395 mJ. The laser beam was focused down to a 115 μm or 60 μm diameter (FWHM) Gaussian spot on the droplet and was circularly polarized. While significant astigmatism was apparent for a tighter focus, the part of the beam intersecting with the droplet could still be well described by a 60 μm-diameter Gaussian function. Conversely, the 115 μm focus produced a circularly symmetric beam spot. In order to capture the dynamics of the expanding droplets two shadowgraphy systems based on 850-nm-wavelength, 15-ns pulsed laser diodes and long-distance microscopes coupled with charge-coupled-device cameras were used. The two systems provide a "front" view and a side view, 30° and 90° with respect to the laser propagation direction. By varying the time delay between the plasma-generating laser pulse and shadowgraphy pulses, a sequence of images was recorded. The images obtained from the side were processed using an image analysis program that tracks the center-of-mass displacement and the size of the expanding droplet as well as the target tilt angle. In

order to introduce controlled misalignment, the timing of the Nd:YAG laser pulse was varied around the established time for optimal alignment of laser on droplet, see Fig. 5.1. Since the droplets vertical velocity U_x stayed constant ($\sim 12\,\mathrm{m/s}$), this "mistiming" Δt resulted in a laser impact off-centered by a distance Δx, translating the initial spherical droplet into a tilted disk. The final droplet shape is the result of complex force interplay and its study is left for future work. The velocity U_x was obtained by processing the front-view images containing two or more droplets. The target tilt angle, defined as the angle between the target normal and the laser beam propagation direction (see Fig. 5.1(b)), was mapped as a function of misalignment, with $\Delta x = U_x \Delta t$, for different laser pulse energies. At the same time, we tracked the propulsion velocity u_z along the laser light propagation direction. We obtained an estimate of the droplet expansion velocity $\dot{R}$ by measuring its radius (i.e. the maximum droplet radius along the tilted axis) shortly ($1\,\mu$s) after the laser pulse impact and assuming a linear expansion on this short timescale, such that $\dot{R} \approx (R(1\,\mu\mathrm{s}) - R_0)/(1\,\mu\mathrm{s})$.

5.3 Model

In this section, we outline an intuitive model for the tilt angle θ_{tilt} (see Fig. 5.1(b)) in terms of the axial misalignment and the laser beam width. Figure 5.2 shows a schematic overview of the problem. A droplet with radius R_0 is hit by a Gaussian off-centered laser pulse having an axial offset Δx and beam width σ, which relates to the full-width at half-maximum of the laser beam according to the usual convention $\sigma = \mathrm{FWHM}/(2\sqrt{2\ln 2})$. The target tilt angle can be deduced from the direction of the target's center-of-mass motion. We derive the target's center-of-mass motion from the plasma pressure distribution on the surface of the target where the laser energy is absorbed. This pressure distribution is directly related to the spatial intensity profile of the laser. Below, we detail these steps.

During the laser impact, a small liquid layer is ablated and forms a plasma cloud on the illuminated side of the droplet, see Fig. 5.2. The time scale of this plasma generation is typically much shorter than the laser pulse. As a result, most of the laser energy is absorbed just before the plasma critical density surface [49] where the plasma electron frequency equals that of the laser light and no further light penetration is possible. This gives the system an effective radius $R_{\mathrm{eff}} \geq R_0$, see Fig. 5.2. The laser intensity profile I at R_{eff} is given by a projection of part of the Gaussian laser beam profile onto the laser-facing hemisphere with radius R_{eff} and an offset Δx. It is insightful to formulate this intensity profile in terms of two dimensionless parameters: the dimensionless laser beam width $\alpha = \sigma/R_{\mathrm{eff}}$ and the

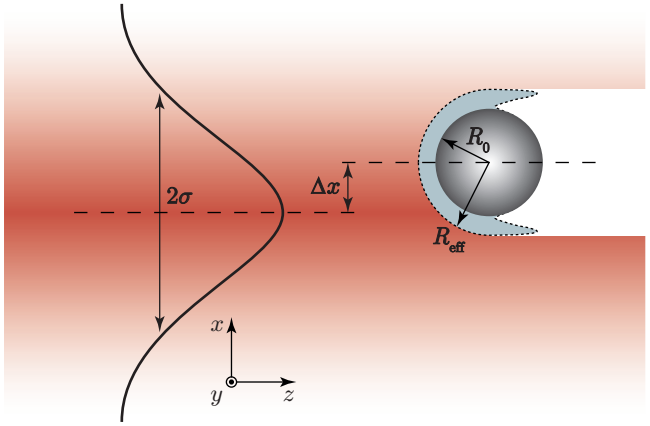

FIGURE 5.2: Schematic cross-section of the problem: a droplet with radius R_0 is hit by a Gaussian-shaped intensity-profile laser pulse with size σ from the left. The laser hits the droplet off-center with an axial offset Δx creating plasma (light gray area) surrounding the droplet on the illuminated side (dashed line), thereby creating an effective radius R_{eff}.

dimensionless laser offset $\beta = \Delta x / R_{\text{eff}}$, which gives in spherical coordinates

$$I(\theta, \phi) \sim \exp\left(- \left[\frac{\sin(\theta)^2 - 2\beta \sin(\theta)\cos(\phi) + \beta^2}{2\alpha^2} \right] \right) \times H(\pi/2 - \theta)\cos(\theta), \quad (5.1)$$

where θ and ϕ are the polar angle and azimuthal angle respectively, and H is the Heaviside step function to limit the intensity profile to the illuminated side of the droplet. Note that an extra $\cos(\theta)$ term is included in Eq. (5.1) to account for the projection of the beam onto the effective radius, which is assumed to be locally spherical and of constant size.

With the intensity profile at R_{eff} at hand, we now obtain an expression for the plasma ablation pressure p_{a} acting on this surface. A power-law dependence between this pressure and the impinging laser pulse energy has been established in previous work [20, 22, 70], and experimentally shown to be valid to excellent accuracy over three orders of magnitude in laser energy [20, 22],

$$p_{\text{a}} \propto (E - E_0)^{\delta}, \quad (5.2)$$

where $E \propto I$ is the fraction of the laser pulse energy that is intercepted by the liquid target. In the remainder of this work, we take $\delta = 0.6$ in accordance to Ref. [49]. Furthermore we neglect the small offset energy E_0, since typically $E_0 \ll E$ (see Ref. [20]) and use Eqs. (5.1) and (5.2) to find the local pressure $p_{\text{a}}(\theta, \phi)$ acting on the target's effective surface.

The center-of-mass velocity of the target is then obtained from p_a. To this end, we consider the droplet and its surrounding plasma cloud as a single body with radius R_eff that is subjected to a local pressure distribution $p_\mathrm{a}(\theta, \phi)$. Note that by doing so, we neglect the exchange of momentum between this plasma cloud and the droplet. Furthermore, we assume that the liquid body does not deform on the time scale of the pressure pulse, which is justified since the timescale of deformation is typically much longer [20, 21]. The center-of-mass velocity of the body is then given by

$$\begin{aligned} u_x(\alpha,\beta) &\sim \int_0^{\pi}\int_0^{2\pi} p_\mathrm{a}(\theta,\phi,\alpha,\beta)\sin(\theta)\sin(\theta)\cos(\phi)\,\mathrm{d}\theta\,\mathrm{d}\phi,\\ u_y(\alpha,\beta) &\sim \int_0^{\pi}\int_0^{2\pi} p_\mathrm{a}(\theta,\phi,\alpha,\beta)\sin(\theta)\sin(\theta)\sin(\phi)\,\mathrm{d}\theta\,\mathrm{d}\phi,\\ u_z(\alpha,\beta) &\sim \int_0^{\pi}\int_0^{2\pi} p_\mathrm{a}(\theta,\phi,\alpha,\beta)\sin(\theta)\cos(\theta)\,\mathrm{d}\theta\,\mathrm{d}\phi, \end{aligned} \tag{5.3}$$

where the coordinates x, y, z are defined in Fig. 5.2.

From the direction of the center-of-mass motion, one can now deduce the target tilt angle. Note that since a pressure always acts perpendicular to the surface it can never induce any rotation of the body. Therefore the target tilt is a result of the preferred expansion direction of the liquid, which by definition is perpendicular to the direction of the center-of-mass motion. As a result, the tilt angle in radians is given by

$$\theta_\mathrm{tilt}(\alpha,\beta) = \arctan(u_x(\alpha,\beta)/u_z(\alpha,\beta)), \tag{5.4}$$

which needs to be evaluated numerically. Our approach differs from the one presented in Ref. [70] as we include the full pressure distribution on the surface of the droplet, see Eqs. (5.3). Comparing the two models, our approach consistently yields significantly lower tilt angle sensitivities.

The target tilt angle sensitivity around zero misalignment is of interest for certain industrial applications [98]. To this end we define the tilt angle sensitivity around $\beta = 0$ as

$$f(\alpha) = \left.\frac{\partial\theta_\mathrm{tilt}(\alpha,\beta)}{\partial\beta}\right|_{\beta=0}, \tag{5.5}$$

which enables a straightforward inspection of the influence of the dimensionless beam width α. The tilt angle sensitivity as expressed by Eq. (5.5) can be approximated analytically by expanding Eq. (5.1) and (5.4) up to $\mathcal{O}(\beta^2)$ and results in

$$f(\alpha) = \mathrm{Re}\left(\frac{u_x(\alpha,1)}{u_z(\alpha,0)}\right). \tag{5.6}$$

The full complex expression is given in its explicit form in the Appendix. The actual tilt angle in this approximation is given by

$$\theta_{\mathrm{tilt}}(\alpha,\beta) \approx \left.\frac{\partial\theta_{\mathrm{tilt}}(\alpha,\beta)}{\partial\beta}\right|_{\beta=0}\beta. \tag{5.7}$$

Another important industrially relevant parameter is the radial expansion velocity $\dot{R}$ as a function of the misalignment. In Fig. 5.1, we observe that laser misalignment not only induces a target tilt but also significantly decreases the expansion velocity. We now employ our basic model to obtain a first-order estimate of this reduced expansion. When the laser beam is misaligned with respect to the droplet, the laser intensity absorbed by the droplet decreases. As a consequence, both the center-of-mass speed and the expansion rate of the target decrease. The partitioning of kinetic energy between propulsion (center-of-mass motion) and expansion is set by the laser beam (or pressure) profile acting on the droplet as detailed in Ref. [21]. To obtain an intuitive, first-order estimate of the target expansion velocity, we assume that this energy partitioning remains fixed and is not influenced by the misalignment or laser beam energy, such that

$$\frac{\dot{R}(\Delta x/R_0)}{\dot{R}(0)} \sim \frac{U_{\mathrm{cm}}(\Delta x/R_0)}{U_{\mathrm{cm}}(0)}. \tag{5.8}$$

Here, the left-hand-side is the expansion velocity as function of the misalignment normalized by the expansion velocity at zero misalignment, and the right-hand-side is the center-of-mass velocity as function of the misalignment normalized by the center-of-mass velocity at zero misalignment.

5.4 Results

The experimental results for the tilt angle, the z-component of the center-of-mass velocity u_z and the radial expansion velocity $\dot{R}$ are shown in Fig. 5.3 as a function of misalignment $\Delta x/R_0$. The error bars represent the standard deviation of the measurements where available, otherwise a conservative value of twice the overall average error was used. In Fig. 5.3(c) the error bars are conservatively set at 20%. We classify three different groups of experimental data. The first data set is obtained for a 115-μm focus with energies of $\sim$40 to $\sim$395 mJ (green diamonds). The second group represents the experimental data for the same focus spot size, but with laser energies between $\sim$5 and $\sim$25 mJ (red squares). The third group consists of all data having a 60-μm focus spot size with laser pulse energies between $\sim$1 and $\sim$95 mJ (blue circles). In the top panel, we observe that the tilt angle monotonically increases with the misalignment. A small but significant influence

of the laser pulse energy on the sensitivity is observed in the grouped data of the large focus spot size (green diamonds versus red squares) but this could not be further proven with any measure of significance for the individual (i.e. for single laser pulse energies) data sets. The small focus spot size (blue circles) results in a stronger tilt angle sensitivity to misalignment and show some signs of saturation at large misalignment values. In the center panel, we see that the normalized z-velocity u_z distribution has a typical bell shape, showing no significant influence of the laser pulse energy in the grouped data of the large focus spot size. The smaller spot size results in a more sharply peaked distribution. In the bottom panel, we observe that the normalized radial expansion velocity $\dot{R}$ also has a typical bell shape, which appears to be of slightly larger width than the u_z distribution. The data also shows no significant influence of the laser pulse energy in the grouped data of the large focus spot size. Again, the smaller spot size results in a more sharply peaked distribution.

To compare the experimental results in Fig. 5.3 to the model described above, we numerically evaluate Eq. (5.4) using a local adaptive solver [99]. For each experimental case we determine α based on the focal spot sizes mentioned above and the effective radius R_{eff}, which we relate to the location of the critical plasma surface. We obtain the location of the critical surface for a Nd:YAG laser pulse on tin droplets from 2D radiation-hydrodynamic simulations [49]. In that work, the distance from a tin droplet (at $R_0 = 15\,\mu$m) to the critical surface is evaluated to be $d_{\text{crit}} \approx 8\,\mu$m for a Nd:YAG laser pulse. By assuming the same position of the critical surface with respect to the droplet surface in our experimental case with slightly bigger droplets ($R_0 = 21.5\,\mu$m), we obtain $R_{\text{eff}} = R_0 + d_{\text{crit}} = 29.5\,\mu$m, and hence, $\alpha_{115} = 1.7$ (115-μm focus, green diamonds) and $\alpha_{60} = 0.86$ (60-μm, blue circles). The corresponding sensitivity curve is in excellent agreement with the experimental data (see solid lines in Fig. 5.3).

For laser energies lower than 40 mJ and a large focus spot size (red squares), the experimental data are found to be well described by the model if we set $\tilde{\alpha}_{115} = 2.3$, i.e., with the effective radius $R_{\text{eff}} \approx R_0$. This observation could be explained by

FIGURE 5.3: (Figure is found on the following page.) (a) Tilt angle of the target at various misalignments. Data for the 115-μm focus with energies below (red squares) and above (green diamonds) 40 mJ have been grouped. Blue circles represent averages of all data for the 60-μm focus case. Red, green, and blue solid lines depict numerical predictions of target tilt with $\alpha = 2.3$, 1.7 and 0.86 respectively. (b) Droplet propulsion velocity u_z in the laser beam propagation direction. The red and green solid lines fully overlap. (c) Normalized droplet expansion velocity $\dot{R}$. In (b) and (c), the velocities have been normalized to the maximum value of each data set.

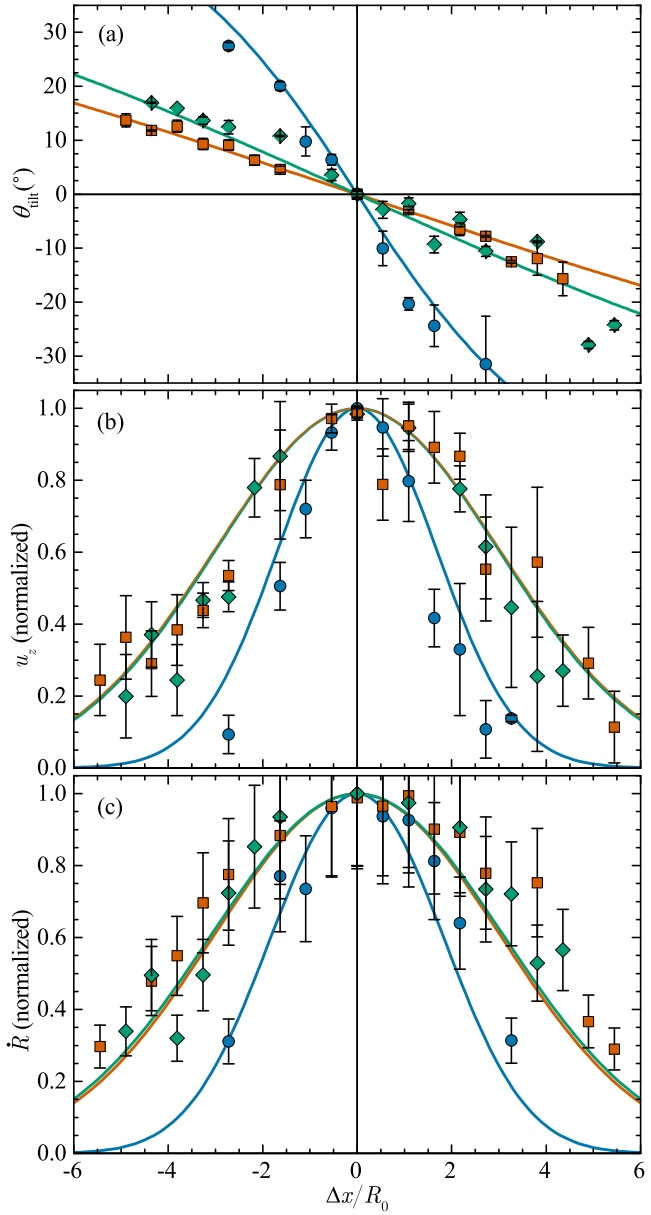

FIGURE 5.3: (Continued from the previous page.)

the reasoning that for such for low-energy and broad focus pulses the plasma is not fully developed and the critical surface is situated very close to the droplet surface ($d_{\mathrm{crit}} \approx 0$). Unfortuantely, no simulation data is available in this regime to support this claim. Furthermore, the difference between α_{115} and $\tilde{\alpha}_{115}$ could also be the result of different plasma pressure distributions [22] or additional dynamical, time-dependent effects that we do not consider here.

Using the above mentioned values for α, we observe that all theoretical curves show good agreement with the experimental data for both the tilt angle and the z-velocity u_z. Following the simple approximation given by Eq. (5.8), we compare the normalized, experimental radial expansion velocity to the theory predictions in Fig. 5.3. We find reasonable agreement between data and our model especially considering the simplifications involved and the experimental uncertainty in determining $\dot{R}$.

Next, we analyze the model prediction for the tilt angle sensitivity around zero misalignment ($\beta = 0$). Figure 5.4 shows the numerical curve (solid line) resulting from Eq. (5.5) with the dimensionless beam widths corresponding to the experimental operating conditions (see Section 5.4). The theoretical curve clearly shows that $f(\alpha)$ first increases, from unity with α peaking near $\alpha \approx 0.3$ after which a monotonic decrease is apparent. The sensitivity rises for larger droplets, keeping a constant beam width. Reversely, a smaller beam for a given effective radius will translate a large sensitivity to its alignment. In the limit $\alpha \to \infty$ one would illuminate the droplet with a flat-top beam of infinite width and would be completely insensitive to misalignment. In the limit $\alpha \to 0$ (i.e. a delta peak) the sensitivity decreases and eventually saturates to unity. In this limit the center-of-mass velocity u_x and u_z decay to zero equally fast as all energy is used to deform the droplet rather then to move its center-of-mass [21]. Hence, the ratio u_x/u_z becomes meaningless and one needs to reconsider the definition of the tilt angle. The maximum in $f(\alpha)$ is caused by a maximum in $u_x(\alpha, 1)$, see Eq. (5.6). As α gets smaller, there is initially an increase in the u_x component since pressure on the surface of the droplet is spread increasingly more onto a surface element that points in the x-direction. However, as α decreases more this surface element gets smaller too and eventually disappears completely as $\alpha \to 0$. Therefore, there is a competition between the decreasing area in this surface element and the increasing direction of the normal pointing more towards the x-direction. Hence, we find a maximum in the tilt angle sensitivity for small $\alpha \approx 0.3$. However, we note that the model is not applicable for $\alpha \ll 1$, since nonlinear plasma and fluid dynamics effects become increasingly more important when all laser energy is focused into a tight spot. In that case, the complete plasma and droplet fluid dynamics must be taken into account. In practice, for the μm-sized droplets considered here such tight focus cannot be reached and thus typically $\alpha \gg 0$.

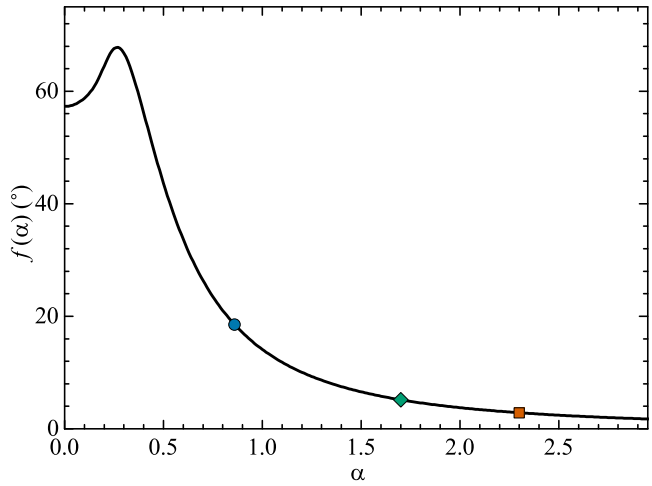

FIGURE 5.4: The theoretical tilt angle sensitivity $f(\alpha)$ (in degrees) as function of the dimensionless beam width α around zero misalignment ($\beta = 0$). The black curve is the analytically calculated tilt angle sensitivity from Eq. (5.5), with $\delta_p = 0.6$. The red square, green diamond and blue circle represent the values corresponding to the experimental conditions (see Section 5.4, color coding as in Fig. 5.3).

5.5 Discussion and industrial application

Careful control over the tilt angle sensitivity and target expansion is of crucial importance for the operating stability and CE of EUV light sources [13, 17, 18, 42]. In the following, we apply our now validated model to predict sensitivities for several practical cases that are immediately relevant for current state-of-the-art industrial droplet-based EUV light sources. In the industrial context, tilt sensitivity is typically expressed as $\theta_{\text{tilt}}/\Delta x$ (in degrees tilt / μm misalignment). Following Eq. (5.7), $\theta_{\text{tilt}}/\Delta x = f(\alpha)/R_{\text{eff}}$.

In Fig. 5.5 we present our model predictions for the sensitivity $\theta_{\text{tilt}}/\Delta x$ as function of beam width σ around zero misalignment ($\Delta x = 0$) for several values of the effective droplet size $R_{\text{eff}} = [10, 15, 25, 35, 50]$ μm. We note that by plotting for several effective droplet sizes R_{eff}, we incorporate both the droplet size R_0 and the distance from the droplet surface to the plasma critical surface d_{crit} for each case, since $R_{\text{eff}} = R_0 + d_{\text{crit}}$ (see previous section). In the figure we also show the experimental parameters studied in the previous sections, analogous to Fig. 5.4.

Figure 5.5 shows that increasing the laser spot size beyond $\sim$45 μm does not significantly change the sensitivity for the given effective droplet sizes and is therefore

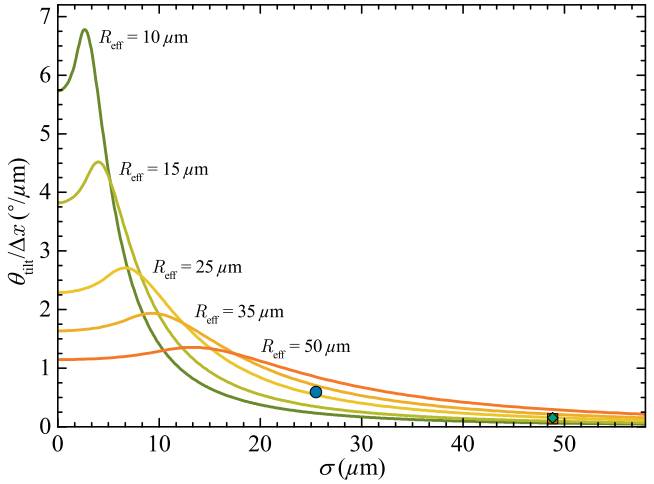

FIGURE 5.5: The calculated tilt angle sensitivity $f(\alpha)/R_{\text{eff}}$ expressed in units $^\circ/\mu$m as function of beam width σ around zero misalignment ($\beta = 0$). The curves are the analytically calculated tilt angle sensitivities from Eq. (5.5), with $\delta_p = 0.6$ and for several relevant values for the effective droplet size $R_{\text{eff}} = [10, 15, 25, 35, 50]\,\mu$m. The red square, green diamond and blue circle represent the values corresponding to the experimental conditions (see Section 5.4, color coding as in Fig. 5.3).

not useful. However, by increasing the laser spot size, the energy required to maintain a similar droplet expansion increases with $1/\sigma^2$ due to finite overlap between the droplet and the laser beam, as discussed in Ref. [20]. Therefore, in practical applications, one should find the optimum conditions balancing between a maximum expansion (i.e. minimizing σ) and a minimal tilt sensitivity (i.e. maximizing σ).

Furthermore, from Fig. 5.5 we observe that the tilt angle sensitivity increases sharply with decreasing laser focus spot size, especially when $\sigma < R_{\text{eff}}$. Under such focusing conditions, a change in the effective size of the droplet R_{eff} has a strong effect on the sensitivity. An interesting way to change the tilt sensitivity, apart from adapting the actual droplet radius R_0, is by changing the laser pulse energy or its wavelength. Shorter wavelengths or lower pulse energies result in a smaller d_{crit} and hence result in a smaller R_{eff} and vice versa.

A particularly interesting industrial application of the model is found in the use of a nanosecond-long CO_2-laser prepulse, at 10.6-μm wavelength. According to radiation-hydrodynamics simulations [49] of the interaction of such energetic laser pulses with tin droplets (at an absorbed intensity of 4×10^9 W/cm^2), the critical surface extends up to about 28 μm from the droplet surface. In the particular case

of $R_0 = 15\,\mu$m tin droplets impacted by a laser beam of $\sigma = 25\,\mu$m studied in Ref. [49], we speculate that the effective system size in our model $R_{\text{eff}} \approx 15\,\mu\text{m} + 28\,\mu\text{m} \approx 43\,\mu$m. In addition, recent experimental work using CO_2-lasers impinging on planar solid tin targets showed that the exponent in Eq. (5.2) is significantly larger, $\delta = 0.96$, compared to the case of a Nd-YAG laser [100]. These results allows us to estimate the scaling of the propulsion velocity (and thus, radial expansion velocity [21]) with CO_2-laser intensity for the $\sigma = 25\,\mu$m case. Using these values for R_{eff} and δ in Eq. (5.9), we get a sensitivity around zero misalignment of $\theta/\Delta x \approx 0.98^\circ/\mu$m, which is about 85% larger than the corresponding sensitivity for Nd:YAG $\theta/\Delta x \approx 0.53^\circ/\mu$m. For the low-energy Nd:YAG cases studied in this work, we found that our experiments were well reproduced assuming $R_{\text{eff}} \approx R_0$, which would for the current example lead to a sensitivity of $0.36^\circ/\mu$m, which differs from the CO_2 case by a factor of 2.7. Of course, the extrapolation of our model to other laser wavelengths requires further experimental validation and is left for future work.

Certain industrial applications may require a finite tilt angle [98]. Our model Eq. (5.4) offers a direct way to predict what misalignment is required to obtain a certain amount of target tilt (see also Fig. 5.3(a)). The slope of that curve around the required misalignment then gives the new tilt angle sensitivity, which can be calculated numerically by evaluating Eq. (5.5) around this new working point. We note that there are in-fact two planes in which we can induce a finite tilt angle, namely in the $x-z$ plane (as discussed in this work) but also in the $y-z$ plane. Both angles are dependent on misalignments in both x and y directions when the degeneracy is lifted by choosing a finite target tilt through a well-defined, intentional misalignment. Further study is required to see how this fact may be advantageously used to increase source operating stability by minimizing L2D sensitivity along the machine axis with the largest risk of misalignment.

5.6 Conclusions

In tin-droplet-based LPP sources of EUV light, laser-to-droplet alignment plays an important role. A slightly misaligned prepulse laser beam can lead to a non-optimal target shape, which causes an inefficient coupling with the main laser pulse and lower conversion efficiency of drive laser light into EUV. Moreover, reflections of the main pulse laser light from the tilted surface may well be detrimental to laser stability.

In this work we experimentally validated a simple, intuitive model describing the tilt angle sensitivity of a droplet impacted by a laser pulse with controlled misalignment. Our back-of-the-envelope model for the tilt angle was derived based solely on the direction of the center-of-mass velocity. From this model, we were

able to obtain the local tilt angle sensitivity around zero misalignment. We experimentally verified the tilt angle and the tilt angle sensitivity by three different experimental groups with industrially relevant settings of an Nd:YAG laser operating at its fundamental wavelength. We observed an excellent agreement with the model over a broad range of laser pulse energies and two laser focus spot sizes. Furthermore, we applied our validated model to predict sensitivities for several practical cases that are immediately relevant for current state-of-the-art industrial droplet-based EUV light sources.

Our model is a simple first-order approximation of the underlying plasma and fluid physics. Full three-dimensional simulations incorporating the complete plasma dynamics should be carried out to obtain the tilt angle as function of the full parameter space. Nonetheless, the current model already allows to physically understand the target tilt as a function of the key experimental control parameters.

Appendix

We present the full solution of the tilt angle sensitivity $f(\alpha,\delta)$ around $\beta = 0$ following (5.5) as used in Fig. 5.4,

$$f(\alpha,\delta) = 2^{-\frac{\delta}{2}-3} e^{-\frac{1}{2}i\pi\delta} \delta^{\frac{1}{2}-\frac{\delta}{2}} \left(-\frac{\delta}{\alpha^2}\right)^{\delta/2} \Gamma\left(\frac{\delta+1}{2}\right)$$
$$\times \frac{-2\delta^{\frac{\delta+3}{2}}(\delta+3)e^{\frac{1}{2}\left(\frac{1}{\alpha^2}+i\pi\right)\delta} - i2^{\frac{\delta+3}{2}}\left(\alpha^2(\delta+1)+\delta\right)\alpha^{\delta+1}\left((\delta+3)\Gamma\left(\frac{\delta+3}{2},-\frac{\delta}{2\alpha^2}\right)-2\Gamma\left(\frac{\delta+5}{2}\right)\right)}{\alpha^4\Gamma\left(\frac{\delta+5}{2}\right)\left(\delta\Gamma\left(\frac{\delta}{2}\right)-2\Gamma\left(\frac{\delta}{2}+1,-\frac{\delta}{2\alpha^2}\right)\right)}. \quad (5.9)$$

Chapter 6

Drop fragmentation by laser-pulse impact

To be submitted as: A. L. Klein, D. Kurilovich, H. Lhuissier, O. O. Versolato, D. Lohse, E. Villermaux, and H. Gelderblom. "Fragmentation of free-falling drops by laser-pulse impact."[1]

We study the fragmentation of a free-falling liquid drop that is impulsively accelerated by the impact of a laser pulse. The drop expands into a thin sheet that breaks by the radial expulsion of ligaments and the nucleation, growth, and merging of holes on the thin sheet itself. We identify two Rayleigh–Taylor mechanisms as cause of the destabilization and derive scaling laws for the characteristic time and wavenumber of destabilization for both the radial expulsion of ligaments and the hole nucleation. Combining experimental data from two liquid systems allows us to reveal how the initial laser-matter interaction affects the late-time fragmentation. The final structure of liquid ligaments is the result of an interplay between the random hole nucleation, which originates from the amplification of noise as set by the laser-matter interaction, and deterministic modulations in the local sheet thickness. The latter are a late-time consequence of the kinematics of the drop deformation and spatial variations in the laser-beam profile.

[1] Alexander L. Klein and Dmitry Kurilovich contributed to this chapter as part of their PhD theses, tin data is acquired by Dmitry Kurilovich and MEK data, model, and analysis by Alexander L. Klein.

6.1 Introduction

The impact of a laser pulse onto a free-falling liquid drop induces a large-scale deformation that eventually leads to the fragmentation of the liquid body. Figure 6.1 shows how a laser impact causes spherical drops to deform into thin, liquid sheets that subsequently break into a set of ligaments and smaller drops. Two types of breakup constitute the fragmentation process in our experiments: the radial expulsion of ligaments from a bordering rim of the sheet (Fig. 6.1 (a, c)) and the nucleation of holes on the thin sheet itself (Fig. 6.1 (b, d)). Both phenomena have been observed individually in other experimental realizations, either by the mechanical impact of a drop on a solid obstacle [101] or by the impact of a shock wave on a thin liquid film [102]. In these studies, Rayleigh–Plateau and Rayleigh–Taylor instabilities have been identified as the cause of the fragmentation. The Rayleigh–Taylor instability is driven by virtue of an acceleration at an interface between two media of different density [103]. The acceleration in our system is caused by the laser impact, localized both in time and space, and by capillary restoring forces. The latter also minimize the surface energy of the system leading to the Rayleigh–Plateau instability.

The problem in the present work deviates in two important aspects from the aforementioned studies. First, the laser impact allows to clearly separate the timescale of the drop acceleration and the subsequent fluid-dynamic response as we have seen in previous studies [20, 31]. By contrast, during the mechanical impact of a drop on a solid both deceleration and deformation take place on the same timescale. Second, the deformation of the drop into a thin sheet and the destabilization of this sheet are ultimately the result of the very same initial acceleration. This aspect sets our experiments apart from the fragmentation of a liquid film due to the impact of a shock wave. In this experiment, the film is created manually and prior to the impact.

A key application that requires understanding of drop fragmentation by laser-pulse impact is found in laser-produced plasma light sources for extreme ultraviolet (EUV) nanolithography. In these sources, a dual-pulse sequence results in the emission of EUV light from a tin plasma [13, 43, 45]: a first laser pulse shapes a liquid tin drop into a thin sheet to create a suitable target for the impact of a second, much more energetic, laser pulse that generates the plasma. Line emission from excited tin ions in the plasma provides the EUV light [13, 23]. In this process, the spatial distribution of liquid tin during the second pulse is crucial for an efficient EUV light generation. The distribution is directly affected by the fragmentation of the sheet after the first pulse. Since both the drop deformation and fragmentation have their origin in the same acceleration by the first laser impact they are coupled to each other, which renders the breakup of the liquid an intrinsic part of the laser impact on a drop. The fundamental understanding of the fragmentation is

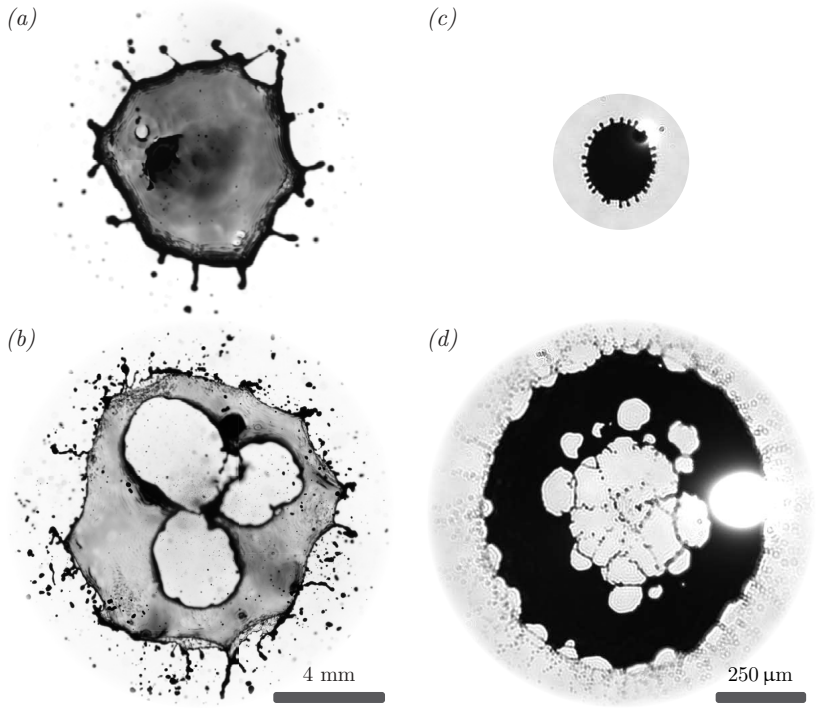

FIGURE 6.1: Fragmentation of liquid drops consisting of methyl ethyl ketone (MEK) in (a, b) and tin in (c, d) as a result of a laser impact. The drops are accelerated by the laser impact and deform into thin liquid sheets that break by the radial expulsion of ligaments as shown in (a, c) and by the nucleation and growth of holes on the thin sheet itself (b, d). The two liquid systems differ in the initial radius $R_0 = 0.9\,\mathrm{mm}$ for MEK and $R_0 = 24\,\mu\mathrm{m}$ for tin, and in the laser-matter interaction that induces the drop acceleration: the millimeter-sized MEK drops are accelerated by the local boiling of liquid and the metallic tin drops by an expanding and glowing plasma cloud, which is visible in (c, d) as white spot.

therefore of great importance to improve laser-produced EUV light sources for nanolithography.

Here, we aim to understand in detail how the initial laser impact on the spherical drop causes the fragmentation of the liquid sheet that develops as a late-time response to the very same laser impact. To this end, we study in Section 6.4 the breakup process for two different liquid systems, which each have their own unique

advantages for the study of fragmentation. On the one hand, we use millimeter-sized MEK drops (Fig. 6.1 (a, b)), which expand into semi-transparent sheets that are accessible for high-resolution and high-speed visualization of small details. On the other hand, we use micrometer-sized metal drops (Fig. 6.1 (c, d)), which experience near-perfect axisymmetric impact conditions that do not obscure our view on any fluid-dynamics instability. The details of the liquid systems and experimental setups are described in Section 6.2 and Section 6.3. Having developed a qualitative understanding of the destabilization mechanism as explained in Section 6.5, we aim to quantify the fragmentation by a description in the framework of fluid-dynamics instabilities. First, we adapt an existing model in Section 6.6 to describe the characteristic change of the liquid topology as a response to the laser impact: a spherical drop deforms into a liquid sheet that expands radially under the influence of surface tension. With a description of the kinematics at hand, we turn to the breakup at the bordering rim in Section 6.7 and the sheet breakup in Section 6.8. We will address in our analysis how the laser-matter interaction affects both the deformation of the sheet and an impulsive Rayleigh–Taylor instability. We finally present scaling laws for the characteristic time and wavenumber for both the breakup at the bordering rim and the sheet breakup.

6.2 Liquid systems

A laser-induced phase change is a way to move liquids by optical radiation and it allows for large deformations and flow speeds to be reached. The laser radiation must be strong enough to supply the energy required for the phase change, which can be a vaporization or the generation of a plasma. We make use of pulsed lasers to accelerate a free-falling liquid drop by a laser-induced phase change on a timescale that is much shorter than the subsequent fluid-dynamic response of the drop. The observed deformation of the drop upon laser impact is then determined to a large extent by the Weber number as explained in previous publications [21, 31]

$$\mathrm{We} = \frac{\rho R_0 U^2}{\gamma}, \tag{6.1}$$

where ρ is the liquid density, R_0 the initial drop radius, γ the surface tension, and U the center-of-mass velocity of the drop as a result of the laser impact. The Weber number has also been identified as an important parameter in the fragmentation of liquid films and jets [102, 104–106]. To understand now the drop fragmentation upon laser impact, we make use of two liquid systems that allow us to explore a large range in We. In this section, we introduce both system together with their characteristics that are of importance for the study of fragmentation.

In [31] we focused on the question how a laser pulse can induce fluid motion in the first liquid system under consideration here: a liquid-dye solution. We showed that the key driving mechanism for the observed acceleration is the local boiling of the drop that is induced by the absorption of laser energy in a superficial layer. The thickness δ of this layer is determined by the amount of dye dissolved in the liquid and the absorption coefficient of the dye at the laser wavelength λ_L. The laser-dye combination and the drop size can then be chosen such that only little mass of the drop is affected by the laser impact, that is $\delta/R_0 \sim 10^{-2} \ll 1$. The superficial layer δ of the drop is then ejected at the thermal speed u during the rapid vaporization on a timescale $\tau_e \sim 10\,\mu\mathrm{s}$. On the same timescale, the resulting recoil pressure p_e accelerates the remainder of the drop to the center-of-mass velocity

$$U \sim \frac{E_\mathrm{abs} - E_\mathrm{th}}{\rho\, R_0^3\, \Delta H}\, u, \tag{6.2}$$

where E_abs is the energy absorbed by the drop, E_th is the threshold energy that is needed to heat the liquid layer to the boiling point, and ΔH is the latent heat of vaporization as we explained in [31]. The scaling law (6.2) motivates our choice to use the solvent methyl ethyl ketone (MEK) for the current study: the low value of ΔH allows to induce large drop velocities for a given laser energy, which translated in view of (6.1) to a large Weber number range. An alternative liquid is an aqueous solution of Acid-Red-1, which is more convenient to handle experimentally but the range in We is limited due to the large value of ΔH for water. We characterized both liquid-dye solutions in [107]. In particular, we ensured that γ is not affected by the dye, which is crucial for the current study as capillary restoring forces affect both the drop deformation and fragmentation.

The key difference of the second system is found in the driving mechanism of the fluid dynamics: a metal drop is propelled by an expanding plasma cloud in the vicinity of the drop surface as already discussed in [20]. We briefly introduce the concept of this propulsion mechanism, since will see an important influence of the plasma cloud on the expansion rate of the deforming drop in Section 6.6. The drop is placed in the focus point of a laser beam where the local fluence exceeds the limit for plasma generation. The intrinsic extinction coefficient of the metal [61] prevents the laser light to penetrate the drop by more than a few nanometer. As soon as a plasma is generated within a fraction of the laser-pulse duration $\tau_p = 10\,\mathrm{ns}$, inverse-bremsstrahlung absorption strongly decreases the initially high reflectivity of the metallic surface to negligible values. Any further laser radiation is then absorbed by the plasma cloud that exerts a pressure p_e on the drop surface accelerating the drop as a whole. The timescale of the drop acceleration is set by the plasma dynamics, which is of the same order as the laser-pulse duration: $\tau_e \sim \tau_p = 10\,\mathrm{ns}$. Therefore, the description of the drop propulsion by a short recoil pressure p_e is analogous to the vapor-driven drop in the first system. The center-of-mass velocity U for the

TABLE 6.1: Characteristics of the two liquid systems used in the present work. MEK refers to a solution of methyl ethyl ketone and the dye Oil-Red-O enclosed in a nitrogen environment at ambient temperature (for details on the dye manufacturer see [107]). The second system consists of liquid tin at an elevated temperature in a vacuum environment (manufacturer of the liquids given in the text).

	Description	MEK	Tin
T	liquid temperature (C)	20	260
ρ	liquid density ($\mathrm{kg\,m^{-3}}$)	805	6968
ν	liquid viscosity ($\mathrm{m^2\,s^{-1}}$)	0.53×10^{-6}	0.27×10^{-6}
γ	surface tension ($\mathrm{N\,m^{-1}}$)	0.025	0.544
R_0	initial drop radius (m)	0.9×10^{-3}	24×10^{-6}
τ_c	capillary timescale (s)	5×10^{-3}	13×10^{-6}
τ_i	inertial timescale (s)	$\sim 10^{-4}$	$\sim 10^{-6}$
τ_e	propulsion timescale (s)	10×10^{-6}	10×10^{-9}
τ_p	laser duration (FWHM) (s)	5×10^{-9}	10×10^{-9}
λ_L	laser wavelength (nm)	532	1064
—	propulsion mechanism	vapor-driven	plasma-driven
We	Weber number range	90–2000	5–18500
Re	Reynolds number range	3000–14 000	400–22000
Oh	Ohnesorge number	$\ll 1$	$\ll 1$

metal drop follows a similar scaling law with respect to the absorbed energy, that is $U \sim (E_\mathrm{abs} - E_\mathrm{th})^{0.59}$, where E_abs, E_th, and the exponent now have their origin in the plasma dynamics, which we explained in [20]. We either use pure liquid tin (99.995 % purity by Goodfellow), which is motivated by the industrial application in EUV light sources, or an eutectic indium-tin alloy (50In–50Sn, 99.9 % purity by Indium Corporation) with a conveniently low melting point. Since both liquids are almost equivalent in terms of atomic mass, density, and surface tension we can use them interchangeably in the context of this work and refer to them as the tin system.

Characteristic to both systems is the clear separation of timescales: the laser-matter interaction takes place on a nanosecond timescale set by τ_p and accelerates the drop on the timescale τ_e. The drop propulsion is accompanied by a lateral expansion that occurs on the inertia timescale $\tau_i = R_0/U$ and is eventually slowed down by surface tension on the capillary timescale $\tau_c = (\rho R_0^3/\gamma)^{1/2}$. The clear separation of timescales then reads

$$\tau_e \ll \tau_i < \tau_c, \tag{6.3}$$

all of which are listed in table 6.1 for an overview on the two systems. In summary, the combination of the MEK and tin system allows us to study the fragmentation upon laser impact for a large range of Weber numbers. We neglect viscous effects as the Ohnesorge number $\mathrm{Oh} = \sqrt{\mathrm{We}}/\mathrm{Re} \ll 1$, where the Reynolds number $\mathrm{Re} = U\,R_0/\nu$ is larger than We, see table 6.1. The fragmentation then shows the same features and chronology for both systems as we will see in Section 6.4, while each setup offers advantages for our analysis. On the one hand, the millimeter-sized drops in the MEK system expand into semi-transparent sheets that are accessible for a high-resolution visualization. High-speed recordings of the fragmentation are only possible for the MEK system, since the timescale τ_c needs to be long enough to be resolved by the frame rate of the camera. On the other hand, the micrometer-sized tin drops allow to achieve much higher Weber numbers under near-perfect impact conditions that are free of azimuthal modulations in the propulsion mechanism as will be explained in the next section.

6.3 Experimental setups

We impact a free-falling drop with a carefully-timed laser pulse to propel and deform the drop into a thin sheet that finally breaks. The two liquid systems at vastly different length scale require two individual experimental setups, which are explained in more detail in [107] for MEK and water drops, and in [20] for the tin drops. Both setups rely on the same concept, which is sketched in Fig. 6.2, but differ in the details. Here, we only briefly introduce the experimental setups and comment on important differences between them.

6.3.1 Key concept of the experiment

In both setups, a drop falls down towards the laser-impact position while it relaxes to a spherical shape with radius R_0, see Fig. 6.2. On its way, the drop passes through a horizontal light sheet that generates a precise reference trigger for the main laser to impact the drop, the energy meter to acquire the laser-pulse energy E_L, and two cameras and a beam profiler for visualization. The complete arrangement of the trigger laser, photodiode, and equipment for the drop generation can be moved to align the drop in $\vec{e}_y$- and $\vec{e}_z$-direction. A delay between the reference trigger and the timing of the laser pulse allows to position the drop in $\vec{e}_x$-direction relative to the laser beam. As the drop reaches the impact position, a high-energetic pulse of light enters from the left through a focusing lens f_1, hits the drop at $x = y = z = 0\,\mathrm{m}$, and exits to the right through the imaging lens f_2.

The impact conditions for the drop can be visualized with the laser light captured by lens f_2 as will be explained in Section 6.3.4. The subsequent response of

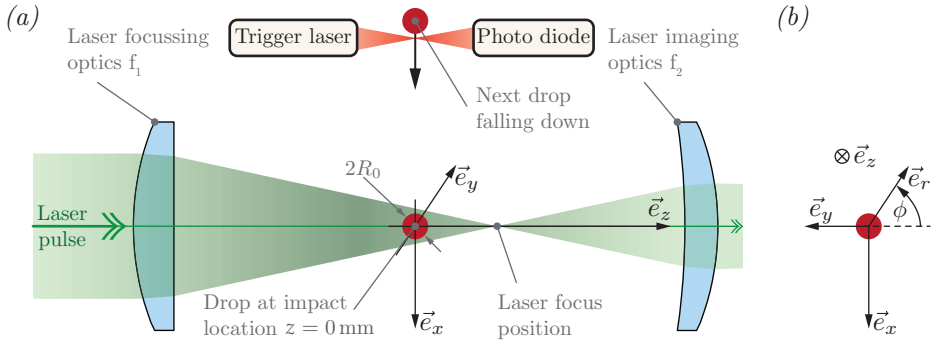

FIGURE 6.2: (a) Concept of a drop-impact experiments illustrating the moment of laser impact at $t = 0\,\mathrm{s}$ in a side-view. The laser pulse is focused by a lens with an effective focal length f_1, hits the drop, and is captured by an imaging lens f_2 to redirect the beam onto a charge-coupled device (CCD) for visualization. The drop at the impact location defines the origin of our coordinate system, which is sketched in (b) for the back-view (i.e. in $\vec{e}_z$-direction). The experiment is repeated as soon as the next drop falls down in $\vec{e}_x$-direction, which is illustrated by the drop at the top of the sketch.

the drop to the laser impact is visualized in two orthogonal views: the side-view is aligned to the $\vec{e}_y$-axis, whereas the back-view records images in the direction of the laser-beam propagation $\vec{e}_z$, see Fig. 6.2 (b). We obtain stroboscopic videos by performing a single impact experiment per video frame while changing the time delay between the laser impact and the pulsed light source that illuminates the scene of interest. Our image analysis then obtains the drop position in all three coordinate directions as a function of time, which is used to calculate the velocity U in $\vec{e}_z$-direction. The sheet radius R is determined as the equivalent radius of a circle with the same area as the shape detected in the xy-plane. Experiments that suffer considerably from a laser-to-drop misalignment or variations in the laser energy are excluded in our analysis: the velocity U is constant for $t > \tau_e$ and leads to an accurate prediction for the center-of-mass position in each video frame. We then filter typically the worst 10 % of experimental realizations to study the fragmentation process at well-defined control parameters, which is important to obtain unbiased statistics as we will see in Section 6.8. The technical equipment that is used for the MEK and tin experiments differ, as explained in the following.

6.3.2 Experimental MEK setup

Drops with an initial radius $R_0 = 0.9\,\mathrm{mm}$ are generated by the quasi-static pinch-off from a capillary tube. A filter with a pore size of 200 nm is placed at the inlet to the capillary tube to prevent solid contaminations to enter the drop that might be introduced when the dye is dissolved into the liquid. The experiment is performed in a nitrogen environment, since MEK easily forms explosive mixtures with ambient air. The excitation source is a Nd:YAG laser system at its first harmonic wavelength $\lambda_\mathrm{L} = 532\,\mathrm{nm}$ emitting pulses with a duration of $\tau_p = 5\,\mathrm{ns}$ full width at half maximum (FWHM). To improve the uniformity of the incident radiation on the drop, we use a beam-shaping and near-field imaging technique. However, for a full description of the beam preparation, drop-impact chamber, and a study on the stability of the experimental control parameters we refer the reader to [107].

To resolve all relevant time and length scales a stroboscopic imaging technique with nanosecond exposure times (High Efficiency Diffuser by LaVision pumped by a Nd:YAG laser to remove the coherence of the laser light by incoherent laser-induced fluorescence light illumination (iLIF) [108]) in combination with high-resolution cameras (pco.4000 by PCO AG and Bigeye G-1100B Cool by Allied Vision Technologies, each with $4008 \times 2672 \sim 10^7$ pixels) is used. As the drop is propelled along the $\vec{e}_z$-axis we move the back-view camera with a motorized stage to keep the deforming drop in the depth of field for each video frame. This procedure is necessary to resolve small details on the semi-transparent MEK sheets as we will see in Section 6.4. Since the fragmentation takes place on the timescale $\tau_c \approx 5\,\mathrm{ms}$ in the MEK system, we can record continuous videos of the fragmentation following typical criteria for high-speed imaging [109]. Our high-speed system consists of two continuous light sources (LS-M352A metal halide light source by SUMITA Optical Glass and a MAX-303 xenon light source by Asahi Spectra) and high-speed cameras (FASTCAM SA-X2 and SA1.1 by Photron) in a backlit configuration. We record high-speed videos at a maximum resolution of $1024 \times 1024 \sim 10^6$ pixels with a frame rate of $f_\mathrm{cam} = 10\,000$ frames per second. The advantage of the high-speed recordings in the current study is the ability to follow individual breakup events, which are not necessarily reproducible due to the stochastic nature of the fragmentation.

6.3.3 Experimental tin setup

Drops of liquid tin are dispensed from a pressure-driven drop generator with an initial radius of $R_0 = 24\,\mu\mathrm{m}$ at a temperature of $260\,^\circ C$. The laser is a Nd:YAG system emitting pulses of $\tau_p = 10\,\mathrm{ns}$ (FWHM) at the fundamental wavelength $\lambda_\mathrm{L} = 1064\,\mathrm{nm}$. Since the laser beam is focussed to generate a plasma at the drop

surface, the experiment is placed in a vacuum vessel, typically at 10^{-7} mbar, to prevent an optical breakdown before the laser pulse hits the drop. The vacuum environment also prevents an oxidization of the metallic surface of the drops.

For stroboscopic visualization of the expanding tin drops we use a shadowgraph imaging systems based on pulsed lasers and CCD cameras (Manta G-145B NIR by Allied Vision Technologies) coupled to long-distance microscopes (Infinity K2 DistaMax with CF-1/B objective and NTX tube (2x)). The back-view camera in the tin system is aligned to the $\vec{e}_z$-axis under a weak parallax angle that leads to a tilt of the image plane relative to the deforming sheets. This arrangement leads to an apparent elliptical shape of the tin sheets in the back-view images, which we correct in our image analysis when quantitative data is obtained. In early experiments, pulsed laser diodes (PLD) (about 15-ns pulse length) acted as backlight sources for illumination. In more recent experiments, the PLDs were replaced by a pulsed dye-laser pumped by the second harmonic wavelength of a Nd:YAG laser, emitting an approximately 5-ns-long pulse of 560-nm light with a spectral width of 4 nm. Such illumination enables imaging of small features of the expanding tin sheets by reducing detrimental effects due to temporal coherence such as speckle.

6.3.4 Beam profile

The interaction of the laser beam with the liquid gives rise to the pressure p_e on the drop surface that drives the fluid-dynamic response. To get detailed information on the driving force, we measure the laser beam profile with a CCD in absence of the drop before an actual impact experiment. In both systems, the imaging lens f_2 (Fig. 6.2) can be used to capture the incident radiation, i.e. the fluence $F(x, y, z = 0)$ in the impact plane spanned by $\vec{e}_x$ and $\vec{e}_y$. The CCD only records the relative fluence $f(x, y, z = 0)$ that is translated to absolute terms

$$F(x, y, z = 0) = F_0\, f(x, y, z = 0) \text{ with} \tag{6.4}$$

$$F_0 = E_\mathrm{L} \left(\int_A f(x, y, z = 0)\ \mathrm{d}A \right)^{-1}, \tag{6.5}$$

where we measure E_L with an energy meter and chose the area of integration A large enough to enclose the complete beam.

For the MEK system, the driving pressure is caused by the vapor recoil that is a direct result of the laser-matter interaction at the drop surface. As such, the pressure preserves any spatial fluctuation present in $F(x, y, z = 0)$ at the drop location. To determine the drop position and size in relation to the laser beam, we use the CCD image data during each realization of an impact experiment, see Fig. 6.3 (a). We then compute the fluence F_abs that is absorbed by the drop as

shown in Fig. 6.3 (b). The pressure p_e on the drop surface is now directly proportional to F_{abs}, from (6.2) we obtain

$$p_e(r,\phi) \sim \frac{F_{\mathrm{abs}}(r,\phi) - F_{\mathrm{th}}}{\Delta H} \frac{u}{\tau_e}. \tag{6.6}$$

Combined with the measurement in Fig. 6.3 (d) we recognize that the MEK drops are subject to a driving force that varies in azimuthal direction ϕ by about $\pm 10\%$. Since f is found to be independent of E_{L}, the azimuthal variation in the MEK experiments is then also independent of E_{L} and fixed in the Galilean reference frame of the laboratory for all our experiments.

By contrast, the tin drops experience a near-perfect axisymmetric driving force. A lens with a focal length of a $\mathrm{f}_1 = 1000\,\mathrm{mm}$ focuses the laser beam to a circular Gaussian spot, where the drop is then placed. Such an optical arrangement leads to a diffraction-limited spot diameter of approximately $100\,\mu\mathrm{m}$, which can be estimated by the extent ω_0 of an Airy disk [110] that scales as $\omega_0 \sim \lambda_{\mathrm{L}}\,\mathrm{f}_1/d_0$ with d_0 as the laser-beam diameter before lens f_1. However, this optical arrangement dictates a length scale of a few micrometer for the tin system, that is $R_0 = 24\,\mu\mathrm{m} < \lambda_{\mathrm{L}}\,\mathrm{f}_1/d_0$. The advantage of the focussing condition is a homogenous laser radiation at the impact location, see Fig. 6.3 (e, f). In addition to the homogenous laser radiation, any spatial fluctuation comparable to R_0 is removed by the intermediate step of the plasma generation during the drop acceleration: the tin drop is not subject to the direct laser radiation but shielded by its own plasma cloud as explained in Section 6.2. As a consequence, the fluid dynamics obey a high degree of rotational symmetry as we will see in Section 6.4.

FIGURE 6.3: (Figure is found on the following page.) (a) Planar laser-beam profile in the MEK system as recorded in the absence of the drop for $y/R_0 \leq 0$ and recorded during an experiment with the drop for $y/R_0 \geq 0$. The latter yields the drop radius R_0 and position in the beam profile as indicated by the solid red line (b) Energy per unit area absorbed by the drop, that is the fluence F_{abs} taking losses due to Fresnel reflection [110] at the liquid-air interface into account. Based on approximately 100 recordings of such a spatial distribution a mean profile (connected red dots) in radial (c) and azimuthal direction (d) is determined. The solid black line represents the predicted result for a perfect flat-top beam profile (indicated by $F_{\mathrm{abs,FT}}$ in (d)) (e) Planar laser-beam profile measured for the tin system and the drop marked in the center (red circle) at its expected position. The same colorbar as in (a) is used but the profile exhibits less spatial variations at the drop position, which explains the absence of yellow hotspots in the image. (f) The Gaussian beam profile in radial direction r recovered from (e).

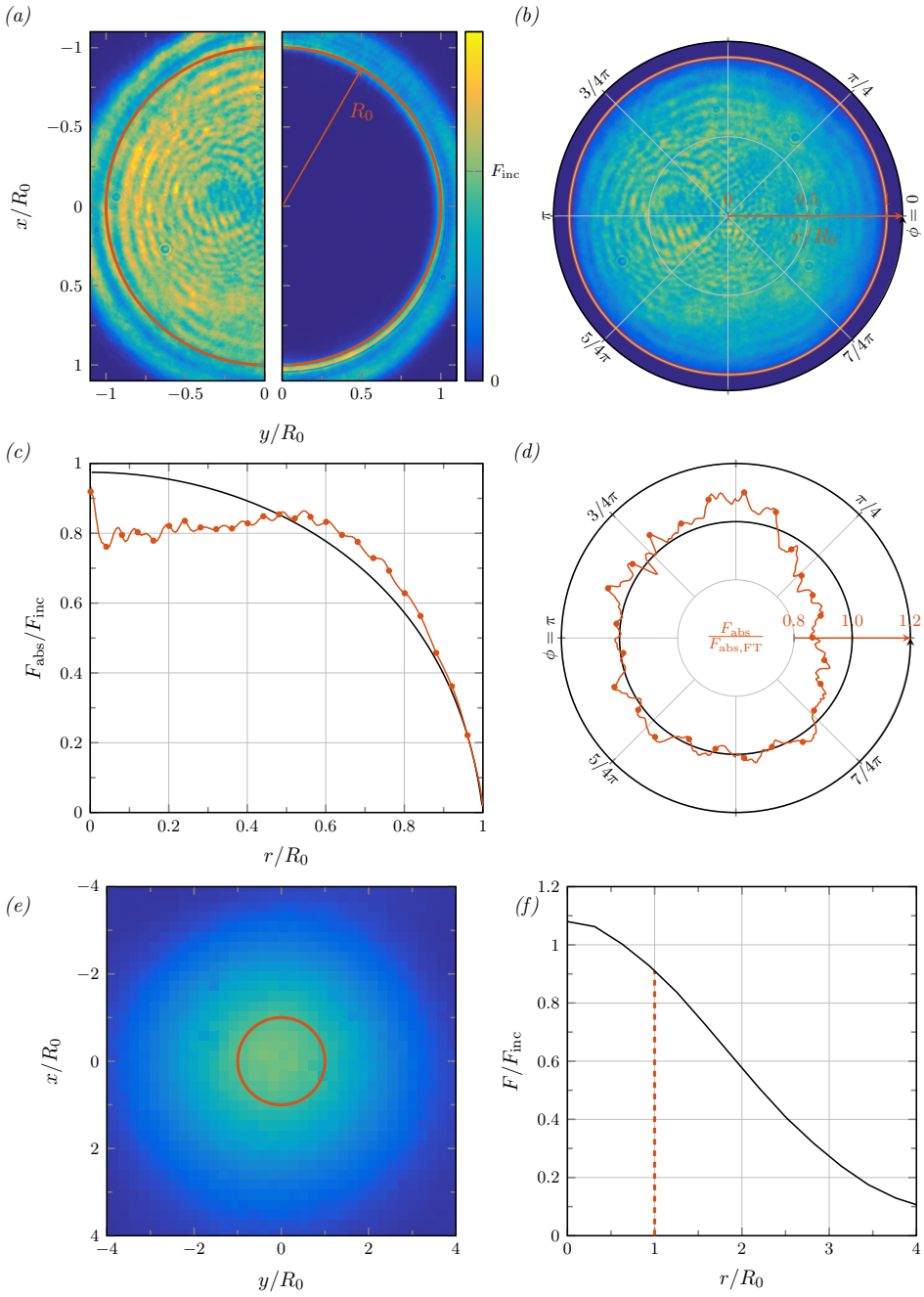

FIGURE 6.3: Continued from the previous page.

6.4 Chronology

The MEK experiment in Fig. 6.4 illustrates the chronology of the drop fragmentation, which starts with the laser impact and ends with a structure of ligaments that subsequently break into smaller drops. First, the drop accelerates on the timescale $\tau_e \sim 10\,\mu s$ and starts to move forward in $\vec{e}_z$-direction at the velocity U while it expands in radial direction r. At $t = 0.27\,ms$ the drop already resembles a thin sheet. This time corresponds to the inertia timescale $\tau_i = R_0/U = \tau_c\,We^{-1/2} = 0.28\,ms$ of that particular experiment. The liquid is semi-transparent in our visualization, which allows us to observe a thinner outer region of the sheet that is bordered by a thicker and hence darker rim. Likewise, the center of the sheet is still thick compared to the outer region. As the sheet radius $R(t)$ further expands with time the sheet thickness decreases as shown by the growing gray areas on the sheets at $t = 0.54$ to $1.7\,ms$. The variation of gray values on the sheet in Fig. 6.4 shows that the sheet thickness is a function of time and space, that is $h(r,t)$. We notice modulations of the sheet thickness in azimuthal direction ϕ, but the sheet in the back-view images preserves a near-circular shape during the expansion, i.e. an axisymmetric evolution about $\vec{e}_z$.

The fragmentation of the drop is observed as a continuous evolution that accompanies the deformation of the drop into a thin sheet and the radial expansion of the sheet thereafter. Two types of breakup can be identified in Fig. 6.4. First, the breakup of the bordering rim: corrugations are visible on the rim at $t = 0.27\,ms$, but they are still small in relation to the sheet radius R. The corrugations grow over time until ligaments are expelled radially outward, which is visible for the first time in Fig. 6.4 at $t = 0.54\,ms$ ($t/\tau_c = 0.1$). The ligaments break to from stable drops that continue to move radially outward at a constant speed, which is comparable to $\dot{R}$ at the moment of detachment from the sheet. As a result, the sheet at $t = 1.1\,ms$ in Fig. 6.4 is surrounded by a cloud of tiny drops.

The breakup of the thin sheet is the second type of destabilization in our experiments and follows the same principle as observed for the rim: corrugations appear on the liquid body that eventually result in a change of the topology with the liquid mass collected in elongated ligaments. Then, the ligaments break to form stable drops. Only now, the fragmentation is not localized to an one-dimensional structure as for the rim but takes place on the two-dimensional sheet. Corrugations are visible on the sheet at $t = 1.1\,ms$ in Fig. 6.4, where a pointer at the top highlights a patch with large spatial frequency components. We observe such disturbances on the sheet to precede any hole nucleation, including multiple holes piercing a single patch of corrugations. Figure 6.4 shows two cases where a single hole nucleates in a corrugated region: at 1.1 ms the lower pointer marks a hole shortly after it pierced the sheet close to the outer rim and at 1.7 ms the same process is captured in the center of the sheet. Once a hole nucleates on the sheet it continues to grow,

thereby collecting the surrounding liquid mass of the sheet in a rim. The last frame at $t = 2.5\,\mathrm{ms}$ in Fig. 6.4 shows the result of multiple holes growing and eventually merging over time: the liquid of the sheet is finally collected in a two-dimensional structure of ligaments that breaks into stable drops.

A comparison of the MEK and tin system in terms of the drop deformation and fragmentation is shown in Fig. 6.5. The first row shows the destabilization of the bordering rim for an otherwise intact sheet at low Weber number. The rim cannot be observed directly for the tin sheets, since they appear opaque in the visualization due to the large extinction coefficient of visible light in tin [61]. Both systems show the formation of ligaments and the detachment of tiny drops once these ligaments break. We refer to this fragmentation mechanism as *rim breakup*. The second and third row of Fig. 6.5 show how the sheets break by the nucleation of holes at two distinct regions: either close to the rim or in the center of the sheets. The thinner neck region at $r/R \sim 1$ seems to promote the breakup by hole nucleation, which we refer to as *neck breakup*. We observe a second location for hole nucleation at $r/R < 0.5$, referred to as *center breakup*.

The neck breakup is observed before the center breakup and may repeat itself several times during the sheet expansion. Holes pierce the sheet in the neck region and continue to grow.Once the holes have reached the outer rim of the sheet, the rim is basically detached from the sheet and breaks up in tiny drops (see Fig. 6.5 (b) and (e)). The liquid mass collected by the holes during their growth forms a new and corrugated rim. The observation of the neck breakup requires a high spatial and temporal resolution. The process is localized in space to a region close to $r/R \sim 1$ and leaves no other trace behind than a corrugated rim and tiny drops. The detached drops contribute to the cloud of drops surrounding the sheet that we already observed for the rim breakup. For example, Fig. 6.1 (c) is shown as an example for the center breakup but the neck breakup already took place (which is why the image is taken at a later time t and the sheet appears larger than the one from the same experiment in (b)).By contrast, the growth of holes during the center breakup is much easier to observe experimentally, which is why we will base our quantitative analysis in Section 6.8 mostly on data obtained for the center breakup.

The opaque tin sheets prevent a further comparison of the two systems in terms of the corrugations that are visible for MEK in Fig. 6.5 (b, c). However, both systems show identical, qualitative features for the fragmentation. A difference between the two systems is found in the Weber number at which fragmentation is observed. While the rim breakup is observed for both systems at a comparable Weber number (compare Fig. 6.5 (a) and (d)), more than one order of magnitude in We separates the two systems during the sheet breakup in Fig. 6.5 (b, c) and (e, f). We will see in Section 6.8 that this difference is caused by the different driving mechanisms that affect the sheet destabilization.

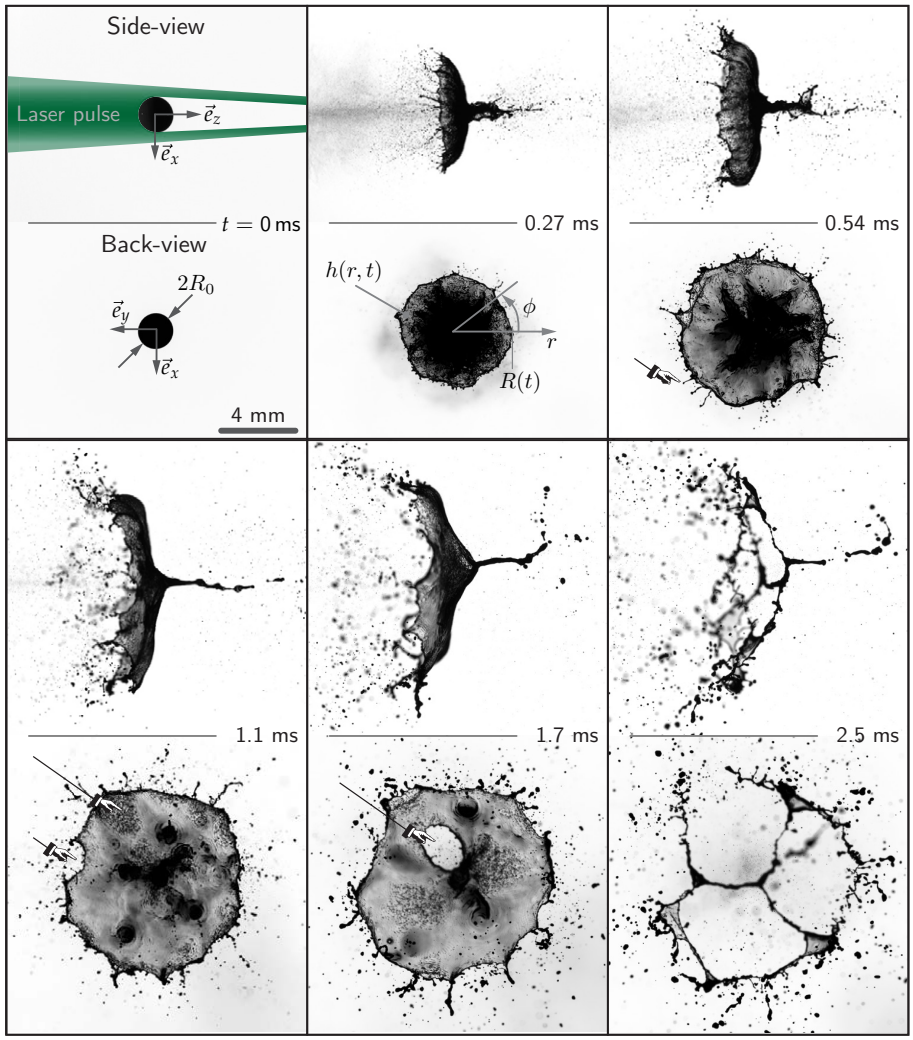

FIGURE 6.4: Sequence of events following the impact of laser pulse on free-falling drops in the MEK system at We = 330 ($\tau_c = 5$ ms). Images are recorded in stroboscopic fashion in a side- and back-view, where the side-view images are shown in a comoving frame with the propulsion speed U subtracted.At the inertial timescale $\tau_i = \tau_c \,\mathrm{We}^{-1/2} = 0.27$ ms, the semi-transparent liquid allows to recognize a thin sheet of radius $R(t)$ and non-uniform thickness $h(r,t)$ that is bordered by a rim. The pointers in the subsequent three pictures mark the onset of fragmentation during the sheet expansion: radial expulsion of ligaments at $t = 0.54$ ms, corrugated areas and a hole piercing the sheet close to the rim a $t = 1.1$ ms, and hole nucleation close the center of the sheet at $t = 1.7$ ms. A final web of ligaments is shown for $t = 2.5$ ms.

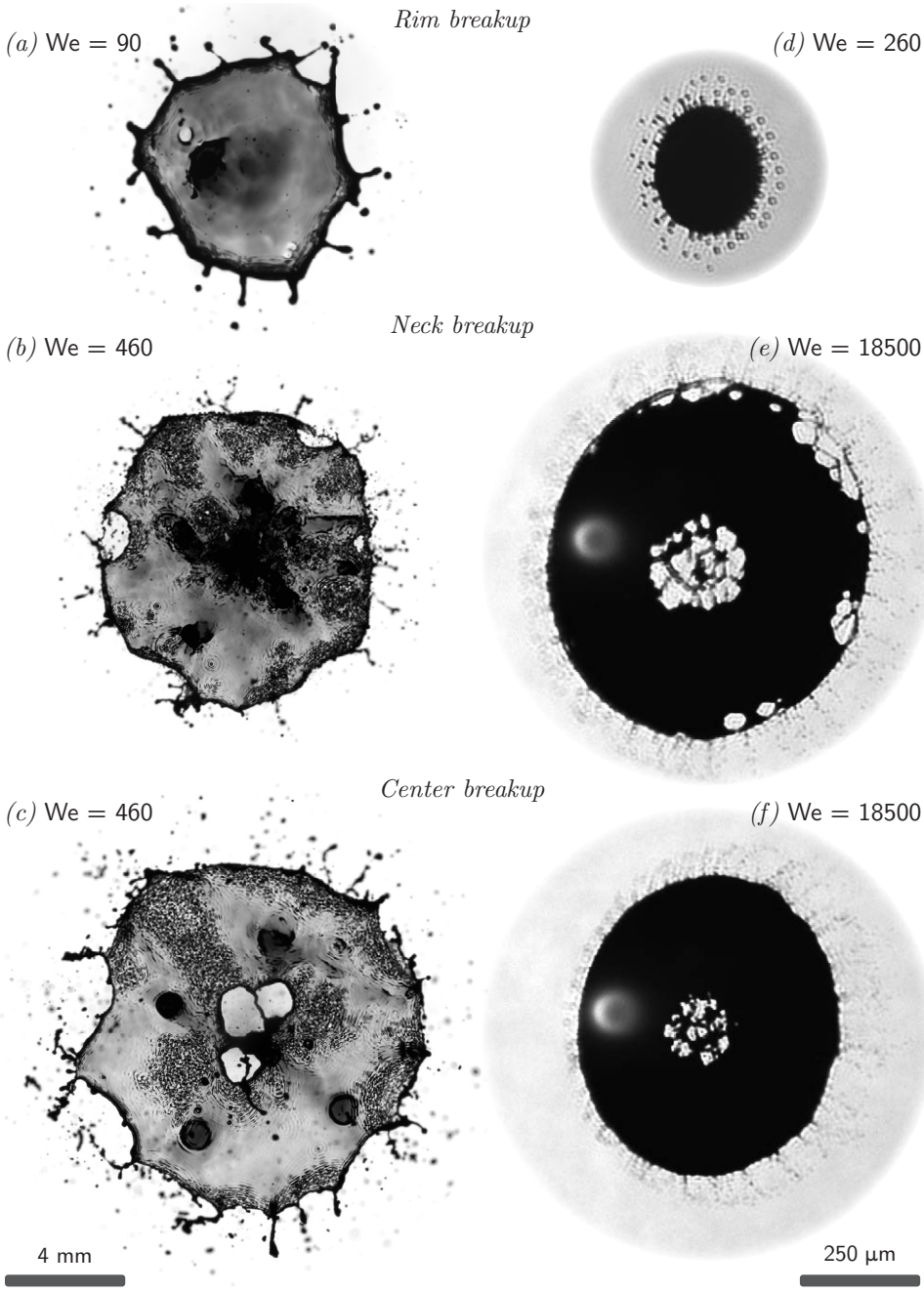

FIGURE 6.5: (Continued on the following page.)

FIGURE 6.5: (Figure is found on the previous page.) Fragmentation regimes for vapor-driven MEK drops (a–c, $R_0 = 0.9\,\mathrm{mm}$) and plasma-driven tin drops (d–f, $R_0 = 24\,\mu\mathrm{m}$). In both systems, the fragmentation of the sheets starts at three distinct locations: the bordering rim (first row: (a, d)) and the breakup at the neck (second row: (b, e)) and center of the sheet (third row: (c, f)). The apparent elliptical shape of the tin sheets is caused by a weak parallax angle of the camera relative to the propulsion in $\vec{e}_z$-direction. The white spot in figure (b) and (c) is an artifact of the plasma that propels the tin drop. Both MEK and tin drops show the same features during the fragmentation, which we refer to as *rim*, *neck*, and *center breakup* (see text).

6.4.1 Some comments on jetting

In addition to the sheet evolution, one observes the ejection of mass on the opposite site of the laser impact in form of a liquid crown (notice the thin and hence gray areas at the tip, visible at $t = 0.27\,\mathrm{ms}$ in Fig. 6.4). The ejected mass moves at a speed larger than U, collapses on the $\vec{e}_z$-axis ($t = 0.54\,\mathrm{ms}$), and forms a jet that detaches from the sheet and finally breaks up ($t = 1.1$ to $2.5\,\mathrm{ms}$). The jetting, or in general the ablation of mass, is also observed in the tin system as shown in Fig. 6.6 (a, b). However, the effect of this early jetting on the sheet evolution is observed to be small as the ejected mass is small compared to the remainder of the drop. A description of the phenomena is therefore beyond the scope of the present study, while we recognize that it may results in a slightly tampered center region of the sheet when it becomes sufficiently thin as illustrated in Fig. 6.6 (d). Here, we briefly comment on the physical cause that may lead to the jetting phenomena.

The early jetting is not a direct consequence of the pressure pulse driving the expansion: detailed simulations of the drop-shape evolution by a boundary-integral (BI) method, which is capable to reproduce jetting phenomena in principle [111], do not show this feature as we saw in [21], compare also Fig. 6.6 (c). A possible explanation for the jetting is the occurrence of a cavitation bubble that could give rise to a fast jetting phenomena [112–115]. However, a nucleation of a bubble inside the drop by direct laser radiation is unlikely in our systems. The penetration depth of the laser light for both MEK and tin is limited to fraction of the drop, that is $\delta/R_0 \ll 1$ as already explained in Section 6.2. Acoustical effects could however induce a cavitation bubble [115, 116]: pressure transients induced on one side of the drop travel to the opposite side or may even be focus inside the drop. Thermoelastic pressure waves are caused by the rapid heating of the superficial layer of the MEK drops under isochoric conditions[2] [117–119]. The same effect leads to

[2]Thermoelastic pressure transients under isochroic conditions [117] are achieved in the MEK system since $c\,\tau_p/\delta \sim 1$, where c is the speed of sound in the liquid, δ the layer thickness heated by the laser and τ_p the laser-pulse duration.

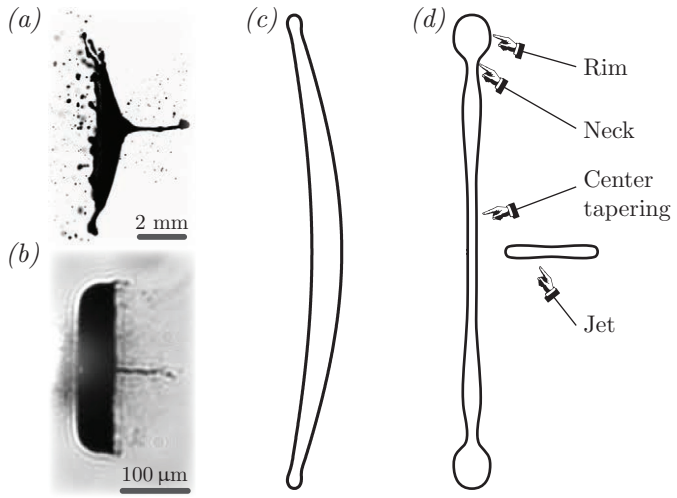

FIGURE 6.6: (a, b) Side-view images showing the formation of a jet in the center of the drop in the MEK (a) and tin system (c). (c) Sheet contour obtained from a BI simulation illustrating the cross section of the axisymmetric shape for We = 790 (taken from [21]). (d) Sketch of the sheet showing a bordering rim and a tampered neck and center region.

pressure transients in tin drops [54], where in addition the plasma generation is accompanied by shock waves [120, 121]. We recognize that the compressibility of the liquid and acoustic effects may cause the jetting phenomena. However, the inclusion of these effects in our study on fragmentation is out of scope given the small effect of the jetting on the overall system response, especially the late-time sheet dynamics.

6.5 Interpretation

The laser impact on a free-falling liquid drop can be understood as a rapid acceleration on the timescale τ_e that acts on the spherical surface of the drop and causes the subsequent deformation into a thin sheet bordered by a rim. The destabilization of this liquid body is then observed on the timescale τ_i and τ_c as a continuous evolution: corrugations appear and eventually lead to a change of topology such that the liquid mass is collected in elongated ligaments. Then, the ligaments break to form stable drops. This fragmentation process was observed in Section 6.4 in two different configurations: the breakup of the bordering rim, which we referred to as *rim breakup*, and the hole nucleation on the sheet itself called the *sheet breakup*.

The latter was observed at two different locations on the sheet, which we denoted by *neck* and *center* breakup. We now evaluate what the mechanisms are that can possibly cause and amplify corrugations on the deforming liquid drops in our experiments. As we will demonstrate below, the accelerations by the laser impact and capillary restoring forces each induce fluid-dynamic instabilities that lead to the breakup.

The kinematics of the sheet in our experiments are in striking agreement with the impact of a drop on pillar [101]. Also there, the topology of a drop is rapidly changed to an expanding thin sheet that is bordered by a rim. Not surprisingly, we observe the same destabilization and breakup for the rim as described by [101]. The rim diameter was found to reach an equilibrium value such that the rim is affected by a Rayleigh–Plateau instability, similar to the breakup of an elongated liquid cylinder of constant diameter. In addition, the liquid in the rim is subject to an acceleration that is determined by the expansion and recoil dynamics of the sheet leading to a Rayleigh–Taylor mechanism. Our observations for the nucleation, growth, and merging of holes on a sheet are in agreement with a previous study by [102]. In their experiment, a thin liquid film is accelerated by the reflection of a traveling shockwave at the liquid film itself. The hole nucleation is explained with an impulsive Rayleigh–Taylor instability driven by the strong accelerations perpendicular to the sheet. By contrast, the sheets in our experiments are not subject to a direct acceleration. A possibly candidate in our experiments for a strong acceleration is the initial acceleration of the drop, i.e. an acceleration at a time when the thin sheet has not yet developed. Our analysis then needs to address when both the evolving liquid sheet and a simultaneous Rayleigh–Taylor instability are in such a state for breakup to occur.

Having identified Rayleigh–Plateau and Rayleigh–Taylor instabilities as likely candidate for the destabilization of the liquid sheet, we realize that both the rim and the sheet breakup depend on the sheet kinematics: the radius $R(t)$ determines the acceleration during the rim breakup and the thickness $h(r,t)$ is required to follow the evolution of an instability during the sheet breakup. Consequently, we first seek an analytical description in terms of $R(t)$ and $h(r,t)$ for the deformation and expansion of the drop in Section 6.6. With a description of the kinematics at hand, we then turn to the analysis of the breakup itself: in Section 6.7 we study the rim breakup and in Section 6.8 the breakup of the sheet.

6.6 Expansion dynamics

As discussed in [21], the deformation of a drop by virtue of a laser impact can be described in three stages: an early-time stage ($0 \leq t \leq \tau_e$) where the spherical drop is accelerated and gains kinetic energy as a result of a recoil pressure p_e acting

on its surface. Then follows an intermediate stage ($\tau_e < t \lesssim \tau_i$) where the drop deforms into a sheet, and a late-time stage ($t \gg \tau_i$) where the sheet undergoes a surface-tension limited expansion. In the early-time analytical model the partition of kinetic energy of translation and deformation $E_{\mathrm{k,d}}/E_{\mathrm{k,cm}}$ is obtained from the recoil pressure p_e, which is set by the laser-matter interaction recalling for example expression (6.6). This energy partition is then fed into a late-time model that describes the expansion dynamics in terms of a rescaled Weber number based on the kinetic energy of deformation

$$\mathrm{We_d} = \frac{E_{\mathrm{k,d}}}{E_{\mathrm{k,cm}}}\,\mathrm{We}. \tag{6.7}$$

In [21] we used a simple late-time model assuming a sheet of uniform thickness. However, in our MEK data we observe a clear radial dependency of the sheet thickness and need to apply a slightly more sophisticated sheet model to accurately describe our expansion data. To this end, we use a model that was previously used to describe the sheet evolution after the drop impact on a pillar [101]. This model described the sheet dynamics away from the pillar region and includes a spatial dependency in the description of the sheet thickness $h(r,t) \sim 1/r$, which has been validated experimentally by [122]. In this model too, it is assumed that the drop impact itself is decoupled from the subsequent dynamics of the sheet, an assumption that is well justified for our systems in view of the separation of timescales (6.3). Following [101], we describe the sheet radius $R(t)$ as

$$\frac{R(t)-R_0}{R_0} = \sqrt{3\,\mathrm{We_d}}\,\frac{t}{\tau_c}\left(1-\frac{\sqrt{3}}{2}\frac{t}{\tau_c}\right)^2. \tag{6.8}$$

The only modification introduced is the rescaling of We in analogy to the approach described in [21]. We choose the rescaling such that the energy partition of the thin sheet at $t = \tau_i$, i.e. when the topology of the drop changed to a thin sheet, matches the analytical result from the early-time model, see appendix Section 6.9 for the details.

The energy partition allows to incorporate different laser-matter interactions that set the recoil pressure p_e on the liquid interface during the drop acceleration. Since the relative fluence $f(x,y,z=0)$ in the impact plane is kept constant for all MEK experiments and is directly related to the pressure p_e as explained in §6.3, the energy partition is independent of E_{L} and can be calculated analytically to $E_{\mathrm{k,d}}/E_{\mathrm{k,cm}} = 1.8$, which we already used in [21]. In this calculation, we neglect the threshold fluence F_{th} in expression (6.6) as we operate the experimental setup at $F_{\mathrm{abs}} \gg F_{\mathrm{th}}$, which is necessary to reach large Weber numbers. By contrast, the energy partition for the tin drops is a function of E_{L}, since the plasma dynamics is a function of the incident laser energy, even at constant focusing conditions. We

find $E_{\mathrm{k,d}}/E_{\mathrm{k,cm}}$ to follow a power law with respect to E_{L}, see Fig. 6.7. A theoretical prediction of the scaling law requires a profound understanding of the plasma dynamics during the laser impact and goes beyond the scope of this study. However, the trend with the laser energy can be explained: a comparison of Fig. [s]6.7 (b–d) shows that at lower laser energy the plasma cloud covers a smaller area of the drop surface, which results in an effective focusing of the recoil pressure to a confined region. The more focused a pressure distribution is, the more kinetic energy goes into deforming the drop without translating it as we saw in [21]. This relation then translates to an increase in $E_{\mathrm{k,d}}/E_{\mathrm{k,cm}}$ as the laser energy E_{L} decreases, which is in agreement with our experimental observations.

The comparison of the analytical expression (6.8) to experimental data for both MEK and tin experiments is shown in Fig. 6.8 (a) and (b), respectively. The initial expansion to the maximum radius $R_{\max}$, the moment when $R_{\max}$ is reached at $t_{\max} = 2\,\tau_c/\sqrt{27} \approx 0.38\,\tau_c$, and the recoil of the sheet due to surface-tension forces are accurately captured by the model. Especially for tin the agreement between model and experiment holds over nearly four decades in Weber number (Fig. 6.8 (b)). The model deviates from the experimental results only for cases where the fragmentation severely affects the topology of the sheet. The onset of the sheet breakup is earlier for MEK in comparison to tin as we will see in Section 6.8. Consequently, we observe the model here to deviate earlier in Fig. 6.8 (a) for MEK when compared to tin in (b), especially for large Weber numbers that lead to a severe neck breakup as explained in the following.

In the collapsed view of Fig. 6.8 (c) a few cases are highlighted to illustrate how fragmentation affects the comparison between model and experiment. A reference case in absence of any fragmentation is given by $\mathrm{We} = 5$ that follows the model perfectly. Second, for tin at $\mathrm{We} = 130$ the sheet itself is stable and we only observe the rim breakup, which leads to an apparent over-expansion of the sheet radius in the experiment for $t > t_{\max}$. In the corresponding inset in Fig. 6.8 (c) we see how ligaments are expelled radially outward and do not follow the recoil of the sheet for $t > t_{\max}$. Our image analysis excludes detached ligaments and tiny drops in the calculation of R, but ligaments that are connected to the sheet still cause the apparent over-expansion. The same behavior is observed for MEK at $\mathrm{We} = 90$ in Fig. 6.8 (a). Interestingly, the effect of the rim breakup on the sheet dynamics decreases with increasing Weber number: for $\mathrm{We} = 960$ the model follows the experimental data points perfectly during the recoil phase (Fig. 6.8 (b)), although the rim breakup is observed in the experiment. Indeed, the sheet model (6.8) predicts the rim diameter b and hence the mass contained by the rim to decrease with Weber number as $b/R_0 \sim \mathrm{We_d}^{-1/4}$ [101]. However, with increasing Weber number the sheet fragmentation leads to a deviation between model and experiment, which is illustrated for $\mathrm{We} = 330$ in Fig. 6.8 (c). Holes nucleate in the

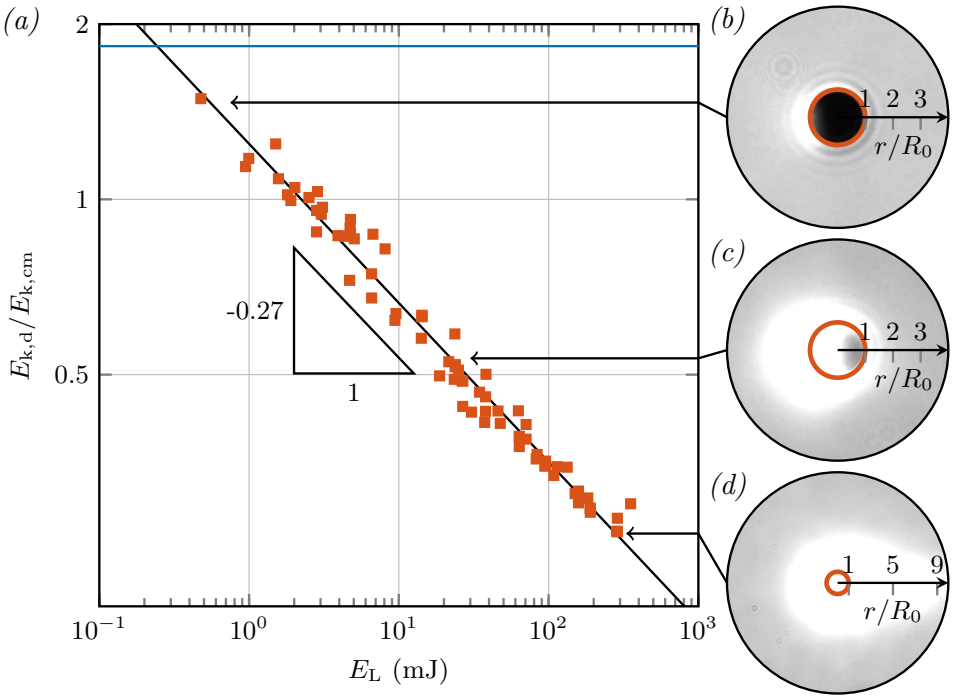

FIGURE 6.7: Energy partition $E_{k,d}/E_{k,cm}$ as function of laser energy E_L for MEK (solid blue line) and tin drops (red squares) in (a). The values for MEK are calculated analytically to $E_{k,d}/E_{k,cm} = 1.8$, independent of E_L(see text). The values for tin (red squares) are determined for each experiment by the best fit of expression (6.8) to the experimental curves shown in Fig. 6.8. The solid black line is then the power law that follows from a linear regression yielding $E_{k,d}/E_{k,cm} = 0.19\,(E_L/E_0)^{-0.27}$ with $E_0 = 1$ J. The three insets (b–d) visualize the white plasma clouds that result in the deformation of the tin drops. The initial undeformed tin drops are marked by the red circle in each inset.

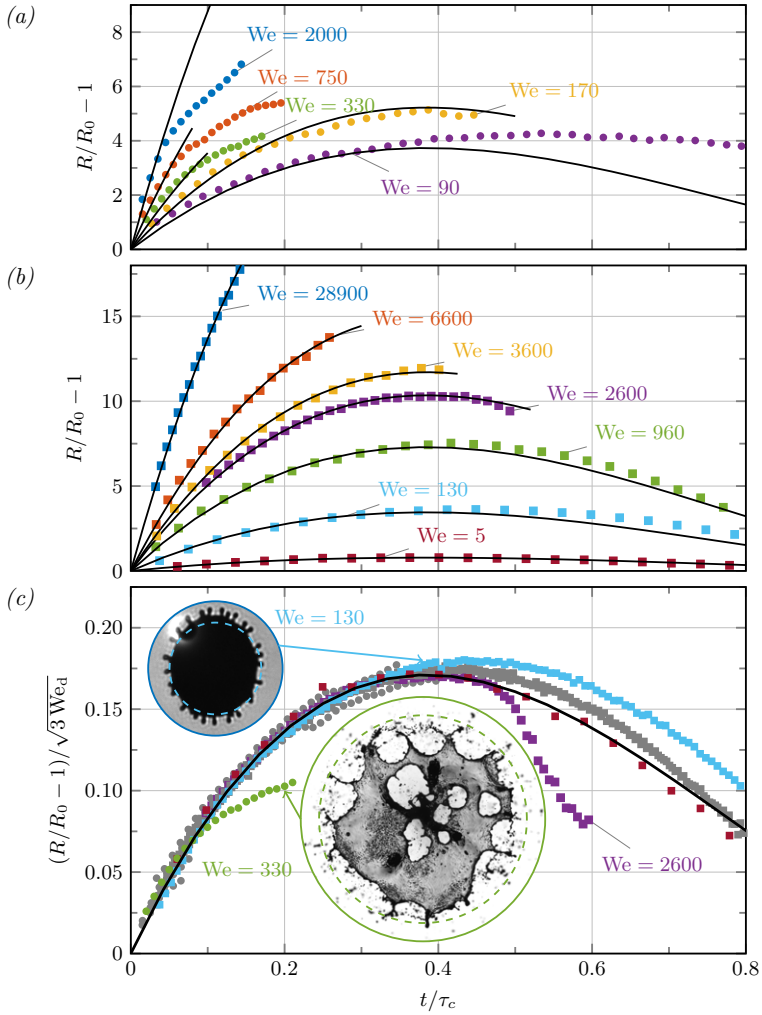

FIGURE 6.8: Sheet-radius evolution as function of dimensionless time t/τ_c for MEK ((a), circle markers in (c)) and tin drops ((b), square markers in (c)). The solid black line is the trajectory expected from (6.8). Experimental curves are shown with a reduced marker density in (a, b) for better visualization. (c) Rescaled experimental data comparing all experiments of (a) (gray circles) and (b) (gray squares) to the analytical prediction (6.8). Experimental curves are stopped in case the sheet evolution is strongly affected by the fragmentation, which is shown in the two insets for the rim breakup (tin drop at We = 130) and sheet breakup (MEK drop at We = 330).

neck region of the MEK sheet at $t/\tau_c < 0.2$ and start to grow. Our image analysis is able to deal with holes on the sheet that have not yet reached the outer rim, such that the calculation of R is not affected. However, as holes reach the outer rim and cause the rim to partially detach from the sheet as shown in the inset, the experimentally determined radius R decreases rapidly. The rapid decrease in R due to the neck breakup is also visible for tin sheets, e.g. for We = 2600 in Fig. 6.8 (c) at $t/\tau_c > 0.5$. Since the sheet breakup is observed for tin later in time as compared to MEK, this deviation sets in later as well for tin.

The model (6.8) includes a sheet thickness description $h(r,t)$ that applies in a region away from the drop center and reads in terms of this thesis [101]

$$h(r,t) \sim \frac{R_0^2\,\tau_c}{\sqrt{\mathrm{We_d}}rt}. \tag{6.9}$$

Four our discussion on the sheet breakup later in Section 6.8 we need a description of the center region where we cannot employ (6.9). We therefore describe the late-time dynamics of the sheet thickness in a mass-averaged sense as

$$\frac{h}{R_0} \sim \left(\frac{R}{R_0}\right)^{-2}, \text{ with} \tag{6.10}$$

$$\frac{R}{R_0} \sim \frac{R_{\max}}{R_0}\,\frac{t}{\tau_c} \sim \mathrm{We_d}^{1/2}\left(\frac{t}{\tau_c}\right)^{1/2}, \tag{6.11}$$

where we made use in the latter expression of the linear radial expansion, which is valid for $\mathrm{We_d} \gg 1$ and $t \le t_{\max}$ according to (6.8). The scaling (6.10) is robust as the same relation is found for the neck region, i.e. $r = R(t)$, based on s (6.9), (6.8), and using $\tau_c/\tau_i \sim \mathrm{We_d}^{1/2}$.

In conclusion, the sheet model (6.8, 6.9) captures the kinematics of the deforming drop accurately until the fragmentation severely changes the topology of the deforming liquid body. The kinetic-energy partition $E_{\mathrm{k,d}}/E_{\mathrm{k,cm}}$ allows for a treatment of different impact conditions in the MEK and tin system that originate from the different laser-matter interactions. As a consequence, drops in the MEK system expand faster into thin sheets as compared to tin drops for the same Weber number. The sheet model leads to the same scaling for a characteristic sheet thickness in the center and neck region of the sheet, where we observe the first hole nucleation during the sheet breakup. With a solid description of the kinematics for the liquid sheet at hand we now turn to the rim breakup in Section 6.7 and the sheet breakup in Section 6.8.

6.7 Rim breakup

Our goal is to find a prediction for the number of ligaments N_ℓ that are expelled radially outward as a result of the rim breakup. To this end, we determine at what time t_ℓ a Rayleigh–Plateau and Rayleigh–Taylor instability manifest themselves on the rim. From the sheet radius and the characteristic wavenumber k_ℓ at that time follows then the number of ligaments $N_\ell \sim R(t_\ell)\, k_\ell$. Based on the similarity between our expanding sheet and the one occurring after the mechanical impact of a drop on a solid, we follow a similar approach as [101].

The evolution of the rim breakup that finally results in the radial expulsion of ligaments is illustrated for tin at $\mathrm{We_d} = 140$ in Fig. 6.9. Corrugations with an amplitude ξ develop on the rim and are visible in the experiments initially as mere noise and later as a perturbation with a characteristic wavenumber k_ℓ. We define the latter moment as the time t_ℓ of rim breakup. Once the ligaments have manifested themselves on the rim, their number N_ℓ only changes due to the compression of the rim at $t > t_{\max}$ when the sheet starts to recoil: individual ligaments that are still attached to the sheet approach each other such that they merge at their base as shown in Fig. 6.9 (c, d). The corresponding decrease of N_ℓ over time in Fig. 6.9 (a) is thus not a result of an instability rearranging the fluid, but a mere consequence of the compression of the rim.

We observe the development of ligaments before the sheet starts to recoil at $t_{\max}$ as shown in Fig. 6.10: the moment we observe the manifestation of the corrugations as radial ligaments decreases with increasing Weber number. Following [101], we describe the rim as a liquid cylinder of diameter $b \sim R_0 \mathrm{We_d}^{-1/4}$ and neglect its curvature, which is valid for our experiments since $k_\ell\, R \gg 1$. The rim is stretched over time at a rate $\dot{R}/R$ and sits in a decelerating frame with a time-dependent acceleration $-\ddot{R}(t)$. Two destabilization mechanisms play a role in such a case. First, the capillary destabilization by a Rayleigh–Plateau mechanism affects the rim of constant diameter b. The associated timescale of the capillary instability is then $(\rho\, b^3/\gamma)^{1/2} \sim \tau_c \mathrm{We_d}^{-3/8}$, which is in agreement with our experimental observation in Fig. 6.10. Second, a Rayleigh–Taylor mechanism is at play, where an associated body force proportional to $-\rho\, \ddot{R}$ pushes the fluid particles in the rim radially outward. The growth rate of the corrugation in a local frame tangent to the rim is then [101]

$$\frac{\mathrm{d}}{\mathrm{d}t} \ln\left(\frac{\xi}{R}\right) = -\frac{\dot{R}}{R} + \mathrm{Re}(-i\omega), \tag{6.12}$$

where ω is the instantaneous growth rate.The first term on the right-hand side in (6.12) is the stretching of the rim that actually damps the growth of the perturbation during the expansion of the sheet for $t < t_{\max}$. The timescale of the damping is set by τ_c, independent of the Weber number [101]. The second term

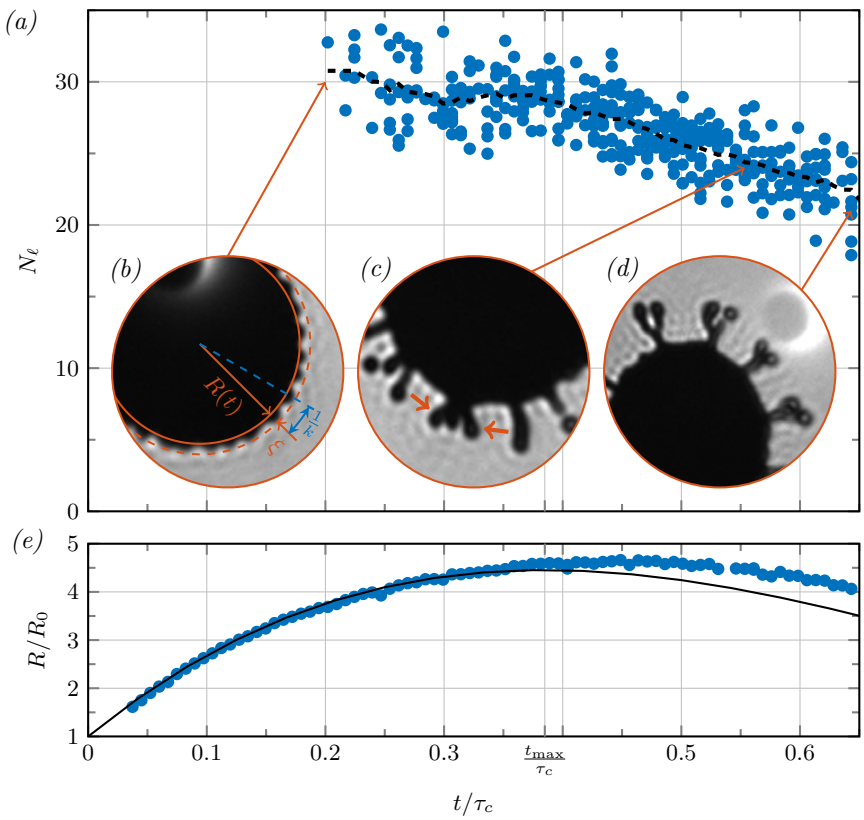

FIGURE 6.9: Evolution of the rim breakup for $\mathrm{We_d} = 140$ as function of dimensionless time t/τ_c obtained for a tin experiment that exhibits a near-perfect axisymmetric expansion. (a) Total number of ligaments N_ℓ, where blue circles indicate individual realizations of the experiment and the dashed black line is a running average. The inset (b) shows the sheet radius $R(t)$, the amplitude ξ, and the wavenumber k of the corrugation as observed at $t/\tau_c = 0.2$. During the recoil of the sheet at $t > t_{\max}$ two or more ligaments may merge as shown in inset (c) and (d). (e) Sheet radius $R(t)$ for each realization and the trajectory (solid black line) from (6.8).

on the right-hand side in (6.12) amplifies the corrugation with an instantaneous growth rate ω that depends on $\mathrm{We_d}$. The associated timescale of the amplification is $\omega^{-1} \sim (\rho \ddot{R}^3/\gamma)^{-1/4} \sim \tau_c \mathrm{We_d}^{-3/8}$, which is the same timescale as found for the Rayleigh–Plateau mechanism. In our experiments, $\mathrm{We_d} \gg 1$ such that the

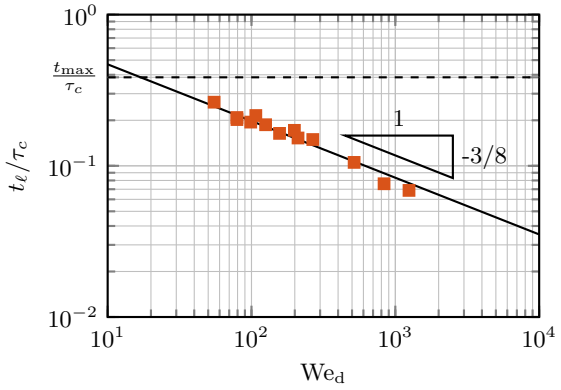

FIGURE 6.10: The time t_ℓ when corrugations similar to the ones in Fig. 6.9 (b) become visible on the bordering rim as a function of Weber number $\mathrm{We_d}$. The data is acquired manually from a subset of tin experiments that are recorded at identical camera and lighting conditions to exclude an influence of the image resolution. The prefactor of the scaling law (solid black line) is 1.1.

timescale of the Rayleigh–Taylor instability is separated from the expansion dynamics. As a consequence, the damping due to the stretching is irrelevant for large Weber numbers allowing for the instability to manifest itself on the rim at early times, that is

$$t_\ell \sim \tau_c \, \mathrm{We_d}^{-3/8}. \tag{6.13}$$

The wavenumber k_ℓ for which ω in (6.12) reaches a maximum is $k_\ell \sim (-\ddot{R}\,\rho/\gamma)^{1/2} = \mathrm{We_d}^{1/4}/R_0$ [101]. From the timescale t_ℓ of the destabilization and the corresponding wavenumber k_ℓ we can determine N_ℓ. The expansion dynamics (6.8) can be approximated for $t \leq t_{\max}$ by $R/R_0 \sim \mathrm{We_d}^{1/2}\, t/\tau_c$ leading finally to

$$N_\ell \sim k_\ell \, R(t_\ell) \sim \mathrm{We_d}^{3/8}. \tag{6.14}$$

The scaling exponent of 3/8 in (6.14) deviates from the scaling of 3/4 in terms of the Weber number as proposed by [101]. In their study, the time of maximum expansion is assumed to be the characteristic time of the destabilization, i.e. $t_\ell = t_{\max} \sim \tau_c$. And indeed, in Section 6.6 we saw that at $t \sim t_{\max}$ the rim breakup affects the sheet kinematics considerably, but we observe the manifestation of the instability at an earlier point in time leading to the different scaling with Weber number.

We validate the scaling (6.14) experimentally as shown in Fig. 6.11. Since the number of ligaments in the experiments only changes by the rim compression for

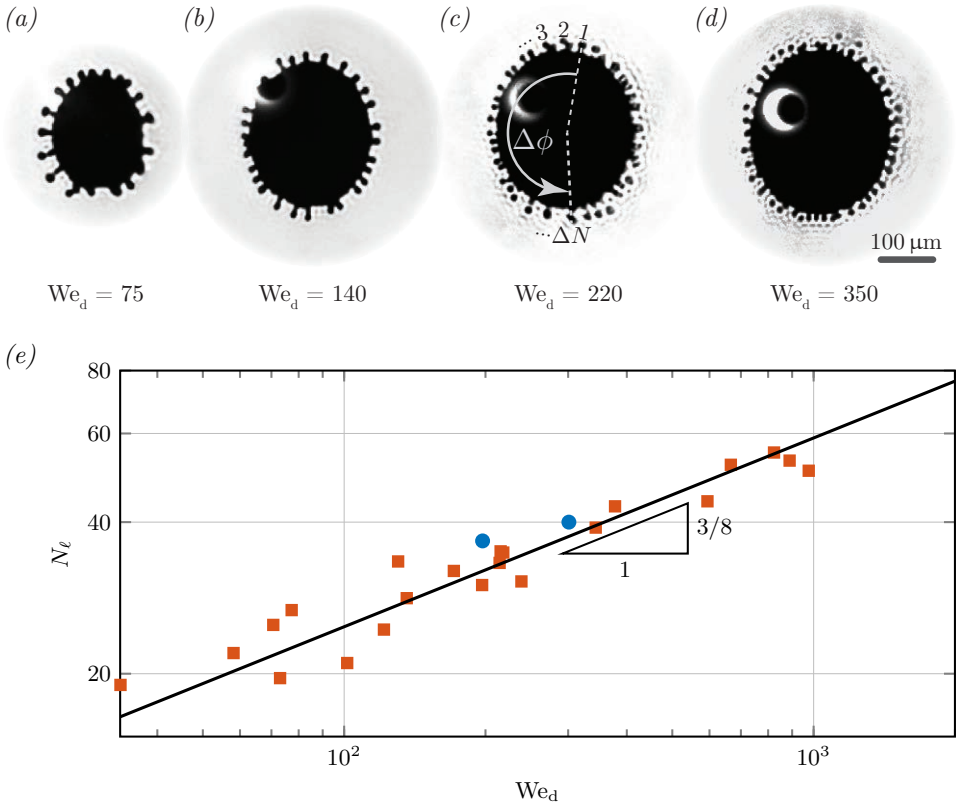

FIGURE 6.11: (a–d) Radial expulsion of ligaments during the rim breakup for increasing Weber number We_d (left to right). The back-view images are taken from experiments with tin drops that exhibit a near-perfect axisymmetric expansion. The optical resolution may limit the detection of ligaments to a fraction $\Delta\phi/2\pi$ of the rim as illustrated in (c).In such cases, the expected total number of ligaments N_ℓ is estimated by $N_\ell = 2\,\pi\,(\Delta N - 1)/\Delta\phi$. (e) Number of radially expelled ligaments N_ℓ as function of the Weber number We_d for tin (red squares) and MEK drops (blue circles). The data for MEK is limited to two experiments, since the early hole nucleation in the neck region affects the rim breakup and prevents an accurate measurement for larger Weber numbers. The prefactor of the scaling law (solid black line) is 4.4.

$t > t_{max}$, we can obtain N_ℓ as function of We_d by simply counting the number of ligaments that are pointing radially outward during $t_\ell \le t \le t_{max}$, which is illustrated in Fig. 6.11 (a–d). The obtained scaling with We_d in Fig. 6.11 (e) is in

good agreement with our prediction (6.14) with a prefactor of 4.4. The limited range in $\mathrm{We_d}$ for which data can be obtained for the MEK experiments prevents a detailed comparison for the two systems in terms of the scaling exponent. The sheet breakup takes place in the MEK system much earlier in comparison to the tin system as we already mentioned in Section 6.6. The neck breakup in direct vicinity to the rim limits then the range in $\mathrm{We_d}$ for which can obtain a reliable measurement of N_ℓ in the MEK system. However, the MEK data points (blue circles) that we did mange to obtain follow the same scaling (6.14) with the same prefactor as the tin data (red squares). Hence, we conclude that the difference in rim breakup between MEK and tin is completely captured by the rescaled Weber number $\mathrm{We_d}$ that accounts for the different driving mechanism, in particular the effect of the plasma dynamics on the expansion of the tin sheets.

6.8 Sheet breakup

The questions we aim to answer in the analysis of the sheet breakup are analogous to the rim breakup: When does the sheet break and which characteristic wavenumber is selected during the breakup? We already found an agreement in Section 6.5 between our observations for the nucleation, growth, and merging of holes and an analogous process for a manually prepared liquid film that is accelerated by a shockwave [102]. The analogy suggest the same mechanism as cause of the sheet destabilization for the laser impact on a drop: an impulsive Rayleigh–Taylor instability. However, the sheets in our experiments are not subject to a direct acceleration of either one of their interfaces. Only the spherical drop is accelerated on the timescale τ_e and the sheets, as well as a potential Rayleigh–Taylor instability, must develop simultaneously until the sheet breaks on the timescale τ_c. As a consequence, we study the sheet breakup in Section 6.8.1 in more detail to convince ourselves that it shows typical features of an instability before we propose a model in Section 6.8.2 to answer our questions.

6.8.1 Observations

We first recognize that the Weber number not only sets the expansion dynamics (6.8) and (6.9) when rescaled by the energy partition $E_{\mathrm{k,d}}/E_{\mathrm{k,cm}}$, but also represents the initial drop acceleration a on the timescale τ_e. In comparison to τ_i and τ_c the acceleration can be considered impulsive and is then given by $a \sim U/\tau_e = R_0/(\tau_c\ \tau_e)\,\mathrm{We}^{1/2}$. Since R_0 and τ_c are kept constant in each experimental setup and τ_e is found to be constant as well for both vapor-driven and plasma-driven drops, $\mathrm{We}^{1/2}$ is a direct scale for the impulsive acceleration in our experiments. As a result, our observations cannot distinguish between a stronger

accelerations on the one hand and a faster expansion on the other hand. Both are coupled and cannot be set independently, unless $E_{\mathrm{k,d}}/E_{\mathrm{k,cm}}$ could be controlled experimentally in both systems.

Figure 6.12 shows the breakup of MEK sheets for one decade in Weber number. In case the laser impact is severe enough a minimum Weber number is achieved to observe the sheet breakup. A further increase in Weber number (Fig. 6.12 (b–e)) leads to a more severe fragmentation process as the number of holes N_b that pierce the sheet per unit area A and the corresponding wavenumber $k_b \sim (N_b/A)^{1/2}$ are increased. Our observation for the increase in k_b with We is a clear signature of a fluid-dynamics instability and in agreement with the study on liquid films by [102]. The mode selection, i.e. the characteristic wavenumber k_b observed in their experiments, was captured in the analysis by an impulsive Rayleigh–Taylor instability. In addition, the characteristic time of the instability development was found to be a function of We as well. Our experiments also reveal a faster fragmentation process for an increase in Weber number, see Fig. 6.12 (b–e). However, only the analysis can reveal whether the time dependency in our experiments is a result of a stronger acceleration or mere consequence of faster sheet dynamics.

A characteristic scale for the sheet thickness h_{b} at the moment of breakup shall help to exclude other mechanisms than a fluid-dynamic instability as cause of the destabilization. The minimum Weber number for sheet breakup to occur in the MEK system (Fig. 6.12 (a)) translates to a radial sheet expansion of $R/R_0 > 6$ (similar expansions are required to cause destabilization for tin sheets). The scaling (6.10) leads then to the typical sheet thickness $h_{\mathrm{b}}/R_0 \sim 10^{-2}$. We confirm by high-speed recordings of individual piercing events on MEK sheets that the hole-opening speed agrees with the Taylor–Culick speed $v \sim \sqrt{\gamma/h_{\mathrm{b}}\rho} \sim 1\,\mathrm{m/s}$ [123] as set by

FIGURE 6.12: (Figure is found on the following page.) Sheet breakup for increasing Weber number We in back-view images taken from MEK experiments. (a) The sheet is smooth and starts to recoil from its maximum radius $R_{\max}/R_0 = 6$ reached at $t/\tau_c = 2/\sqrt{27} \approx 0.38$, the moment the image is taken. The rim breakup leads to the formation of ligaments but the breakup of the thin sheet itself is not observed. A slight increase in the Weber number leads however to single breakup events on the sheet (not shown). (b–e) The sheets are first pierced near their neck and in the center before $R_{\max}$ is reached. The images are taken shortly after the first piercing event to allow for a characteristic hole density to develop, since the piercing is subject to fluctuations. The dimensionless time of each image is decreasing $t/\tau_c = 0.3,\ 0.2,\ 0.15,\ 0.12$ (b–e) with increasing Weber number. The shadowgraph visualization with a small numerical aperture is sensitive to any light refraction such that corrugations on the thin sheet just before breakup become visible. With increasing We, we observe a larger hole density resulting in a finer web of ligaments.

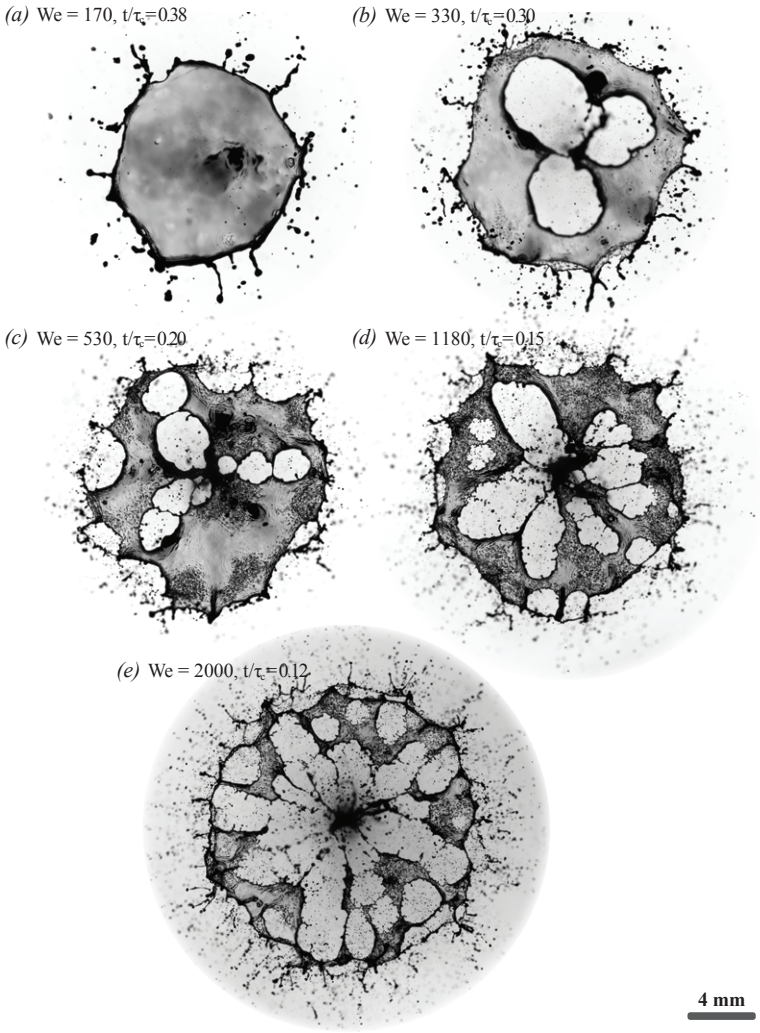

FIGURE 6.12: (Continued from the previous page.)

our estimate of h_b. The typical scale of h_b in absolute terms is then a few tens of micrometer for the MEK sheets and a fraction of a micrometer for the tin sheets. We prevent solid impurities of such a length scale to enter the initial MEK drops by an appropriate filtration as explained in Section 6.3. Furthermore, we exclude by high-speed recordings for selected experiments that the breakup is caused by individual fragments impacting on the sheet. The ejected mass during the early jetting phenomena, a likely candidate for fragments, travels at a velocity larger than the center-of-mass velocity U of the expanding sheet preventing any collision with the sheet at later times. Van der Waals forces can be important when the film thickness is in the range of several tens of nanometer [124], but even the tin sheets at a micrometer-scale are not yet thin enough for this effect to be relevant. The combination of two liquid systems at vastly different scales is to our advantage here: any mechanism proposed as cause for the breakup must hold for both systems, the framework of an impulsive Rayleigh–Taylor instability being the most likely one in view of our observations.

A Rayleigh–Taylor instability amplifies initial perturbation until their amplitude severely affects the topology of the liquid body. Following [102], the sheets in our experiment are then most likely pierced when the amplitude of the instability is of the order of the local sheet thickness. A fragmentation process based on the amplification of initial perturbations, which can be as small as the thermal noise in a system [105], is expected to show a stochastic nature. We therefore elucidate whether the hole nucleation and the formation of the characteristic web of ligaments (Fig. 6.12 (b–e)) is set by deterministic or stochastic influences, or a combination of the two.

The patches of corrugations that precede the hole formation as described in Section 6.4 are also visible in Fig. 6.12 (b–e) and are an indication for the destabilization of the liquid sheet to occur. Vice versa, corrugations with a high spatial frequency are absent on stable sheets (Fig. 6.12 (a)). We observe no direct relation between the spatial frequency of the corrugation k_corr and the wavenumber k_b of holes piercing the sheet in a corrugated area: only a few holes pierce a corrugated area on MEK sheets, i.e. $k_\mathrm{corr} \gg k_b$. However, we can use the appearance of corrugations as an indication where holes are likely to occur. To this end, we use an image-analysis algorithm that is sensitive to spatial frequencies much larger than the hole density, see Fig. 6.13 (a). From the data of approximately 100 experimental realizations, one of which is shown in Fig. 6.13 (b), we obtain the probability density function (PDF) for likely areas of hole nucleation in radial direction as shown in Fig. 6.13 (c). Not surprisingly, our quantitative analysis recovers the areas of hole nucleation that we already identified visually in Section 6.4: the neck and center region of the sheet breakup. With the two regions identified by a bimodal Gaussian distribution we recover the PDF in azimuthal direction for each

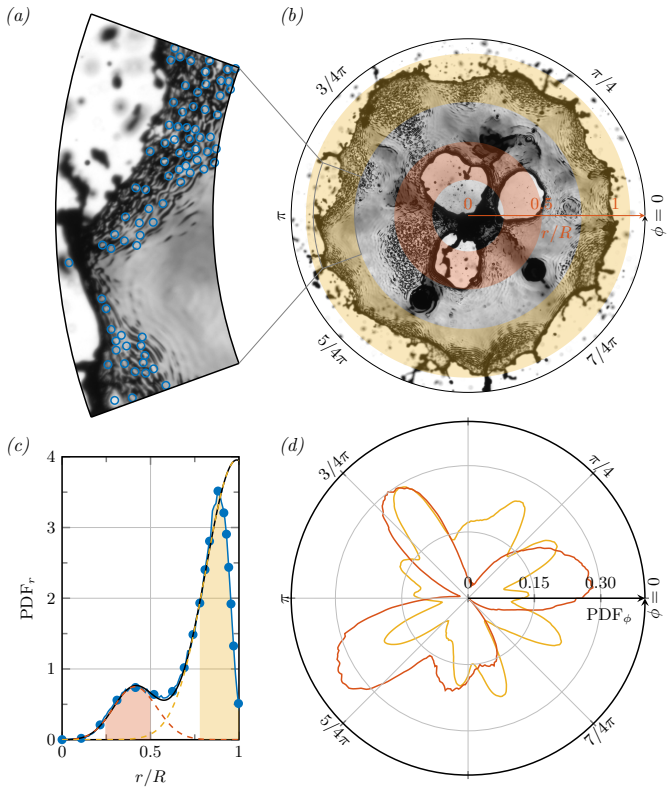

FIGURE 6.13: Hole nucleation on MEK sheets at We = 440. (a) Magnified section of the sheet in (b) illustrating the result of an algorithm to detect corrugations that precede the sheet breakup: a cross-correlation of the image and a Gaussian kernel with a standard deviation $\sigma \sim 1/k_{\mathrm{corr}}$ identifies local corrugations (open blue circles), where $1/k_{\mathrm{corr}}$ is a scale for the spatial frequency of the corrugations. (b) Sheet from a single realization of the experiment, where the center and neck region of the sheet breakup as identified by the analysis shown in (c) are highlighted (neck in yellow, center in red). (c) Probability density function (PDF) for the radial location r/R of the local sheet corrugations found in approximately 100 realizations of the experiment. The PDF is approximated by $\mathrm{PDF} = 2\, r/R\, g(r)$, where $g(r)$ is the radial modulation that describes the deviation of the hole nucleation location from a random distribution. The experimental data (connected blue circles) is well described by a two-component Gaussian mixture model $g(r|\mu_i, \sigma_i)$ (solid black line) with μ_i and σ_i being the mean and standard deviation of the radial location of hole nucleation. The highlighted areas, i.e. $\mu_i - \sigma_i \leq r/R \leq \mu_i + \sigma_i$, illustrate the preferred hole locations in the center (red area, $\mu = 0.37$, $\sigma = 0.13$) and the neck region (yellow area, $\mu = 0.96$, $\sigma = 0.180$) of the sheet. (d) PDF of the azimuthal position ϕ of preferred hole locations for the center (red line) and neck region (yellow line) of the sheet breakup.

radial region (Fig. 6.13 (d)). Also here, we recognize a deterministic influence with three preferred locations of hole piercing in the center region and approximately six preferred areas of destabilization in the neck region. In agreement with these findings, the final web of ligaments preserves the deterministic influence as illustrated for a large Weber number We = 2000 in Fig. 6.14.

The deterministic facets of the sheet fragmentation are not in contradiction to a Rayleigh–Taylor mechanism. The instability can very well be the cause for the hole piercing but its visual appearance is convoluted by a deterministic profile in the sheet thickness h. We clearly observed a radial dependency in the sheet thickness that needed to be included in our quantitative description of the expansion dynamics in Section 6.6 to accurately describe our experimental data. In addition, we noticed azimuthal modulations in the sheet thickness in Section 6.4. Although these modulations do not affect the expansion dynamics considerably, the sheet thickness varies locally during the late-time expansion. The physical cause for azimuthal modulations can be found in the driving mechanism as explained in

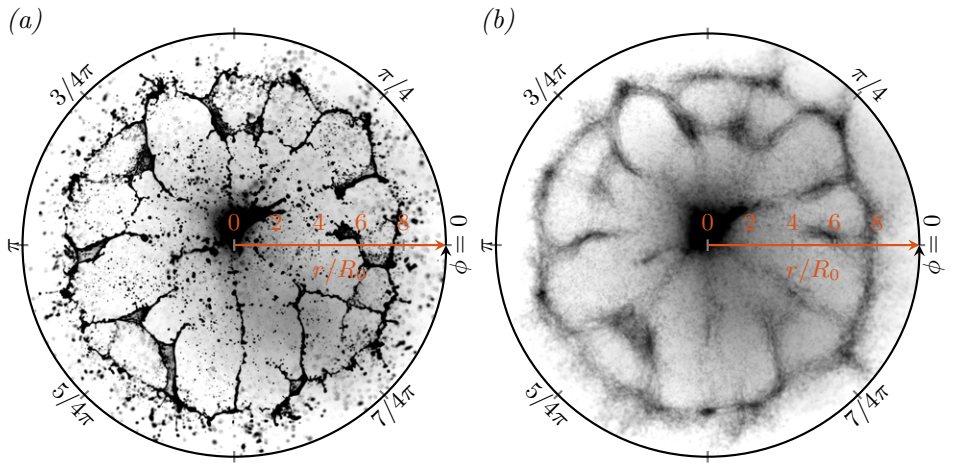

FIGURE 6.14: (a) Back-view of a single experiment for an MEK drop at We = 2000 and $t/\tau_c = 0.15$. The nucleation, growth, and merging of holes on the sheet leads to a web of ligaments. (b) Overlay of 31 back-view images at $t/\tau_c = 0.15 \pm 0.006$ for the same experimental condition as in (a) but taken from separate, independent realization of the same experiment. The gray value in the overlay image is a measure for the probability that ligament are present at the same position in all 31 realization of the same experiment, where a black pixel means that in all experiments a ligament is found at a particular position. The overlay reveals a deterministic influence on the final web of ligaments during the sheet fragmentation.

Section 6.2: the vapor-driven MEK drops are subject to azimuthal modulations in the initial acceleration of about ±10% in amplitude. As these modulations are deterministic, that is fixed in the lab reference frame, the fragmentation also shows deterministic aspects.

To observe the stochastic nature of hole nucleation we then need to find an experiment where the characteristic wavelength of hole nucleation is small in comparison to the spatial extent L of local thickness variations, that is $k_b L \gg 1$. In Fig. 6.15 we show a corresponding case for the center breakup of a tin sheet at $\mathrm{We} = 30\,000$. The hole nucleation with a wavenumber k_b in the center of the sheet is observed to take place on an area with radial extent L_c such that $k_b L_c \gg 1$. Such a case allows us to sample the process of hole nucleation in large numbers to obtain unbiased statistics, i.e. unaffected by large-scale variations in the sheet thickness. Our analysis for the location of piercing events recovers a distribution as expected for a stochastic process (Fig. 6.15 (b, c)). With the experimental observation of random hole nucleation we conclude on the destabilization mechanism. The physical mechanism of the sheet breakup is a fluid-dynamic instability that is affected by large-scale variations in the sheet thickness. In particular, we anticipate a Rayleigh–Taylor instability that is driven by the impulsive acceleration of the drop at τ_e. Our analysis in the next section then leads to a prediction for the characteristic time of destabilization, which we can validate experimentally.

6.8.2 Model derivation and comparison to experiment

Here, we describe the model to predict the sheet breakup taking into account the characteristics of the laser impact. We identified a Rayleigh–Taylor instability as mechanism for the sheet destabilization that is initiated by the impulsive acceleration of the drop surface at τ_e. Any perturbations that are present on the accelerated interface of the drop are then amplified during this early-time of sheet breakup. At later times $t > \tau_e$ the perturbations continue to evolve in absence of an external acceleration, while still affected by capillary restoring forces as the overall topology of the drop is changing as well. We aim to capture two characteristics of the drop evolution in our analysis: the change from a spherical drop to a sheet on the timescale τ_i and the expansion of the drop into a thin sheet at τ_c, both are a late-time consequence of the initial acceleration. Our arguments are based on the analysis by [102] for thin liquid films that were also accelerated impulsively. In our case, the sheets are then most likely pierced when the perturbation amplitude is of the order of the sheet thickness. We therefore trace the perturbation amplitude from the early-time τ_e to the late-time τ_c, where we observed the breakup in the experiments.

Figure 6.16 sketches the evolution of a Rayleigh–Taylor instability on a deforming drop in three distinct phases. The first phase (Fig. 6.16 (a)) describes the

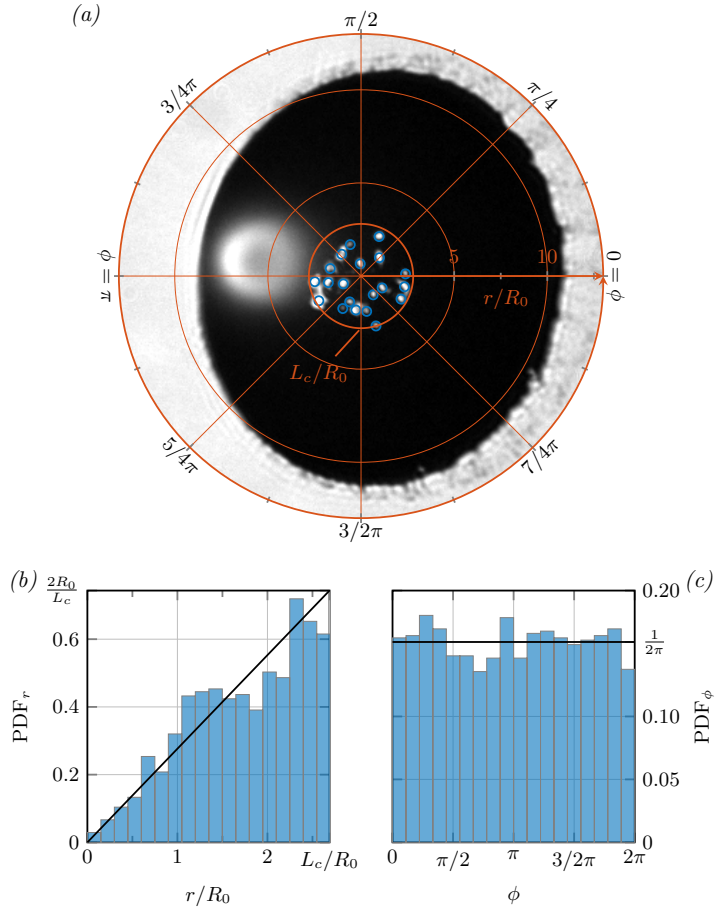

FIGURE 6.15: Hole nucleation in the center of tin sheets at We = 30 000. (a) A single realization of the experiment with individual holes highlighted (open blue circles) as detected by an image-analysis algorithm that is sensitive to variations in the gray value. Approximately 100 realizations of the experiment lead to a spatial distribution of hole nucleation events, where the area that holds 90 % of these events is marked by the circle $L_c/R_0 = 2.7$ in (a). For this area, the radial (b) and azimuthal distribution (c) of nucleation events is obtained. The experimental distributions (in blue) agree with the corresponding prediction for a random nucleation process (black line), where it follows from geometric arguments: $\mathrm{PDF}_r = 2r/L_c$ and $\mathrm{PDF}_\phi = 1/(2\pi)$. The wavenumber k_b of hole nucleation is found from the total number of holes N_b identified in n realizations of the experiments to be $k_b R_0 = (R_0^2 N_b/(\pi n L_c^2))^{1/2} = 0.86$.

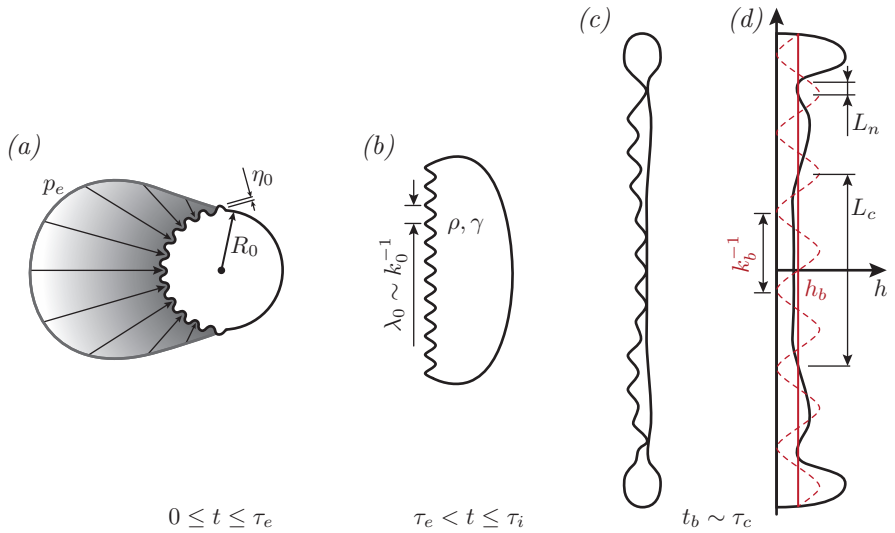

FIGURE 6.16: Sketch of a model to describe the evolution of an impulsive Rayleigh–Taylor instability on a deforming drop. (a) One side of the drop is accelerated perpendicular to the surface by the pressure p_e on the timescale τ_e. The acceleration a amplifies the Fourier modes of initial amplitude η_0 and wavenumber k_0. (b) The drop deforms into a sheet on the timescale τ_i in absence of any external acceleration. (c) The sheet expands considerably until it breaks at the time t_b when the perturbation amplitude is of the order of the sheet thickness h_b. (d) A thickness profile showing two regions of size L_n and L_c where the criterion for breakup is fulfilled and holes are expected to nucleate with a characteristic wavenumber k_b.

acceleration of the drop, where in comparison to τ_i and τ_c the acceleration can be considered impulsive and is then given by a step function equal to $a \sim U/\tau_e = R_0/(\tau_c\ \tau_e)\,\mathrm{We}^{1/2}$ for $0 \le t \le \tau_e$ and equal to 0 for $t > \tau_e$. In our model the drop is assumed to be a sheet with thickness $h_0 \sim R_0$ and density ρ that is surrounded by a gas phase of negligible density. One interface of the sheet is then accelerated perpendicular to its surface. The acceleration a amplifies any initial modulation of the surface, which can be represented by the Fourier modes

$$\eta(s,t) = \eta_0\, f(t)\, \mathrm{e}^{iks}, \tag{6.15}$$

where η_0 is the initial amplitude and s a generalized coordinate tangent to the sheet in the following analysis. The temporal evolution $f(t)$ is determined by the instantaneous growth rate $\omega(k)$, i.e. the dispersion relation specific to each of the three phases.In the second phase (Fig. 6.16 (b)), the drop is not accelerated any

more but the Fourier modes continue to exist on a drop that evolves into a sheet on the timescale τ_i. The third phase (Fig. 6.16 (c)) is characterize by the large expansion of the sheet on the timescale τ_c, during which we observe the actual breakup. The sheet is then pierced when the thickness modulations are of the order of the sheet thickness [102], compare also Fig. 6.16 (d). We neglect in our analysis the local thickness variations (marked by L_c and L_n in Fig. 6.16 (d)) that lead to the preferred areas of hole nucleation as seen in the previous section, since the underlying mechanism of destabilization is unaffected by those imperfections. Consistently, we make use of the robust scaling (6.10) for the overall kinematics of the sheet.

Lengths and times are made non-dimensional in the analysis by the initial drop radius R_0 and capillary time τ_c,

$$\hat{\omega} = \omega\,\tau_c,\ \hat{t} = \frac{t}{\tau_c},\ \hat{k} = kR_0,\ \text{and}\ \hat{k}_c = \sqrt{\frac{\rho a R_0^2}{\gamma}}, \tag{6.16}$$

where $\hat{k}_c$ is the capillary wavenumber. Following [102], we treat the acceleration $a = R_0/(\tau_c\ \tau_e)\,\mathrm{We}^{1/2}$ in the first phase as impulsive, i.e. we assume $1/\hat{\omega}_1 \gg \hat{\tau_e}$. Since $\hat{k}_{c,1} = \mathrm{We}^{1/4}{\hat{\tau_e}}^{-1/2} \gg 1$, the sheet can be considered thick with respect to the capillary length, which leads to the dispersion relation [102]

$$\hat{\omega}_1^2 = \hat{k}^3 - \hat{k}_{c,1}^2\hat{k}. \tag{6.17}$$

The initial conditions for the shape function $f(t)$ in (6.15) are

$$f_1(\hat{t}=0) = 1 \text{ and } f_1' = \frac{\mathrm{d}f_1}{\mathrm{d}\hat{t}} = 0, \tag{6.18}$$

such that we allow all unstable modes that fit inside the drop, that is $1 \le \hat{k} \le \hat{k}_{c,1}$, to grow with the same initial amplitude and zero initial speed. The solution of $f_1(t)$ then follows from [102, 125]

$$\frac{\mathrm{d}^2 f_1}{\mathrm{d}\hat{t}^2} = -\hat{\omega}_1^2 f_1(\hat{t}) \tag{6.19}$$

and is found to be

$$f_1(\hat{t}) = \cos\left(\hat{k}^{3/2}\hat{t}\right) + \frac{\mathrm{We}^{1/2}}{\hat{k}^2\hat{\tau_e}}\left(1 - \cos\left(\hat{k}^{3/2}\hat{t}\right)\right). \tag{6.20}$$

Assuming an impulsive acceleration, we expand this solution for $\tau_e \to 0$ and find for the amplitude and growth rate at the end of phase 1: $f_1(\hat{\tau_e}) \approx 1$ and $f_1'(\hat{\tau_e}) \approx$

$\mathrm{We}^{1/2}\hat{k}$. Each mode has therefore a specific growth rate as a result of the impulsive acceleration. However, the amplitude remains unchanged in phase 1, which is a direct consequence of our assumption $1/\omega_1 \gg \tau_e$.

The Fourier modes in phase 2 and 3 are not directly amplified by an acceleration, that is $\hat{k}_{c,2} = \hat{k}_{c,3} = 0$. In phase 2, the dispersion relation (6.17) reads then $\hat{\omega}_2^2 = \hat{k}^3$ and the mode development is in view of (6.19) described by $f_2'' = -\hat{k}^3 f_2$. The initial conditions

$$f_2(\hat{t}=0) = 1 \text{ and } f_2'(\hat{t}=0) = \hat{k}\mathrm{We}^{1/2} \tag{6.21}$$

match the second phase to the result obtained in the first phase. The solution is then a free harmonic oscillator

$$f_2(\hat{t}) = \cos\Big(\hat{k}^{3/2}\hat{t}\Big) + \frac{\mathrm{We}^{1/2}}{\hat{k}^{1/2}} + \sin\Big(\hat{k}^{3/2}\hat{t}\Big). \tag{6.22}$$

This solution for phase 2 is derived under the assumption of thick sheet, i.e. the dispersion relation characteristic of an infinite medium, i.e. $\hat{\omega}_2^2 = \hat{k}^3$, was used. Consequently, as the drop expands into a thin sheet the solution (6.22) will inevitably be invalid at some point during the expansion when the two interfaces of the sheet are coupled by the Laplace pressure. This time defines the transition from the second to the third phase of the model and is most likely given by τ_i, i.e. the timescale on which we observed the transition of the drop to a thin sheet in Section 6.4.We now assume a sheet expansion that is fast in comparison to the frequency of the harmonic oscillation described by (6.22), i.e. the sheet is thin at τ_i while all Fourier modes are still in their first oscillation. Comparing τ_i to the period of oscillation for each mode requires then $\hat{k}^{3/2}\,\mathrm{We_d}^{-1/2} \ll 1$ for the assumption to be valid, which is justified for our experiments with $\mathrm{We_d} \gg 1$. As a consequence, we expand the solution (6.22) in the limit $\hat{k}^{3/2}\hat{t} \to 0$ to obtain

$$f_2 \approx 1 + \mathrm{We}^{1/2}\hat{k}\hat{t} - \tfrac{1}{2}\hat{k}^3\hat{t}^2, \tag{6.23}$$

$$f_2' \approx \mathrm{We}^{1/2}\hat{k} - \hat{k}^3\hat{t}, \tag{6.24}$$

which is used to determine the mode $\hat{k}_{\max}$ with the largest growth rate according to $\mathrm{d}(f_2')/\mathrm{d}k = 0$. The result $\hat{k}_{\max} = \mathrm{We}^{1/4}/(3\hat{t})^{1/2}$ is time dependent, since each mode resonates with its intrinsic frequency during the second phase. Our choice for the transition to the third phase of the model determines then the fastest growing mode $\hat{k}_{\max}(\tau_i)$ at the end of the second phase.

Phase 3 is characterized by the expansion of the sheet to $\hat{R} \gg 1$ until the amplitude of the fastest growing mode is of the order of the sheet thickness (Fig. 6.16 (d)). We describe the mode development in the third phase by the thin-sheet dispersion relation, since we assume $k(t_b)h(t_b) \ll 1$. In absence of any acceleration the dispersion relation for a thin sheet is $\hat{\omega}_3 = (kh)^4/2$ [102] and when normalized in

agreement with definition (6.16) we obtain $\hat{\omega}_3 = \hat{h}\hat{k}^4/2$.In phase 1 and 2, we neglected the effect of the sheet expansion on the dispersion relation of the modes. However, the characteristic of the third phase is just this expansion and simultaneous thinning of the sheet. We now take the effect of the sheet expansion on $\hat{\omega}_3$ into account by a self-similar stretch. Each quantity before the stretch, i.e. at the end of the second phase, is denoted by the subscript 0 such that the self-similar stretching reads $k_0 R_0 = kR$ and $\eta_0/k_0^2 \sim \eta/k^2$. The former is the effect of the radial sheet expansion that stretches the wavelength of a given perturbation and the latter is the contraction of the perturbation amplitude resulting from mass conservation. Introducing the kinematics (6.10) of the sheet then leads to

$$\hat{k} = \hat{k}_0\, \hat{R}^{-1} \text{ and } \frac{\eta}{h} = \frac{\eta_0}{R_0}. \tag{6.25}$$

Combining this self-similar stretching with the scaling laws (6.10) and (6.11) for the sheet kinematics we now recognize that the instantaneous growth rate during the expansion in phase 3 decays much faster then the sheet thins: $\hat{\omega}_3 \sim \hat{t}^{-6}$ and $\hat{h} \sim \hat{t}^{-2}$. In conclusion, the sheet expansion and simultaneous thinning literally freezes the growth rate of the perturbation in its state at the end of the second phase, that is $f_3'' \approx 0$ for $t > \tau_i$. As a result, the amplitude of the instability than evolves as

$$f_3(\hat{t}) = f_2(\hat{k}_{\max}, \hat{\tau}_i) + f_2'(\hat{k}_{\max}, \hat{\tau}_i)\hat{t} \approx \mathrm{We}\left(\frac{E_{\mathrm{k,d}}}{E_{\mathrm{k,cm}}}\right)^{1/2} \hat{t}, \tag{6.26}$$

where we made use of $\hat{\tau}_i = \mathrm{We}_{\mathrm{d}}^{-1/2}$. We now acknowledge that the choice for τ_i as the characteristic time for the sheet thinning introduces the energy partition $E_{\mathrm{k,d}}/E_{\mathrm{k,cm}}$ for the first time in our analysis.

Following [102], the time of breakup t_b is now found when the perturbation amplitude is of the order of the sheet thickness, that is

$$\frac{\eta_0}{R_0} f_3(t_b) = 1, \tag{6.27}$$

where we take into account the thinning (6.25). Once t_b is known the wavenumber at breakup $\hat{k}_b$ is obtained by applying the stretching (6.25) to the result $\hat{k}_{\max}(\hat{\tau}_i)$ from the second phase. As a final result, we obtain as prediction for the sheet breakup

$$\frac{t_b}{\tau_c} \sim \left(\frac{\eta_0}{R_0}\right)^{-1} \mathrm{We}^{-1} \left(\frac{E_{\mathrm{k,d}}}{E_{\mathrm{k,cm}}}\right)^{-1/2}, \tag{6.28}$$

$$k_b R_0 \sim \frac{\eta_0}{R_0}\, \mathrm{We} \left(\frac{E_{\mathrm{k,d}}}{E_{\mathrm{k,cm}}}\right)^{1/4}. \tag{6.29}$$

These scaling laws for the breakup time t_b and the characteristic wavenumber k_b of hole nucleation are expressed in terms of the initial amplitude of the perturbation in relation to the drop size η_0/R_0, the Weber number We, and the energy partition $E_{\mathrm{k,d}}/E_{\mathrm{k,cm}}$. The stronger dependency of t_b on We in comparison to $E_{\mathrm{k,d}}/E_{\mathrm{k,cm}}$ as expressed by the scaling exponents is evident for our experiments. We already recognized that Weber number affects both the initial acceleration and the sheet kinematics. It entered our model therefore already in the first phase when the growth rate of the Fourier modes are set. In addition, the Weber number also set the scaling for the kinematics (6.10) and (6.11) that we used in the third phase of our model. In contrast to the Weber number, the energy partition only influences the late-time evolution of the sheet. $E_{\mathrm{k,d}}/E_{\mathrm{k,cm}}$ enters therefore our model only in the third phase: it affects the characteristic time τ_i, i.e. the time phase 3 is assumed to begin, and the expansion rate of the thin-sheet, which leads to the weaker scaling exponent for $E_{\mathrm{k,d}}/E_{\mathrm{k,cm}}$ in comparison to We.

The comparison of prediction (6.28) with experimental data for MEK and tin is shown in Fig. 6.17. The breakup time t_b is rescaled by $E_{\mathrm{k,d}}/E_{\mathrm{k,cm}}$ according to the prediction (6.28) to allow a direct comparison of MEK and tin as their kinetic-energy partition $E_{\mathrm{k,d}}/E_{\mathrm{k,cm}}$ differs. We find a good agreement for the scaling with the Weber number over three decades for the combined data of MEK and tin. We also show in Fig. 6.17 the time of destabilization in the neck region of MEK sheets. Also here, the experimental data and the prediction (6.28) agree in terms of the scaling with the Weber number. The different prefactor between the neck and center region can be explained by the radial thickness profile $h(r,t)$: the neck region reaches the critical thickness h_{b} for a given Weber number at an earlier point in time compared to the center region. However, the kinematics of the neck and center region are described by the same scaling (6.10) and the development of the perturbation amplitude is assumed to be independent of the position on the sheet: a global Rayleigh–Taylor instability that is responsible for the breakup in the neck and center region alike. Consequently, the scaling exponent for the neck and center breakup are identical and in agreement with our prediction.

The prediction (6.29) for the characteristic wavenumber k_b explains the large Weber number We = 30 000 in Fig. 6.15 that was required to recover the random hole nucleation by unbiased statistics. A strong acceleration as set by the Weber number affects the mode selection such that the wavelength of the fastest growing mode at the end of the second phase is small enough to be sampled experimentally during the breakup in the third phase. As a consequence, the scaling for the wavenumber k_b cannot be validated experimentally for a sufficiently large range of Weber numbers. In both systems, it is a challegne to recover k_b in unbiased statistics unless extremley large Weber numbers are reached.

The initial perturbation amplitude η_0/R_0 is a property that is assumed to be

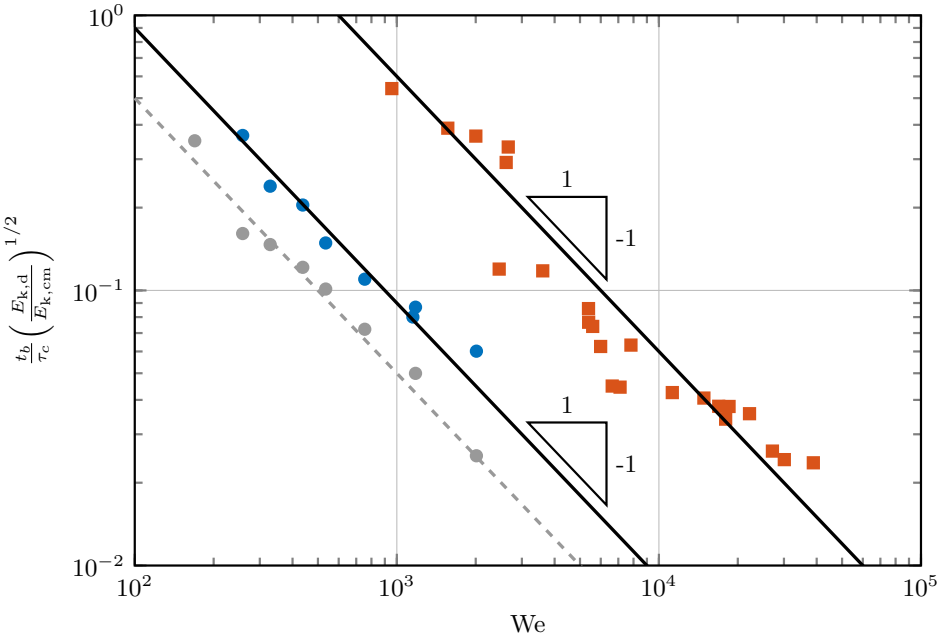

FIGURE 6.17: Breakup time t_b for MEK (blue circles) and tin drops (red squares) obtained for the sheet breakup in the center of the sheet. The experimental data points are obtained by finding the moment in time where the first hole in the center of a sheet $r/R \leq 0.5$ is observed. The solid black lines are the prediction (6.28) with $\eta_0/R_0 = 10^{-2}$ for MEK and $\eta_0/R_0 = 1.6 \times 10^{-3}$ for tin, both with a prefactor of 1. For MEK the corresponding data for the neck region is shown as gray circles, which follows the same scaling law with $\eta_0/R_0 = 10^{-2}$ and prefactor of 0.5 (dashed grey line).

characteristic to each liquid system and independent of the wavenumber k. It is therefore equivalent to a white noise with a constant amplitude that is present during the acceleration phase of our model. This initial noise explains the early sheet breakup for MEK in comparison to the tin system in our analysis: the amplitude of perturbations during the early-time acceleration phase affects the destabilization at later times in the same way as the Weber number. The two liquid systems apparently exhibit different noise levels, which will be part of our discussion in the next section.

6.9 Discussion & conclusion

We study the fragmentation of a free-falling liquid drop that is propelled by a laser-induced phase change. We consider two liquid systems that differ in their propulsion mechanism: vapor-driven drops of methy ethyl ketone (MEK) and plasma-driven tin drops. The fragmentation shows the same features in both systems and is a late-time consequence of the initial drop acceleration that ultimately leads to the destabilization of the deforming liquid body. The deformation is characterized by a change of topology from the spherical drop into a flat sheet on the inertia timescale and a surface-tension limited expansion into a thin sheet on the capillary timescale. We identify two accelerations that are orthogonal to each other in the flat-sheet limit and amplify perturbations by Rayleigh–Taylor instabilities on the deforming liquid body. First, the impulsive acceleration of the drop surface by virtue of the laser impact causes a destabilization of the thin sheet, which we referred to as *sheet breakup*. The second acceleration is caused by capillary restoring forces: a rim develops at the edge of the expanding sheet and is subject to a local acceleration in the same way as it was described for the mechanical impact of drop on a pillar [101]. We referred to this type of destabilization as *rim breakup*. As the drop deformation and fragmentation are ultimately the consequence of the very same laser impact we find a signature of the laser-matter interaction in the fluid-dynamic response.

The plasma dynamics affects the expansion of the liquid sheet by how the kinetic energy is transferred to the drop at its surface. We describe this effect by a power-law scaling for the partition of kinetic energy into translation and deformation energy in relation to the laser energy. Once included in the description of the sheet kinematics, the rim breakup in both systems is entirely described in terms of the Weber number and the kinetic-energy partition. We then obtain scaling laws for the characteristic time and wavenumber of the rim breakup, which we validate by experimental data. Capillary restoring forces also cause a Rayleigh–Plateau instability during the rim breakup. Our analysis predicts the timescale of the Rayleigh–Plateau and Rayleigh–Taylor instability to be decoupled from the late-time expansion of the sheet for large Weber numbers, which is confirmed by experimental observations.

The Rayleigh–Taylor instability that leads to the sheet breakup already starts to develop during the initial drop acceleration by the laser-matter interaction. Consistently, our analysis of the sheet breakup leads to a third parameter, beside the Weber number and energy partition, that is necessary to distinguish between the different driving mechanisms: the amplitude of perturbations η_0/R_0 that are present during the initial acceleration of the drop. We trace the amplitude of these perturbations from the early-time acceleration to the late-time deformation of the drop.The evolution of the instability is described by the dispersion relation characteristic of each of the following three phases: the impulsive acceleration in the

first phase is followed by an intermediate phase where the drop deforms into a flat sheet. Then follows a late-time phase where the expansion of the flat sheet into a thin sheet freezes any further development of the instability except for a self-similar stretching. We then obtain scaling laws for the characteristic time and wavenumber of the sheet breakup. The former is validated in both liquid systems by experimental data to find a good agreement between our model and the experiment.

We conclude from the time of sheet destabilization that the plasma-driven system exhibits an initial noise level of one order of magnitude lower than the vapor-driven system. The typical scale of $\eta_0/R_0 \sim 10^{-2}$ in the vapor-driven system excludes the thermal noise as source for initial perturbations, since the thermal noise was found to be several orders of magnitude smaller in comparable systems [126]. We therefore attribute the difference in η_0/R_0 between the two systems to a macroscopic noise that originates in the different laser-matter interaction at the drop surface. The sheet breakup is then caused by a global Rayleigh–Taylor instability that leads to a destabilization in areas where the perturbation amplitude is of the order of the local sheet thickness. In both systems, a radial dependency is introduced in the sheet thickness by virtue of the topology change from a spherical drop to a flat sheet. In addition, azimuthal modulations in the initial laser radiation for vapor-driven drops translate to deterministic variations in the sheet thickness during the late-time expansion. As a consequence, likely areas of destabilization emerge on the sheet in azimuthal and radial direction during the fragmentation. The hole nucleation itself is found to be a randomly distributed process when observed on a length much smaller than the extent of the deterministic thickness variations.

The analysis of the fluid-dynamic instabilities in combination with experimental data leads to a phase diagram for the onset of fragmentation by laser-pulse impact (Fig. 6.18). At low Weber number, only the rim breakup is observed while the sheet remains stable. In this regime, the initial acceleration is not strong enough to amplify the initial perturbation sufficiently for the sheet breakup to occur. For increasing Weber number the rim destabilizes at earlier times before the maximum expansion of the sheet is reached. The trajectory of fragments that originate from the rim breakup is set by the sheet expansion rate at the moment of detachment, which leads to a cloud of small drops surrounding the sheet at maximum expansion. The sheet breakup occurs at two distinct regions that are set by the radial thickness profile during the late-time expansion: the neck and the center region of the sheet. Both regions follow the same scaling law for the characteristic time of destabilization, which is the consequence of a global Rayleigh–Taylor instability that is responsible for the breakup in the neck and center region alike.

Both the rim and sheet breakup lead to a structure of elongated ligaments: in case of the rim breakup, the ligaments point radially outward, whereas the sheet

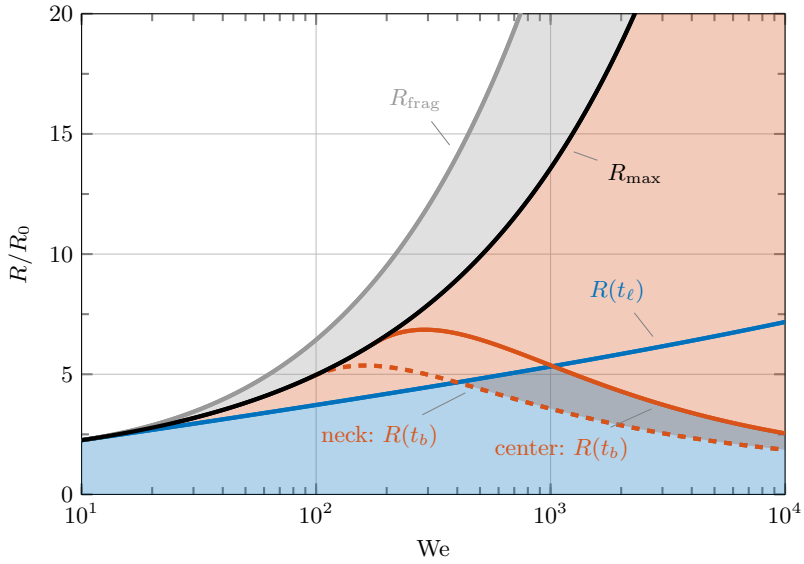

FIGURE 6.18: Overview on the stability of free-falling drops upon laser impact in terms of the Weber number and the radial expansion R/R_0. The parameter range of stable liquid sheets (blue area) is separated from the unstable domain (red area) by the rim breakup at $R(t_\ell)$ and the sheet breakup at $R(t_b)$. The diagram is based on the MEK system for which the energy partition $E_{\mathrm{k,d}}/E_{\mathrm{k,cm}} = 1.8$ and the initial perturbation amplitude $\eta_0/R_0 = 10^{-2}$ for the sheet breakup. The radii $R(t_\ell)$ and $R(t_b)$ follow then from the sheet kinematics (6.8) and the corresponding scaling (6.13) and (6.28) for the breakup time, where the sheet breakup $R(t_b)$ is given for the neck (dashed red line) and center region (solid red line). The prefactor in each scaling is obtained from the experimental data in Fig. 6.10 and Fig. 6.17, respectively. The maximum radius R_{max} (solid black line) follows from the sheet kinematics (6.8) for $t_{\mathrm{max}}/\tau_c = 2/\sqrt{27}$. At the same time, the radius R_{frag} (solid gray line) is an estimate for the extent of the cloud of fragments (gray area) that originate from the rim breakup. The fragment trajectory is assumed to be set by the expansion rate at the moment of destabilization, i.e. $R_{\mathrm{frag}} = R(t_\ell) + \dot{R}(t_\ell)(t_{\mathrm{max}} - t_\ell)$.

breakup leads to a two-dimensional web of ligaments. The parameter range where such a collection of ligaments is formed is marked as unstable domain (red area) in Fig. 6.18. The last stage of the drop fragmentation is then characterized by the breakup of individual ligaments into stable fragments. The collection of all resulting fragments, which finally relax to a spherical shape, leads then to the overall size distribution of stable drops. The elementary size distribution coming from a single ligament breakup depends on the roughness and the size of the ligament [101, 106,

127]. Depending on the history of a ligament, i.e. the way it was created before its breakup, the elementary distribution is then more or less broad. Experimental data for the elementary distribution after ligament breakup is best described by a gamma distribution [127]. The linear superposition of all elementary gamma distributions, one for each typical type of ligament, leads then to the overall size distribution of stable drops. The remaining problem is then to obtain the statistics for the typical ligaments that form in course of the rim and sheet breakup.

The final size distribution of the rim breakup for the mechanical impact of a drop an a pillar was successfully described by the linear combination of two elementary gamma distributions [101]. Each of the two distribution accounted for the breakup of a typical class of ligaments: one distribution for the radial ligaments and a second one for the remnant rim not completely converted into radial ligaments. As pointed out by [101] the experimental data for the size distribution was obtained under very symmetric impact conditions. In the current study, the high degree of symmetry observed in the tin system, especially the clear observation of the characteristic wavenumber k_ℓ, leads to the expectation that a bimodal distribution is sufficient as well to describe the rim breakup. In contrast to the tin system, the rim breakup in the MEK system is affected by the sheet breakup, which already limited the amount of data we could obtain for the rim breakup in that system. In turn, this interaction of the rim and the sheet may also require more than two elementary distributions to capture the rim breakup in the MEK system.

The statistics for the fragmentation of a web of ligaments has been described in detail by [106]. In this study, a planar Savart sheet is seeded with small air bubbles to cause a random hole piercing on the sheet. The growth and merging of holes in this experiment lead then to a web of ligaments, similar to the one observed in our study. The fragmentation of the ligament structure leads to a broad size distribution of fragments that was almost fully recovered by the elementary distribution for a single type of ligaments [106]. Since the ligaments are strongly corrugated by large-amplitude random capillary waves, even a single elementary distribution leads to a broad collection of drop sizes. Other contribution, e.g. drops originating from the nodes of the web of ligaments, lead then to a slightly broader final size distribution. A possible source of very small drops that was observed by [106] but lay outside the parameter domain is a secondary sheet formation due to the inertia of colliding rims: if the hole-opening speed is large the colliding rims do not merge but splash, forming a secondary sheet that is oriented orthogonal to the original one. We observe a similar process in our experiments, in particular for rims that originate from a hole nucleation in the neck region where the sheet is thinnest and the hole-opening speed the largest: the rims collide in an asymmetric fashion and form highly corrugated ligaments or even splash to first form a collection of thinner ligaments before they finally break into stable drops. The manifestation of such a

collection of ligaments can be seen in Fig. 6.19 for a single MEK sheet. We observe a variation in the typical size of ligaments by more than order of magnitude. Furthermore, the inset Fig. 6.19 (c) reveals the highly-corrugated cylindrical geometry of ligaments. We now recognize the necessity to consider more than one elementary size distribution to capture this broad size distribution already observed for the ligaments themselves.

Given the aforementioned considerations the final size distribution of the laser impact on a drop is expected to be broad distribution as a result of multiple elementary size distributions. The experimental investigation for both systems in terms of the size distribution is a challenge. On the one hand, the optical resolution of the shadowgraph images limits the range of fragment sizes that can be detected in the tin system. The small ligaments in Fig. 6.19 (c) for the MEK system suggest a typical size of $d_\ell/R_0 \sim 10^{-2}$, which is in absolute terms then a few hundred nanometer for the tin system, i.e. far below the resolution of optical imaging in the

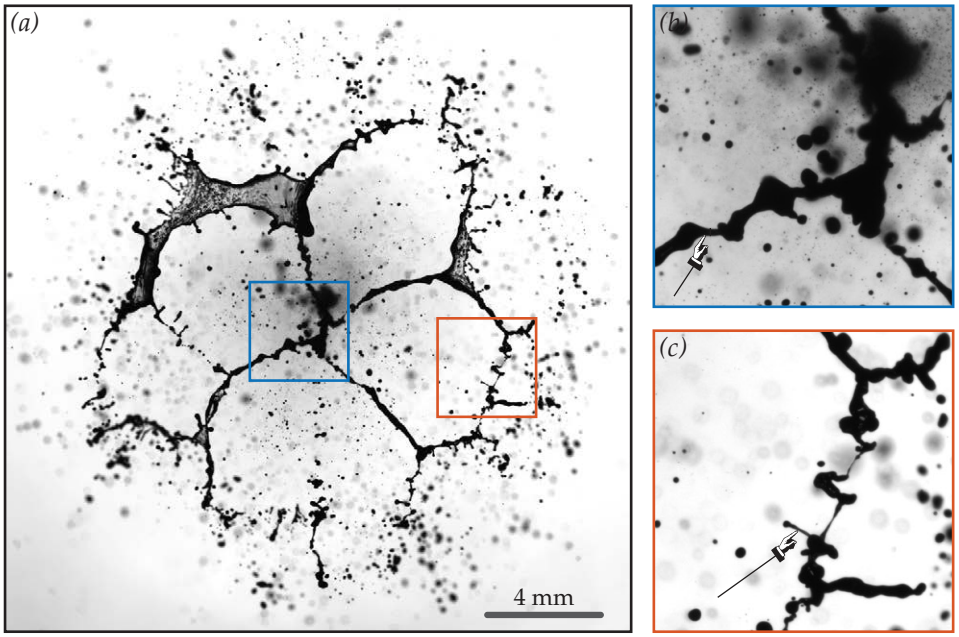

FIGURE 6.19: The web of ligaments for a MEK sheet at We = 750 in (a) and two magnified parts from the center (b) and neck region (c) of the sheet. The typical diameter of ligaments d_ℓ varies by more than one order of magnitude as indicated by the two pointers in (b, c) that mark ligaments with approximately $d_\ell = 100\,\mu\text{m}$ and $d_\ell = 4\,\mu\text{m}$.

visible spectrum. Measurement techniques based on light scattering seem to be a viable approach, but require suitable calibration particles to measure reliable size distributions, which are difficult to obtain for metals [128]. On the other hand, the MEK system shows large-scale facets that are set by the laser-beam profile (compare Fig. 6.14) and not of universal nature. These influences need to be incorporated in an statistical analysis in a transparent way to obtain a description that holds for both the tin and MEK system. Such an analysis clearly deserves further investigation, where the work presented here is the first step towards a full description of the drop fragmentation that incorporates the chaotic and deterministic facets of the ligaments formation.

Appendix: Rescaling the late-time sheet model

The impact of a drop with the velocity U and initial radius R_0 on a pillar of the same size leads to the development of a radial sheet of thickness $h(r,t)$ and radius $R(t)$ with dynamics [101]

$$\frac{R(t)-R_0}{R_0} = \sqrt{\tilde{\mathrm{We}}}\,\frac{t}{\tau_c}\left(1-\frac{\sqrt{3}}{2}\frac{t}{\tau_c}\right)^2, \tag{6.30}$$

$$h(r,t) \sim \frac{R_0^3}{Urt} = \frac{R_0^2\,\tau_c}{\sqrt{\tilde{\mathrm{We}}}\,rt}, \tag{6.31}$$

$$u_r(r,t) = \frac{r}{t}, \tag{6.32}$$

where u_r is the radial velocity inside the sheet. Here, the rescaled Weber number $\tilde{\mathrm{We}}$ accounts for different initial conditions during a laser impact in comparison to a mechanical impact on a pillar. In analogy to [21] we find $\tilde{\mathrm{We}}$ from a matching to the initial kinetic energy partition obtained from an early-time ($t \le \tau_e$) model of the drop, termed $\frac{E_{\mathrm{k,d}}}{E_{\mathrm{k,cm}}}$. Matching to the energy partition in terms of sheet model (6.30-6.32) then reads

$$\frac{E_{\mathrm{k,d}}}{E_{\mathrm{k,cm}}} = \frac{\int_0^R u_r^2\, hr\,\mathrm{d}r}{U^2\int_0^R hr\,\mathrm{d}r} = \frac{R^2}{3U^2t^2}, \tag{6.33}$$

where $E_{k,d}$ is the kinetic energy associated with the deformation (expansion) of the sheet and $E_{k,cm}$ with the kinetic energy of the centre-mass-motion. For $t \ll \tau_c$ and $\mathrm{We_d} \gg 1$ we approximate (6.30) by $R \approx R_0\sqrt{\tilde{\mathrm{We}}}\,t/\tau_c$ such that by using that $U^2 = \mathrm{We}\,R_0^2/\tau_c^2$ we find

$$\tilde{\mathrm{We}} = 3\,\mathrm{We}\frac{E_{\mathrm{k,d}}}{E_{\mathrm{k,cm}}} = 3\,\mathrm{We_d}, \tag{6.34}$$

with $\mathrm{We_d}$ as defined in (6.7). This results explains our rescaling in (6.8). The energy partition for the flat-top beam profile used in the MEK system is obtained analytically from the early-time model as $E_{\mathrm{k,d}}/E_{\mathrm{k,cm}} \approx 1.8$ [21].

Chapter 7

Expansion dynamics after laser-induced cavitation in liquid tin microdroplets

D. Kurilovich, T. de F. Pinto, F. Torretti, R. Schupp, J. Scheers, A. S. Stodolna, H. Gelderblom, K. S. E. Eikema, S. Witte, W. Ubachs, R. Hoekstra, and O. O. Versolato, Phys. Rev. Appl. **10**, 054005 (2018).

The cavitation-driven expansion dynamics of liquid tin microdroplets is investigated, set in motion by the ablative impact of a 15-ps laser pulse. We combine high-resolution stroboscopic shadowgraphy with an intuitive fluid dynamic model that includes the onset of fragmentation, and find good agreement between model and experimental data for two different droplet sizes over a wide range of laser pulse energies. The dependence of the initial expansion velocity on these experimental parameters is heuristically captured in a single power law. Further, the obtained late-time mass distributions are shown to be governed by a single parameter. These studies are performed under conditions relevant for plasma light sources for extreme-ultraviolet nanolithography.

7.1 Introduction

Intense, short-pulse laser radiation can produce strong shock waves in liquids leading in some spectacular cases to explosive cavitation and violent spallation of the material [24–26, 129, 130]. Such dramatic physical phenomena can readily find application, a very recent example of which is found in the field of nanolithography where microdroplets of liquid tin are used to create extreme ultraviolet (EUV) light [13, 18, 131]. These tin droplets, typically several 10 μm in diameter, serve as targets for a high-energy, ns-pulse laser, creating a laser-produced plasma (LPP). Line emission from highly charged tin ions in the LPP provides the required EUV light. Currently, a dual-laser-pulse sequence is employed [18]. In a first step, a ns-laser prepulse is used to carefully shape the droplet into a thin sheet that is considered to be advantageous for EUV production with a second, much more energetic, main pulse. Recent developments [17, 18], however, produced tentative but tantalizing evidence for significantly improved source performance when replacing the ns-prepulse with a ps-prepulse laser to produce a shock-wave-induced explosive fragmentation. Although some notable progress was made very recently [24–27], this process requires further investigation.

This paper advances the understanding of the aforementioned systems by providing an experimental and theoretical study of the late-time dynamics of the deformation of free-falling tin microdroplets. Being initially spherical, the droplets are subjected by strong shock waves generated by ps laser pulse impact, giving rise to cavitation [24–27]. This centralized cavitation explosively propels the liquid to very high ($\sim$100 m/s) radial velocities, producing a rapidly thinning liquid-tin shell (see Fig. 7.1). The initial spherical symmetry of the system is broken when the intensity of the shock wave exceeds a certain threshold and dramatic spallation is observed on the side of the droplet facing away from the laser impact zone. We focus our studies on the rich physics of the dynamics set in motion by the central cavitation.

We develop a model description for the time evolution of a stretching spherical shell, including the onset of fragmentation. Using stroboscopic shadowgraphic imaging, this model is experimentally validated over a wide range of laser pulse energies, 15 ps in duration, and for two droplet sizes. The dependence of the initial expansion velocity on these experimental parameters is heuristically captured in a single power law. The late-time mass distributions, experimentally obtained from front-view shadowgraphy, are furthermore shown to be governed by a single parameter.

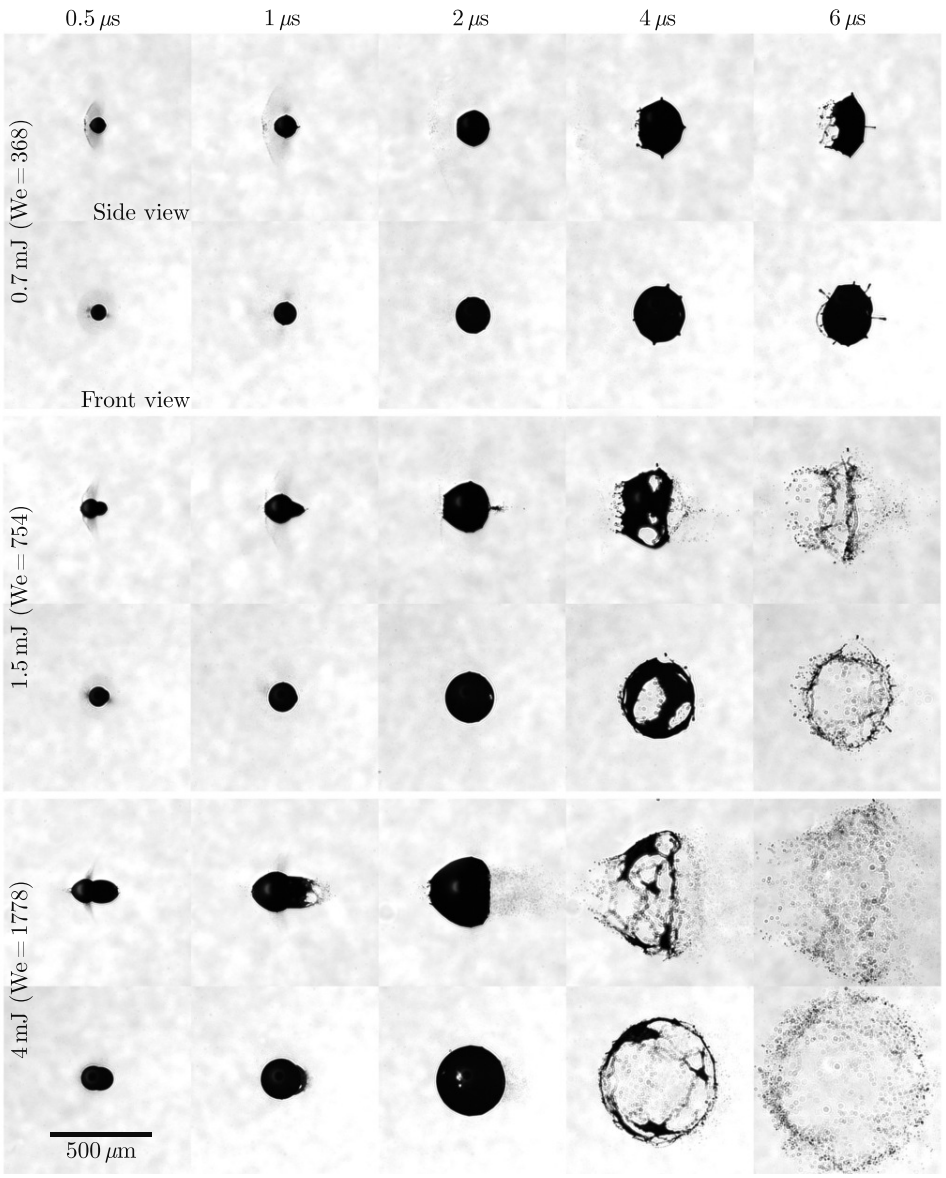

FIGURE 7.1: Stroboscopic shadowgraph images of expanding tin microdroplets (23 μm initial radius) taken at different time delays for three different laser pulse energies (or Weber numbers, see Sec. 7.3.1) at a pulse length of 15 ps, as seen from two viewing angles (90° side view and 30° front view). Laser impacts from the left; images are cropped and centered individually to improve visibility. A 500-μm-length scale bar is provided in the left-lower corner.

7.2 Experimental methods

Our experimental setup has previously been described in detail [20]. For clarity, the most important characteristics, as well as experimental upgrades, are discussed here. A droplet generator is operated in a vacuum chamber (10^{-7} mbar) and held at constant temperature of 260° C, well above the melting point of tin. The nozzle produces an on-axis multi-kHz train of 15 or 23 μm radius droplets of 99.995% purity tin, with density $\rho = 7\,\mathrm{g/cm^3}$ and surface tension $\sigma = 0.532\,\mathrm{N/m}$. The droplets relax to a spherical shape before they pass through a horizontal light sheet produced from a helium-neon laser. The light scattered by the droplets is detected by a photomultiplier tube, whose signal is reduced in frequency to 10 Hz to trigger a Nd:YAG laser system. This laser system produces tunable ps pulses of 1064 nm wavelength light as described in more detail in Ref. [37]. The laser pulse energy is varied between 0.5 and 5 mJ employing a suitable combination of a waveplate and polarizer; the pulse length is kept constant at approximately 15 ps for the experiments described here. The laser beam is focused down to a 100 μm full-width-at-half-maximum (FWHM) diameter Gaussian spot. To maintain cylindrical symmetry, the laser light has circular polarization. An accurately timed laser pulse provides a radially-centered interaction with a falling droplet that occurs in a reproducible manner. Only a small fraction of the droplets interact with a laser pulse due to the mismatch in repetition rates of the droplet generator (multi-kHz) and laser (10 Hz).

Two shadowgraph imaging systems capture the dynamics of the expanding droplets. These systems are based on a single pulse from a broadband 560±2 nm wavelength 5-ns-pulse dye laser. Combined with two long-distance microscopes coupled with CCD cameras, this laser source provides back-lighting that is carefully rendered incoherent both temporally and spatially, with a 4 μm resolution. One of these microscopes is aligned orthogonally to the laser beam to obtain side-view images; the other one is at 30° angle to the beam direction for a (tilted) front view. Both microscopes are equipped with bandpass filters to suppress the plasma radiation. The images obtained are used to track the size, shape, and velocity of the droplet expansion employing an image-processing algorithm. Stroboscopic time series of different droplets are constructed by triggering the shadowgraphy systems once per drive laser shot with increasing delay, typically with time steps of 50–100 ns [132].

7.3 Results and interpretation

The response of a tin droplet to laser pulse impact is shown in Fig. 7.1 for three laser pulse energies. A qualitative description of the relevant physical processes leading to cavitation and spallation was recently given in Ref. [25]. We summarize the crucial steps in the following, combining it with our experimental observations. The laser-pulse impact ablates a thin (less than 1 μm) layer of tin. At the lower pulse energies (see the 0.7 or 1.5 mJ cases presented in Fig. 7.1), this ablated mass is clearly visible and seen to move away from the droplet in the direction opposite to the laser light. The remarkably sharp outer boundary of this ablated mass may be explained by the existence of an inhomogeneous two-phase, gas-liquid mixture of low average density but approaching liquid density in the vicinity of the ablation front [133, 134].

The ablation pulse gives rise to a pressure wave starting from the laser-impacted region of the droplet. This pressure is applied on a short, picosecond time scale that is several orders of magnitude shorter than the time scale on which pressure waves travel through the droplet.

As a consequence, the liquid is locally compressed and pressure waves travel through the droplet [116]. Converging pressure "shock" waves superimpose in the center of the droplet where they cause tensile stress. Once this tensile stress is above the yield strength of the liquid it ruptures and a thin shell is formed. Theoretical modeling [25] has shown that there is a high sensitivity of both the rate of expansion and the morphology of the deformed droplet to the details of the, poorly known, metastable equation-of-state (EOS) of tin in the region of the liquid-vapor phase transition and to the parameters of the critical point. Thus, precise theory predictions of the post-cavitation dynamics of liquid tin microdroplets cannot yet be made and, instead, measurements as presented in this work may provide a sensitive instrument for probing the EOS of liquid metals [25].

After passing through the droplet center, the shock wave reaches the back side of the droplet (i.e. the side facing away from the laser) and is reflected from this free interface, where it can again rupture the liquid and give rise to spallation that rapidly propels, at several hundred meters per second, a small mass fraction of the droplet along the laser beam propagation direction (see Fig. 7.1) [25, 26]. The fluid-dynamic description of this spallation is very rich and will be left for future work. However, it is noteworthy that there is a regime where a strong spallation occurs, but is mitigated under capillary action (compare the $t = 1$ and 2 μs shadowgraphs for the 1.5 mJ case in Fig. 7.1).

The higher-energy cases in Fig. 7.1 also hint at the existence of a hole on the side of the droplet facing the laser, which may possibly be attributed to ablation-thinning of the droplet shell. In combination with the spallation, a "tunnel" is thus created (see the front view shadowgraphs in Fig. 7.1), and may later form a

doughnut-type mass distribution. Another scenario, when fragmentation following the collapse of the shell results in high-speed jetting, corresponding to the lowest laser pulse energies, is reported on in Refs. [27, 112, 135].

In the following, we focus on the late-time dynamics set in motion by the central cavitation. Firstly, a basic model for the time evolution of the intact liquid shell is presented. Secondly, we study the time scale at which first holes close to the equator of this shell become visible, after which full fragmentation of the shell rapidly sets in. This results, eventually, in a late-time mass distribution, the understanding of which is of particular relevance for producing EUV radiation at high conversion efficiencies.

7.3.1 Time evolution of the shell

The shadowgraphs such as those presented in Fig. 7.1 clearly show a cylindrically symmetric expanding shell, the radius $R(t)$ of which is tracked for each time step by measuring the maximal transverse (vertical in Fig. 7.1) size of this feature from the side-view shadowgraphs. By fitting a linear function to the first few $R(t)$ data points after the laser impact, we obtain values for the initial droplet expansion velocity $\dot{R}(t{=}0)$. Figure 7.2(a) shows a monotonic increase of this radial expansion velocity $\dot{R}(t{=}0)$ as a function of laser pulse energy. Using a heuristic argument, we collapse all obtained data onto a single curve, scaling the obtained velocities with the initial droplet radius R_0 (see Fig. 7.2(b)). To arrive at this scaling, we hypothesize that the magnitude of the induced shock wave, and its related cavitation event, scales with the laser-facing surface area, $\propto R_0^2$ (the droplet is much smaller than the laser spot size). Meanwhile, the expansion is impeded by the droplet mass $\propto R_0^{-3}$. By ignoring the possible differences in the dissipation of the shock wave, one thus arrives at the aforementioned simple scaling $\dot{R}(t{=}0) \propto R_0^{-1}$. Ablation-induced momentum exerted on the droplet, leading to propulsion, is expected also to scale with absorbed energy, again as $\propto R_0^2$ [20, 22], counteracted by the droplet mass as $\propto R_0^3$, leading to an identical scaling law. However, in contrast to the ns laser pulse impact studied in those works [20, 22], the resulting droplet propulsion is limited here. As seen from Fig. 7.2(b), such a rescaling causes all data to fall on a single curve that appears to be represented quite well by a power-law function $\dot{R}(t{=}0)R_0 = A \times E^{\alpha}$ with fit parameters $A = 9.4{\pm}1.4\,\mathrm{m}^2/\mathrm{s}$ and $\alpha = 0.46{\pm}0.02$. Although such power-law behavior is well established in the relevant literature on ablation [91, 93, 136], these fit parameters cannot be straightforwardly predicted from available theory, given their sensitivity to the EOS and the details of laser-matter interaction.

To describe the time evolution of the liquid droplets in Fig. 7.1, we hypothesize that a small (micrometer-sized), high-pressure (kilobar-level) cavitation bubble expands the liquid quickly into a thin shell. Thus, a spherically symmetric shell expands at a certain initial velocity $\dot{R}(t{=}0)$, with the cavitation pressure having done

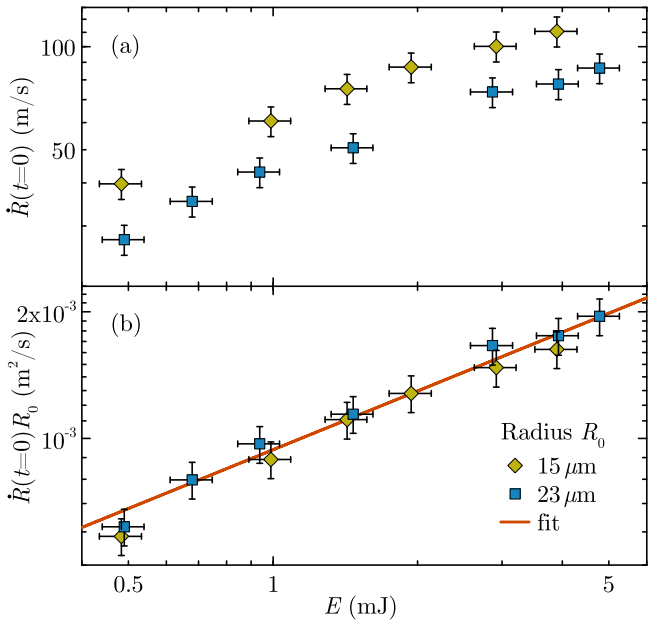

FIGURE 7.2: (a) Initial radial expansion velocity $\dot{R}(t{=}0)$ of tin microdroplets as a function of total laser pulse energy E. Yellow diamonds are for $R_0 = 15\,\mu$m and blue squares are for $R_0 = 23\,\mu$m. The error bars represent 10% uncertainty on the velocity measurements and 20% uncertainty on the energy measurements. (b) The same data, rescaled by multiplying by the initial droplet radius R_0. The solid red line is obtained by fitting a power-law function to the concatenated data.

its thermodynamic work effectively at time zero. Given that the droplet expands into the vacuum, the only limitation to its expansion is surface tension.

The liquid tin shell has thickness $h(t)$ which decreases quadratically with time as mass conservation implies, in the limit of a thin shell ($R(t) \gg h(t)$), that $h(t) = R_0^3/(3R(t)^2) \approx R_0^3/(3t^2\dot{R}(t{=}0)^2)$. The expansion of the shell can be described by the Rayleigh-Plesset equation, which in the limit of a thin shell reads [137]: $p(R-h)-p(R) \approx \rho h\ddot{R}$, where p is pressure. Imposing dynamic boundary conditions at the two liquid-vapor interfaces $p(R-h)$ and $p(R)$, and noting that the only force acting on the shell is the Laplace pressure, the net value of which is given by $p = 4\sigma/R(t)$ (in contrast to Ref. [137], where this contribution was negligible), we find

$$\ddot{R}(t) = \frac{-p}{\rho h(t)} = -\frac{4\sigma}{\rho h(t) R(t)} = -\frac{12\sigma R(t)}{\rho R_0^3}. \tag{7.1}$$

From the above expression, using the boundary conditions of a given $\dot{R}(t{=}0)$ and initial radius R_0, we obtain

$$\frac{R(t)}{R_0} = \cos(\pi t/\tau_c) + \sqrt{\frac{\mathrm{We}}{12}}\sin(\pi t/\tau_c), \tag{7.2}$$

introducing the capillary time scale here as $\tau_c = \pi\sqrt{\rho R_0^3/12\sigma}$ and the relevant Weber number as $\mathrm{We} = \rho R_0 \dot{R}(t{=}0)^2/\sigma$. The above solution is identical in form to that obtained previously for a disk-type expansion of a droplet following ns-laser pulse impact [20, 21].

Next, we apply the theory developed above with zero fit parameters taking as an input the experimental values for $\dot{R}(t{=}0)$. The results are presented in Fig. 7.3(b), where the experimentally obtained radius $R(t)$ (see Fig. 7.3(a)) is rendered dimensionless by dividing by R_0 (and subtraction of the unity value offset), and plotted as a function of dimensionless time t/τ_c. For $R_0 = 15$ the capillary time is $\approx 6\,\mu$s, for $R_0 = 23\,\mu$m it is $\approx 11\,\mu$s. Given the simplicity of our arguments, we find excellent agreement between model and experiment. The observed late-time "overshoot" that is apparent in the experimental data shown, with theory predicting a more rapid retraction of the shell, can be understood by considering the process of hole formation and ensuing fragmentation, which strongly reduces the restoring forces.

7.3.2 Hole opening time

The expanding shell is subjected to Rayleigh-Taylor instabilities (RTI), here as instabilities of the liquid-vapor interface driven by the radial acceleration and deceleration of the liquid sheet [137]. Surface tension provides mode selection of the

FIGURE 7.3: (Figure is found on the following page.) (a) Radius $R(t)$ of shell driven by cavitation in $R_0 = 15\,\mu$m droplets (open symbols) and $R_0 = 23\,\mu$m droplets (colored symbols) for similar Weber numbers. Open squares, We = 304; black squares, We = 368; open circles, We = 705; brown circles, We = 754; open triangles, We = 1923; green triangles, We = 1778. The inset ($500 \times 700\,\mu\mathrm{m}^2$) represents a side-view image of the We = 754 case at $2.5\,\mu$s. (b) Rescaled, dimensionless radius as a function of dimensionless time t/τ_c. The solid curves represent the model predictions (see Eq. (2)) for the $23\,\mu$m initial radius droplet; the dashed curves show the same but for the smaller, $15\,\mu$m droplet. The solid gray line depicts the destabilization radius $R(t_*)$ as obtained from the fit of Eq. (7.3) to the data (see Fig. 7.4), applied to Eq. (7.2). The data are grayed out beyond this line. (c) Sequence of side-view shadowgraphy images taken from Fig. 7.1 for We = 368 and We = 1778, for $R_0 = 23\,\mu$m droplets, with indication of the corresponding dimensionless time t/τ_c.

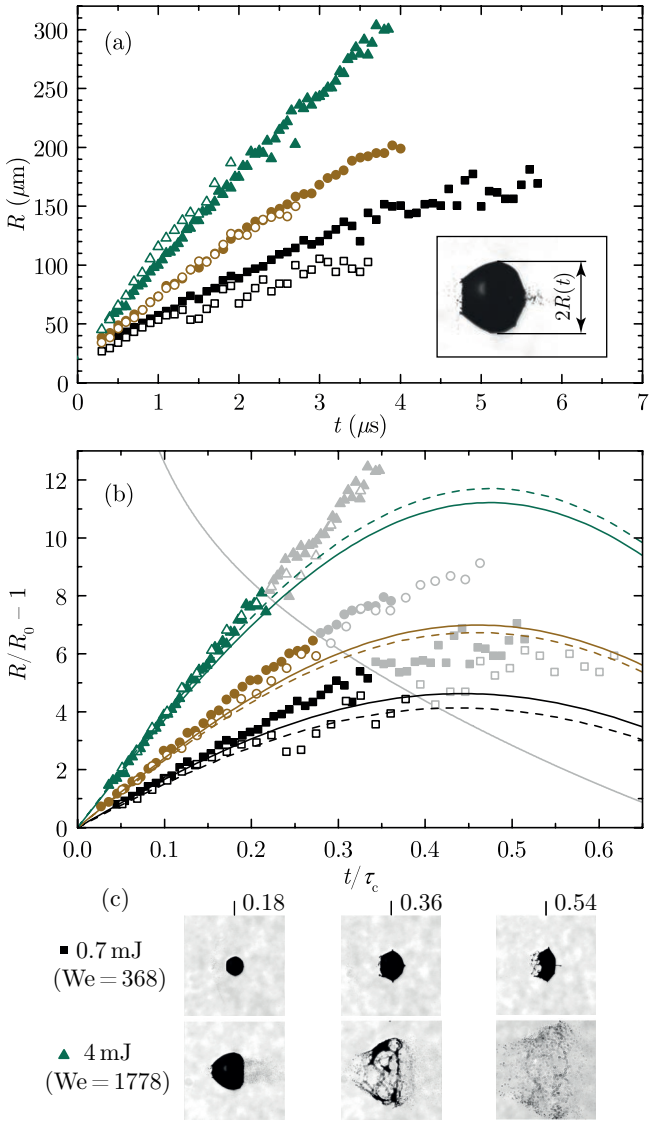

FIGURE 7.3: (Continued from the previous page.)

RTI [102, 125, 137, 138]. This phenomenon will lead to hole formation after which rapid hole opening and merging will lead to full fragmentation of the shell. In our system, there are two acceleration mechanisms that act along the surface normal and that thus will contribute to RTI growth. Firstly, the liquid is strongly accelerated by the cavitation pressure. Secondly, after the initial fast expansion, the shell much more slowly decelerates under the influence of surface tension. Holes will form at the shell piercing time t_*, when the size of a growing instability is of the order of the shell thickness [137]. In the available literature (e.g., see Refs. [102, 137]), quite generally a scaling relation is found of the type

$$\frac{t_*}{\tau_c} \propto \mathrm{We}^{-\beta}, \tag{7.3}$$

resulting in a rough scaling for the corresponding destabilization radius [137]

$$\frac{R(t_*)}{R_0} - 1 \propto \mathrm{We}^{1/2-\beta}. \tag{7.4}$$

Here we have, for simplicity, linearized the expansion rate to a constant $\dot{R} \propto \mathrm{We}^{1/2}$ and in Eq. (7.3) dropped the usual weak scaling term $(\eta_0/R_0)^\beta$, where η_0 is the initial amplitude of RTI. The positive power β is typically smaller than unity [102, 137, 139]. Obtaining a theoretical value for this power is complicated because of the two competing mechanisms driving RTI. We take instead the rather general form of Eq. (7.3) and let the experiment provide the relevant value for β and for the proportionality constant. In the experiments, a hole close to the equator of the shell becomes clearly visible in side view shadowgraphy only when another hole simultaneously appears on the opposite side. This naturally introduces a slight detection bias. However, it is possible to reliably and reproducibly obtain an estimate for t_* based on optical inspection of the experimental data supported by the fact that for times $t > t_*$ (where we take 100 ns time steps) the shell becomes permeated with holes. We observe a monotonically decreasing value for t_* with increasing Weber number as expected from Eq. (7.3). Furthermore, the absolute time of breakup t_* is seen to decrease with droplet size for similar Weber number.

Rescaling $t_* \to t_*/\tau_c$ in Fig. 7.4 indeed collapses the data for the two different droplet sizes onto a single curve. The resulting fit values of the power law Eq. (7.3) are given by $\beta = 0.34(4)$ and 3.0(8) for the proportionality constant. The apparent similarity of the hole opening times for the larger droplet for $\mathrm{We} > 1500$ should be considered to be purely coincidental, linked to the finite accuracy of the optical inspection method of a selected data set with limited temporal resolution. As we clearly find $\beta < 1/2$ we can now immediately conclude from Eq. (7.4) that the destabilization radius $R(t_*)$ increases with Weber number, and thus with laser energy. The fit values obtained will serve as input for predicting the late-time mass distribution produced by the laser impact.

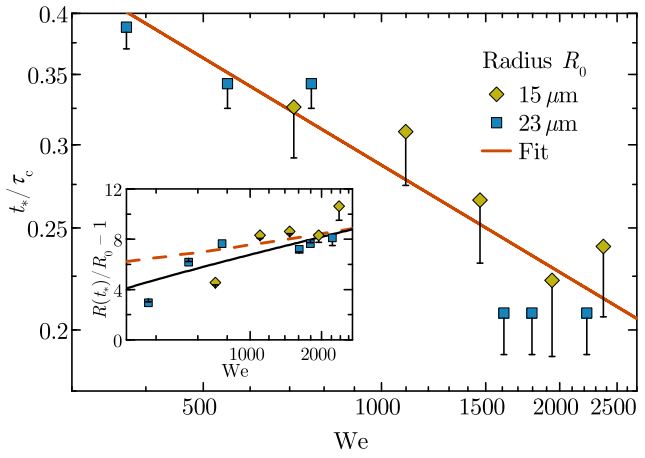

FIGURE 7.4: Dimensionless time of first hole opening t_*/τ_c as a function of Weber number for two droplet sizes: 15 μm (yellow diamonds) and 23 μm initial radius (blue squares). For We $\lesssim 300$, the shell collapsed before holes were apparent. Error bars are two time steps towards shorter values. The solid red line represents the best fit of a power law to the concatenated data. The inset graph depicts the dimensionless radius of the shell at the moment of hole opening. The solid black line shows the destabilization radius as obtained from inserting Eq. (7.3) into Eq.(7.2). The dashed red line is based on Eq. (7.4) taking $\beta = 0.34$ (see the main text).

7.3.3 Late-time mass distribution

Having achieved good agreement between experiment and model, we now summarize our findings in Fig. 7.5 to facilitate a more direct, industrial application of our findings. The maximum amplitude of an intact retracting shell is given by maximizing Eq. (2). The resulting dashed black curve in Fig. 7.5 is close to the well-known scaling $\sim\sqrt{\text{We}}$ (as was pointed out in Ref. [31]). The maximum attainable shell size without any holes (i.e. the destabilization radius) is obtained by inserting Eq. (7.3) into Eq. (7.2) as in Fig. 7.3. The result is shown as a solid black line in Fig. 7.5. Once this line is crossed in the expansion phase, the rapid breakup and fragmentation of the shell, associated with large Weber numbers here, precludes capillary collapse and the droplet target fragments ballistically expand. For the low Weber numbers shown the shell collapses and jetting may ensue [27].

In Fig. 7.5 we have also indicated ranges of Weber numbers that we associate with different spallation regimes. For Weber numbers below We ≈ 500, no spallation is visible at all; for $500 \lesssim \text{We} \lesssim 1000$ the spall is nearly fully retracted due to surface tension; and for We $\gtrsim 1000$ there is a rather abrupt and violent breakout of the spall.

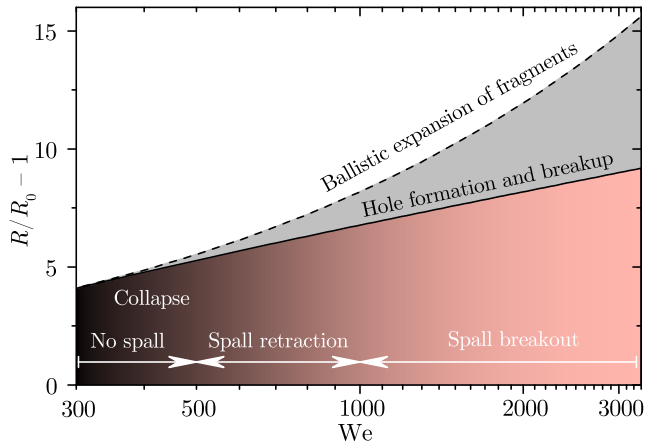

FIGURE 7.5: Phase diagram depicting the maximum obtainable radius as a function of Weber number. White arrows illustrate the various spallation regimes (see main text). The dashed line is obtained by maximizing Eq. (7.2). The solid line shows the destabilization radius as obtained from inserting Eq. (7.3) into Eq. (7.2); the area under this line is obtainable without holes occurring.

For $\mathrm{We} \gtrsim 1000$, we find that hole formation in the "tunnel" wall leads very quickly to complete breakup of the shell, where the fragments continue on their ballistic trajectories with radial velocities close to the initial $\dot{R}(t{=}0)$.

From an application perspective, it is interesting to study the "final" late-time fragment mass distribution that might serve as a target for a main laser pulse in an actual industrial EUV-source based on tin plasma. In the following analysis, we present some brief guidelines based on the here presented data but keep the full analysis of the relevant fragmentation process (including fragment size distributions) for later, dedicated work. We find that the final mass distribution changes very dramatically over a relatively small range of Weber numbers as can be seen from the shadowgraphs presented in Fig. 7.6(a) as well as from their angularly averaged, radial projections shown in Fig. 7.6(b). These projections can loosely be interpreted as a column-density mass distribution along the line-of-sight of the backlight illumination. The projections are not corrected for the small parallax angle or for the limited depth of focus. Still, we expect to track a large fraction of the total droplet mass. Similar mass distributions are found for 15 and 23 μm droplets at comparable Weber numbers (see Fig. 7.6).

For $\mathrm{We} = 544$ we observe that the mass distribution has a maximum in the center of the image, as is to be expected from a collapse. For just very slightly

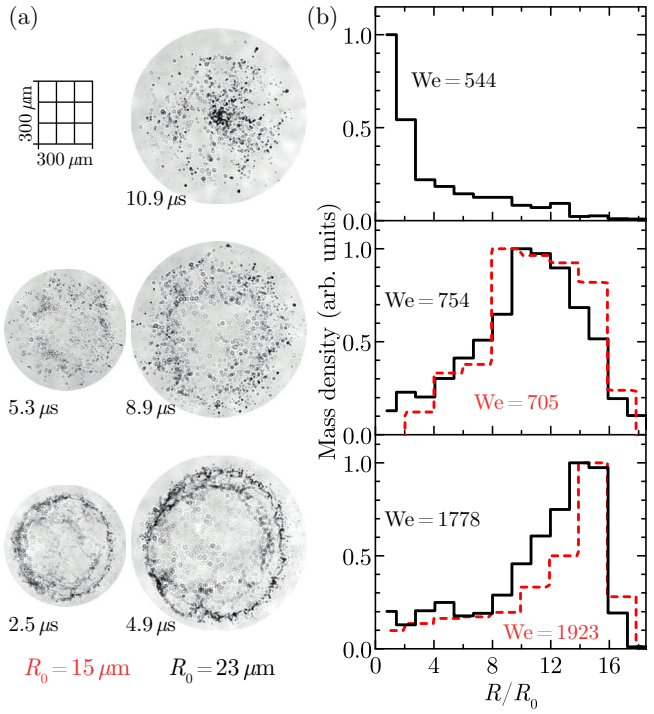

FIGURE 7.6: (a) Late-time front-view (30°) shadowgraphs of expanded and deformed droplets of different droplet sizes representing cases of similar Weber numbers. The rectangular scale grid in the top-left corner visualizes the effect of the 30° parallax angle. (b) Inverted, angularly averaged, radial projections of the obtained gray scale of corresponding images from (a), which gives a qualitative measure of the radial column-density-mass distribution. The dashed red line corresponds to the data from $R_0 = 15\,\mu$m droplets; the solid black line is for $R_0 = 23\,\mu$m.

larger Weber numbers, we find instead a toroidal profile that becomes more and more pronounced for larger Weber numbers. We attribute this observation to the RTI-driven breakup of the "tunnel" wall (thus preventing collapse) as well as by a pronounced spallation that modifies the mass distribution, as was also noted in Ref. [25].

The sensitivity of the final state mass distribution to the Weber number established and quantified here can readily find application. As an example, we note that a typical target size used in the industry is in the order of a few hundred micrometers [18], several microseconds after prepulse impact. In our experiments,

a relevant $\sim$450 μm diameter target is, for example, obtained from a $R_0 = 15\,\mu$m initial droplet size after expanding for 2.5 μs, see Fig. 7.6(a) for We = 1923. In this case, the main pulse would not find a significant mass fraction in its focus. Thus, it may well be opportune to choose a lower Weber number, by tuning down the laser energy, and obtain a more homogeneous mass distribution which could improve the conversion efficiency of drive laser light into useful EUV radiation by, e.g., increasing the absorption of drive-laser light.

7.4 Conclusions

We present an analysis of the cavitation-driven expansion dynamics of liquid tin microdroplets that is set in motion by the ablative impact of a 15-ps laser pulse. High-resolution stroboscopic shadowgraphy of the expanding tin shells is combined with an intuitive fluid dynamic model that includes the time and size at which the onset of fragmentation becomes apparent. This model will aid follow-up studies of the fragmentation pathways. Good agreement between model and experimental data is found for two different droplet sizes over a wide range of laser pulse energies. The dependence of the initial expansion velocity of the liquid shell on these experimental parameters is heuristically captured, for application purposes, in a single power law. A summary phase diagram of the expansion dynamics is presented. It covers regimes with and without spallation, as well as a transition regime where the spalled material is retracted under surface tension. This transition regime enables finding conditions for a maximum shell expansion velocity with strongly suppressed forward-moving debris. This phase diagram facilitates a more direct, industrial application of our findings.

Further, the experimentally obtained late-time mass distributions are shown to be governed by a single parameter, the Weber number. These studies are of particular relevance for plasma sources of extreme ultraviolet light for nanolithography. In such plasma sources, the tin mass distributions obtained upon cavitation-driven shell fragmentation, as studied in this work, are shown to be promising targets for efficient laser coupling [17, 18].

Bibliography

[1]G. E. Moore, "Cramming more components onto integrated circuits", Proc. IEEE **86**, 82–85 (1998).

[2]G. E. Moore, "Progress in digital integrated electronics", Proc. IEDM Tech. Dig., 11–13 (1975).

[3]M. M. Waldrop, "The chips are down for Moore's law", Nature **530**, 144–147 (2016).

[4]*International Technology Roadmap for Semiconductors*, `http://www.itrs2.net/`.

[5]C. A. Mack, "Fifty Years of Moore's Law", IEEE Trans. Semicond. Manuf. **24**, 202–207 (2011).

[6]G. E. Moore, "Lithography and the future of Moore's law", Proc. SPIE **2439**, 2439 –2439 –16 (1995).

[7]J. van Schoot, K. Troost, F. Bornebroek, R. van Ballegoij, S. Lok, P. Krabbendam, J. Stoeldraijer, J. Benschop, J. Finders, H. Meiling, E. van Setten, B. Kneer, P. Kuerz, W. Kaiser, T. Heil, and S. Migura, "The future of EUV lithography: continuing Moore's Law into the next decade", Proc. SPIE **10583** (2018).

[8]R. F. Pease and S. Y. Chou, "Lithography and Other Patterning Techniques for Future Electronics", Proc. IEEE **96**, 248–270 (2008).

[9]A. J. den Boef, "Optical wafer metrology sensors for process-robust CD and overlay control in semiconductor device manufacturing", Surf. Topogr. **4**, 023001 (2016).

[10]C. Wagner and N. Harned, "Lithography gets extreme", Nat. Photonics **4**, 24–26 (2010).

[11]V. Bakshi, ed., *EUV Lithography*, 2nd Edition (SPIE Press, 2018).

[12]M. Purvis, I. V. Fomenkov, A. A. Schafgans, M. Vargas, S. Rich, Y. Tao, S. I. Rokitski, M. Mulder, E. Buurman, M. Kats, J. Stewart, A. D. LaForge, C. Rajyaguru, G. Vaschenko, A. I. Ershov, R. J. Rafac, M. Abraham, D. C. Brandt, and D. J. Brown, "Industrialization of a robust EUV source for high-volume manufacturing and power scaling beyond 250W", Proc. SPIE **10583**, 10583 (2018).

[13]V. Y. Banine, K. N. Koshelev, and G. H. P. M. Swinkels, "Physical processes in EUV sources for microlithography", J. Phys. D **44**, 253001 (2011).

[14]A. Z. Giovannini, N. Gambino, B. Rollinger, and R. S. Abhari, "Angular ion species distribution in droplet-based laser-produced plasmas", J. Appl. Phys. **117**, 033302 (2015).

[15]M. J. Deuzeman, A. S. Stodolna, E. E. B. Leerssen, A. Antoncecchi, N. Spook, T. Kleijntjens, J. Versluis, S. Witte, K. S. E. Eikema, W. Ubachs, R. Hoekstra, and O. O. Versolato, "Ion distribution and ablation depth measurements of a fs-ps laser-irradiated solid tin target", J. Appl. Phys. **121**, 103301 (2017).

[16]A. Bayerle, M. J. Deuzeman, S van der Heijden, D. Kurilovich, T. de Faria Pinto, A. Stodolna, S. Witte, K. S. E. Eikema, W. Ubachs, R. Hoekstra, and O. O. Versolato, "Sn ion energy distributions of ns- and ps-laser produced plasmas", Plasma Sources Sci. Technol. **27**, 045001 (2018).

[17]Y. Kawasuji, K. M. Nowak, T. Hori, T. Okamoto, H. Tanaka, Y. Watanabe, T. Abe, T. Kodama, H. Nakarai, T. Yamazaki, S. Okazaki, T. Saitou, H. Mizoguchi, and Y. Shiraishi, "Key components technology update of the 250 W high-power LPP-EUV light source", Proc. SPIE **10143**, 101432G (2017).

[18]I. Fomenkov, D. Brandt, A. Ershov, A. Schafgans, Y. Tao, G. Vaschenko, S. Rokitski, M. Kats, M. Vargas, M. Purvis, R. Rafac, B. La Fontaine, S. De Dea, A. LaForge, J. Stewart, S. Chang, M. Graham, D. Riggs, T. Taylor, M. Abraham, and D. Brown, "Light sources for high-volume manufacturing EUV lithography: technology, performance, and power scaling", Adv. Opt. Technol. **6**, 173–186 (2017).

[19]V. Bakshi, ed., *EUV Sources for Lithography*, SPIE Press monograph (SPIE Press, 2006).

[20]D. Kurilovich, A. L. Klein, F. Torretti, A. Lassise, R. Hoekstra, W. Ubachs, H. Gelderblom, and O. O. Versolato, "Plasma propulsion of a metallic microdroplet and its deformation upon laser impact", Phys. Rev. Appl. **6**, 014018 (2016).

[21]H. Gelderblom, H. Lhuissier, A. L. Klein, W. Bouwhuis, D. Lohse, E. Villermaux, and J. H. Snoeijer, "Drop deformation by laser-pulse impact", J. Fluid Mech. **794**, 676–699 (2016).

[22]D. Kurilovich, M. M. Basko, D. A. Kim, F. Torretti, R. Schupp, J. C. Visschers, J. Scheers, R. Hoekstra, W. Ubachs, and O. O. Versolato, "Power-law scaling of plasma pressure on laser-ablated tin microdroplets", Phys. Plasmas **25**, 012709 (2018).

[23]G. O'Sullivan, B. Li, R. D'Arcy, P. Dunne, P. Hayden, D. Kilbane, T. McCormack, H. Ohashi, F. O'Reilly, P. Sheridan, E. Sokell, C. Suzuki, and T. Higashiguchi, "Spectroscopy of highly charged ions and its relevance to EUV and soft x-ray source development", J. Phys. B **48**, 144025 (2015).

[24]A. Vinokhodov, M. Krivokorytov, Y. Sidelnikov, V. Krivtsun, V. Medvedev, V. Bushuev, K. Koshelev, D. Glushkov, and S. Ellwi, "Stable droplet generator for a high brightness laser produced plasma extreme ultraviolet source", Rev. Sci. Instrum. **87**, 103304 (2016).

[25]M. M. Basko, M. S. Krivokorytov, A. Y. Vinokhodov, Y. V. Sidelnikov, V. M. Krivtsun, V. V. Medvedev, D. A. Kim, V. O. Kompanets, A. A. Lash, and K. N. Koshelev, "Fragmentation dynamics of liquid–metal droplets under ultra-short laser pulses", Laser Phys. Lett. **14**, 036001 (2017).

[26]M. S. Krivokorytov, A. Y. Vinokhodov, Y. V. Sidelnikov, V. M. Krivtsun, V. O. Kompanets, A. A. Lash, K. N. Koshelev, and V. V. Medvedev, "Cavitation and spallation in liquid metal droplets produced by subpicosecond pulsed laser radiation", Phys. Rev. E **95**, 031101 (2017).

[27]M. S. Krivokorytov, Q. Zeng, B. V. Lakatosh, A. Y. Vinokhodov, Y. V. Sidelnikov, V. O. Kompanets, V. M. Krivtsun, K. N. Koshelev, C.-D. Ohl, and V. V. Medvedev, "Shaping and controlled fragmentation of liquid metal droplets through cavitation", Sci. Rep. **8**, 597 (2018).

[28]D. Kurilovich, T. de Faria Pinto, F. Torretti, R. Schupp, J. Scheers, A. S. Stodolna, H. Gelderblom, K. S. Eikema, S. Witte, W. Ubachs, R. Hoekstra, and O. O. Versolato, "Expansion Dynamics after Laser-Induced Cavitation in Liquid Tin Microdroplets", Phys. Rev. Appl. **10**, 054005 (2018).

[29]S. Y. Grigoryev, B. V. Lakatosh, M. S. Krivokorytov, V. V. Zhakhovsky, S. A. Dyachkov, D. K. Ilnitsky, K. P. Migdal, N. A. Inogamov, A. Y. Vinokhodov, V. O. Kompanets, Y. V. Sidelnikov, V. M. Krivtsun, K. N. Koshelev, and V. V. Medvedev, "Expansion and Fragmentation of a Liquid-Metal Droplet by a Short Laser Pulse", Phys. Rev. Appl. **10**, 064009 (2018).

[30]P. Koukouvinis, N. Kyriazis, and M. Gavaises, "Smoothed particle hydrodynamics simulation of a laser pulse impact onto a liquid metal droplet", PLoS One **13**, 1–13 (2018).

[31]A. L. Klein, W. Bouwhuis, C. W. Visser, H. Lhuissier, C. Sun, J. H. Snoeijer, E. Villermaux, D. Lohse, and H. Gelderblom, "Drop shaping by laser-pulse impact", Phys. Rev. Appl. **3**, 044018 (2015).

[32]M. M. Basko, J. A. Maruhn, and A. Tauschwitz, "An efficient cell-centered diffusion scheme for quadrilateral grids", J. Comput. Phys. **228**, 2175–2193 (2009).

[33]M. M. Basko, J. A. Maruhn, and A. Tauschwitz, *Development of a 2D radiation-hydrodynamics code RALEF for laser plasma simulations*, GSI Report 2010-1, PLASMA-PHYSICS-25 (GSI Helmholtzzentrum für Schwerionenforschung GmbH, 2010).

[34]D. T. Papageorgiou, "On the breakup of viscous liquid threads", Phys. Fluids **7**, 1529–1544 (1995).

[35]R. S. Abhari, B. Rollinger, A. Z. Giovannini, O. Morris, I. Henderson, and S. S. Ellwi, "Laser-produced plasma light source for extreme-ultraviolet lithography applications", J. Micro/Nanolith. MEMS MOEMS **11**, 021114–1 (2012).

[36]A. Y. Vinokhodov, M. S. Krivokorytov, Y. V. Sidelnikov, V. M. Krivtsun, V. V. Medvedev, and K. N. Koshelev, "Droplet-based, high-brightness extreme ultraviolet laser plasma source for metrology", J. Appl. Phys. **120**, 163304 (2016).

[37]A. S. Stodolna, T. de Faria Pinto, F. Ali, A. Bayerle, D. Kurilovich, J. Mathijssen, R. Hoekstra, O. O. Versolato, K. S. E. Eikema, and S. Witte, "Controlling ion kinetic energy distributions in laser produced plasma sources by means of a picosecond pulse pair", J. Appl. Phys. **124**, 053303 (2018).

[38]C. Hollingshead, M. Johnson, S. Barfuss, and R. Spall, "Discharge coefficient performance of Venturi, standard concentric orifice plate, V-cone and wedge flow meters at low Reynolds numbers", J. Pet. Sci. Eng. **78**, 559–566 (2011).

[39]E. Bassous, H. H. Taub, and L. Kuhn, "Ink jet printing nozzle arrays etched in silicon", Appl. Phys. Lett. **31**, 135–137 (1977).

[40]J. L. Dressler, "High-order azimuthal instabilities on a cylindrical liquid jet driven by temporal and spatial perturbations", Phys. Fluids **10**, 2212–2227 (1998).

[41]B. Rollinger, "Droplet target for laser-produced plasma light sources", PhD thesis (ETH Zurich, 2012).

[42]J. Benschop, V. Banine, S. Lok, and E. Loopstra, "Extreme ultraviolet lithography: Status and prospects", J. Vac. Sci. Technol. B **26**, 2204–2207 (2008).

[43]S. Fujioka, M. Shimomura, Y. Shimada, S. Maeda, H. Sakaguchi, Y. Nakai, T. Aota, H. Nishimura, N. Ozaki, A. Sunahara, K. Nishihara, N. Miyanaga, Y. Izawa, and K. Mima, "Pure-tin microdroplets irradiated with double laser pulses for efficient and minimum-mass extreme-ultraviolet light source production", Appl. Phys. Lett. **92**, 241502 (2008).

[44]K. Tomita, Y. Sato, K. Nishikawa, K. Uchino, T. Yanagida, H. Tomuro, Y. Wada, M. Kunishima, T. Kodama, H. Mizoguchi, and A. Sunahara, "Development of a collective Thomson scattering system for laser-produced tin plasmas for extreme-ultraviolet light sources", Appl. Phys. Express **8**, 126101 (2015).

[45]H. Mizoguchi, T. Abe, Y. Watanabe, T. Ishihara, T. Ohta, T. Hori, A. Kurosu, H. Komori, K. Kakizaki, A. Sumitani, O. Wakabayashi, H. Nakarai, J. Fujimoto, and A. Endo, "First generation laser-produced plasma source system for HVM EUV lithography", Proc. SPIE **7636**, 763608 (2010).

[46]R. W. Coons, S. S. Harilal, D. Campos, and A. Hassanein, "Analysis of atomic and ion debris features of laser-produced Sn and Li plasmas", J. Appl. Phys. **108**, 1–8 (2010).

[47]P. Mora, "Theoretical model of absorption of laser light by a plasma", Phys. Fluids **25**, 1051–1056 (1982).

[48]C. R. Phipps, T. P. Turner, R. F. Harrison, G. W. York, W. Z. Osborne, G. K. Anderson, X. F. Corlis, L. C. Haynes, H. S. Steele, K. C. Spicochi, and T. R. King, "Impulse coupling to targets in vacuum by KrF, HF, and CO_2 single-pulse lasers", J. Appl. Phys. **64**, 1083–1096 (1988).

[49]M. M. Basko, V. G. Novikov, and A. S. Grushin, "On the structure of quasi-stationary laser ablation fronts in strongly radiating plasmas", Phys. Plasmas **22**, 053111 (2015).

[50]R. Fabbro, C. Max, and E. Fabre, "Planar laser-driven ablation: Effect of inhibited electron thermal conduction", Phys. Fluids **28**, 1463 (1985).

[51]J. Pstruś, "Surface tension and density of liquid In-Sn-Zn alloys", Appl. Surf. Sci. **265**, 50–59 (2013).

[52]R. Fabbro, J. Fournier, P. Ballard, D. Devaux, and J. Virmont, "Physical study of laser-produced plasma in confined geometry", J. Appl. Phys. **68**, 775–784 (1990).

[53]J. R. Freeman, S. S. Harilal, B. Verhoff, A. Hassanein, and B. Rice, "Laser wavelength dependence on angular emission dynamics of Nd:YAG laser-produced Sn plasmas", Plasma Sources Sci. Technol. **21**, 055003 (2012).

[54]M. Masnavi, M. Nakajima, K. Horioka, H. P. Araghy, and A. Endo, "Simulation of particle velocity in a laser-produced tin plasma extreme ultraviolet source", J. Appl. Phys. **109**, 123306 (2011).

[55]S. S. Harilal, T. Sizyuk, A. Hassanein, D. Campos, P. Hough, and V. Sizyuk, "The effect of excitation wavelength on dynamics of laser-produced tin plasma", J. Appl. Phys. **109**, 063306 (2011).

[56]R. A. Burdt, S. Yuspeh, K. L. Sequoia, Y. Tao, M. S. Tillack, and F. Najmabadi, "Experimental scaling law for mass ablation rate from a Sn plasma generated by a 1064 nm laser", J. Appl. Phys. **106**, 033310 (2009).

[57]F. Dahmani and T. Kerdja, "Planar laser-driven ablation model for nonlocalized absorption", Phys. Fluids B **3**, 1232–1239 (1991).

[58]B. N. Chichkov, C. Momma, S. Nolte, F. von Alvensleben, and A. Tuennnermann, "Femtosecond, picosecond and nanosecond laser ablation of solids", Appl. Phys. A **63**, 109–115 (1996).

[59]E. G. Gamaly, A. V. Rode, B. Luther-Davies, and V. T. Tikhonchuk, "Ablation of solids by femtosecond lasers: Ablation mechanism and ablation thresholds for metals and dielectrics", Phys. Plasmas **9**, 949 (2002).

[60]S. V. Stankus, I. V. Savchenko, and A. S. Agazhanov, "Thermal Conductivity and Thermal Diffusivity of Liquid Indium–Tin Alloys", Int. J. Thermophys. **33**, 774–782 (2012).

[61]G. Cisneros, J. S. Helman, and C. N. J. Wagner, "Dielectric function of liquid tin between 250 and 1100°C", Phys. Rev. B **25**, 4248–4251 (1982).

[62]A. I. Golovashkin, I. S. Levchenko, G. P. Motulevich, and A. A. Shubin, "Optical properties of indium", Sov. Phys. JETP **24**, 1093–1100 (1967).

[63]E. G. Gamaly, "The physics of ultra-short laser interaction with solids at non-relativistic intensities", Phys. Rep. **508**, 91–243 (2011).

[64]S. Atzeni and J. Meyer-ter Vehn, *The physics of inertial fusion: beamplasma interaction, hydrodynamics, hot dense matter* (Oxford University Press on Demand, 2004).

[65]R. S. Craxton, K. S. Anderson, T. R. Boehly, V. N. Goncharov, D. R. Harding, J. P. Knauer, R. L. McCrory, P. W. McKenty, D. D. Meyerhofer, J. F. Myatt, A. J. Schmitt, J. D. Sethian, R. W. Short, S. Skupsky, W. Theobald, W. L. Kruer, K. Tanaka, R. Betti, T. J. B. Collins, J. A. Delettrez, S. X. Hu, J. A. Marozas, A. V. Maximov, D. T. Michel, P. B. Radha, S. P. Regan, T. C. Sangster, W. Seka, A. A. Solodov, J. M. Soures, C. Stoeckl, and J. D. Zuegel, "Direct-drive inertial confinement fusion: A review", Phys. Plasmas **22**, 110501 (2015).

[66]R. Betti and O. Hurricane, "Inertial-confinement fusion with lasers", Nat. Phys. **12**, 435–448 (2016).

[67]C. Phipps, ed., *Laser ablation and its applications*, 1st ed., Vol. 129, Springer Series in Optical Sciences (Springer, 2007).

[68]C. Phipps, M. Birkan, W. Bohn, H.-A. Eckel, H. Horisawa, T. Lippert, M. Michaelis, Y. Rezunkov, A. Sasoh, W. Schall, S. Scharring, and J. Sinko, "Review: laser-ablation propulsion", J. Propul. Power **26**, 609–637 (2010).

[69]H. Mizoguchi, H. Nakarai, T. Abe, K. M. Nowak, Y. Kawasuji, H. Tanaka, Y. Watanabe, T. Hori, T. Kodama, Y. Shiraishi, T. Yanagida, T. Yamada, T. Yamazaki, S. Okazaki, and T. Saitou, "Development of 250 W EUV light source for HVM lithography", Proc. SPIE **10097**, 1009702 (2017).

[70]D. Hudgins, N. Gambino, B. Rollinger, and R. Abhari, "Neutral cluster debris dynamics in droplet-based laser-produced plasma sources", J. Phys. D **49**, 185205 (2016).

[71]R. Kidder, "Application of lasers to the production of high-temperature and high-pressure plasma", Nucl. Fusion **8**, 3 (1968).

[72]Y. V. Afanas'ev and O. N. Krokhin, "Gas-dynamical theory of the effect of laser radiation on condensed substances", in *Quantum electronics in lasers and masers: part 2*, edited by D. V. Skobel'tsyn (Springer US, Boston, MA, 1972), pp. 109–155.

[73]Y. V. Afanas'ev, E. G. Gamalii, O. N. Krokhin, and V. B. Rozanov, "Stationary model of the "corona" of spherical laser targets", Sov. Phys. JETP **44**, 311–316 (1976).

[74]W. M. Manheimer, D. G. Colombant, and J. H. Gardner, "Steady-state planar ablative flow", Phys. Fluids **25**, 1644–1652 (1982).

[75]P. Mulser and D. Bauer, *High power laser-matter interaction*, Vol. 238, Springer Tracts in Modern Physics (Springer, 2010).

[76]L. Zhou, X.-Y. Li, W.-J. Zhu, J.-X. Wang, and C.-J. Tang, "The effects of pulse duration on ablation pressure driven by laser radiation", J. Appl. Phys. **117**, 125904 (2015).

[77]M. M. Basko, V. G. Novikov, and A. S. Grushin, "Radiation hydrodynamics of tin targets for laser-plasma EUV sources", in 2014 International Workshop on EUV and Soft X-Ray Sources (Dublin, November 3-6, 2014).

[78]M. M. Basko, "On the maximum conversion efficiency into the 13.5-nm extreme ultraviolet emission under a steady-state laser ablation of tin microspheres", Phys. Plasmas **23**, 083114 (2016).

[79]F. L. Addessio, J. R. Baumgardner, J. K. Dukowicz, N. L. Johnson, B. A. Kashiwa, R. M. Rauenzahn, and C. Zemach, *CAVEAT: A Computer Code for Fluid Dynamics Problems With Large Distortion and Internal Slip*, Report LA-10613-MS-Rev. 1, UC-32 (Los Alamos National Laboratory, 1992).

[80]E. Livne and A. Glasner, "A finite difference scheme for the heat conduction equation", J. Comput. Phys. **58**, 59–66 (1985).

[81]A. Dedner and P. Vollmöller, "An Adaptive Higher Order Method for Solving the Radiation Transport Equation on Unstructured Grids", J. Comput. Phys. **178**, 263–289 (2002).

[82]S. Faik, M. M. Basko, A. Tauschwitz, I. Iosilevskiy, and J. A. Maruhn, "Dynamics of volumetrically heated matter passing through the liquid–vapor metastable states", High. Energ. Dens. Phys. **8**, 349–359 (2012).

[83]M. Basko, T. Löwer, V. N. Kondrashov, A. Kendl, R. Sigel, and J. Meyer-ter Vehn, "Optical probing of laser-induced indirectly driven shock waves in aluminum", Phys. Rev. E **56**, 1019–1031 (1997).

[84]M. M. Basko and I. P. Tsygvintsev, "A hybrid model of laser energy deposition for multi-dimensional simulations of plasmas and metals", Comput. Phys. Commun. **214**, 59 –70 (2017).

[85]H. Kull, "Theory of the Rayleigh-Taylor instability", Phys. Rep. **206**, 197 –325 (1991).

[86]I. V. Nemchinov, "Steady-state motion of radiation-heated vapors of a material in the presence of lateral spreading flow", J. Appl. Math. Mech. **31**, 320–339 (1967).

[87]N. G. Basov, V. A. Gribkov, O. N. Krokhin, and G. V. Sklizkov, "High temperature effects of intense laser emission focused on a solid target", Sov. Phys. JETP **27**, 575–582 (1968).

[88]A. Caruso and R. Gratton, "Some properties of the plasmas produced by irradiating light solids by laser pulses", Plasma Phys. **10**, 867 (1968).

[89]T. J. Goldsack, J. D. Kilkenny, B. J. MacGowan, P. F. Cunningham, C. L. S. Lewis, M. H. Key, and P. T. Rumsby, "Evidence for large heat fluxes from the mass ablation rate of laser-irradiated spherical targets", Phys. Fluids **25**, 1634–1643 (1982).

[90]A. Maaswinkel, K. Eidmann, R. Sigel, and S. Witkowski, "Comparative study of laser acceleration of thin foils at wavelengths 0.44 μm and 1.3 μm", Opt. Commun. **51**, 255–259 (1984).

[91]K. Eidmann, F. Amiranoff, R. Fedosejevs, A. G. M. Maaswinkel, R. Petsch, R. Sigel, G. Spindler, Y.-l. Teng, G. Tsakiris, and S. Witkowski, "Interaction of 1.3-μm laser radiation with thin foil targets", Phys. Rev. A **30**, 2568–2589 (1984).

[92]F. Dahmani, "Ablation scaling in laser-produced plasmas with laser intensity, laser wavelength, and target atomic number", Phys. Fluids B **4**, 1585–1588 (1992).

[93]F. Dahmani, "Experimental scaling laws for mass-ablation rate, ablation pressure in planar laser-produced plasmas with laser intensity, laser wavelength, and target atomic number", J. Appl. Phys. **74**, 622–634 (1993).

[94]D. Nakamura, T. Akiyama, K. Okazaki, K. Tamaru, A. Takahashi, and T. Okada, "Ablation dynamics of tin micro-droplet irradiated by double pulse laser used for extreme ultraviolet lithography source", J. Phys. D: Appl. Phys. **41**, 245210 (2008).

[95]I. P. Tsygvintsev, A. Y. Krukovskiy, and V. G. Novikov, "3D simulation of shifted laser pulse coupling to tin target", in 2014 International Workshop on EUV and Soft X-Ray Sources (Nov. 2014).

[96]A. Hassanein, V. Sizyuk, and T. Sizyuk, "The effect of critical plasma densities of laser-produced plasma on production of extreme ultraviolet radiation", IEEE Trans. Plasma Sci. **39**, 2810–2811 (2011).

[97]T. Sizyuk and A. Hassanein, "The role of plasma evolution and photon transport in optimizing future advanced lithography sources", J. Appl. Phys. **114**, 083109 (2013).

[98]R. Rafac, R. Sandstrom, D. Brown, and K. Hou, "Extreme ultraviolet light source", Patent US 9232623 (US) (2016), US Patent 9,232,623.

[99]Wolfram Research INC., *Mathematica 11.1.* 2017.

[100]B. V. Lakatosh, D. B. Abramenko, V. V. Ivanov, V. V. Medvedev, V. M. Krivtsun, K. N. Koshelev, and A. M. Yakunin, "Propulsion of a flat tin target with pulsed CO_2 laser radiation: measurements using a ballistic pendulum", Laser Phys. Lett. **15**, 016003 (2018).

[101]E. Villermaux and B. Bossa, "Drop fragmentation on impact", J. Fluid Mech. **668**, 412–435 (2011).

[102]N. Bremond and E. Villermaux, "Bursting thin liquid films", J. Fluid Mech. **524**, 121–130 (2005).

[103]P.-G. de Gennes, F. Brochard-Wyart, and D. Quéré, *Capillarity and Wetting Phenomena: Drops, Bubbles, Pearls, Waves* (Springer, New York, 2002).

[104]N. Bremond and E. Villermaux, "Atomization by jet impact", J. Fluid Mech. **549**, 273–306 (2006).

[105]J. Eggers and E. Villermaux, "Physics of liquid jets", Rep. Prog. Phys. **71**, 036601 (2008).

[106]H. Lhuissier and E. Villermaux, "'Effervescent' Atomization in Two Dimensions", J. Fluid Mech. **714**, 361–392 (2013).

[107]A. L. Klein, D. Lohse, M. Versluis, and H. Gelderblom, "Apparatus to control and visualize the impact of a high-energy laser pulse on a liquid target", Rev.Sci. Instrum. **88**, 095102 (2017).

[108]A. van der Bos, A. Zijlstra, E. Gelderblom, and M. Versluis, "iLIF: illumination by Laser-Induced Fluorescence for single flash imaging on a nanoseconds timescale", Exp. Fluids **51**, 1283–1289 (2011).

[109]M. Versluis, "High-speed imaging in fluids", Exp. Fluids **54**, 1458 (2013).

[110]E. Hecht, *Optics* (Addison-Wesley, New York, 2002).

[111]I. R. Peters, Y. Tagawa, N. Oudalov, C. Sun, A. Prosperetti, D. Lohse, and D. van der Meer, "Highly focused supersonic microjets: numerical simulations", J. Fluid Mech. **719**, 587–605 (2013).

[112]S. T. Thoroddsen, K. Takehara, T. Etoh, and C.-D. Ohl, "Spray and microjets produced by focusing a laser pulse into a hemispherical drop", Phys. Fluids **21**, 112101 (2009).

[113]Y. Utsunomiya, T. Kajiwara, T. Nishiyama, K. Nagayama, S. Kubota, and M. Nakahara, "Laser ablation of liquid surface in air induced by laser irradiation through liquid medium", Appl. Phys. A **101**, 137–141 (2010).

[114]Y. Tagawa, N. Oudalov, C. W. Visser, I. R. Peters, D. van der Meer, C. Sun, A. Prosperetti, and D. Lohse, "Highly Focused Supersonic Microjets", Phys. Rev. X **2**, 031002 (2012).

[115]S. R. Gonzalez Avila and C.-D. Ohl, "Cavitation-induced fragmentation of an acoustically-levitated droplet", J. Phys. Conf. Ser. **656**, 012017 (2015).

[116]S. A. Reijers, J. H. Snoeijer, and H. Gelderblom, "Droplet deformation by short laser-induced pressure pulses", J. Fluid Mech. **828**, 374–394 (2017).

[117]A. Vogel and V. Venugopalan, "Mechanisms of Pulsed Laser Ablation of Biological Tissues", Chem. Rev. **103**, 577–644 (2003).

[118]M. W. Sigrist and F. K. Kneubühl, "Laser-generated stress waves in liquids", J. Acoust. Soc. Am. **64**, 1652–1663 (1978).

[119]X. Wang and X. Xu, "Thermoelastic wave induced by pulsed laser heating:" Appl. Phys. A **73**, 107–114 (2001).

[120]A. H. Clauer, J. H. Holbrook, and B. P. Fairand, "Effects of laser induced shock waves on metals", in *Shock waves and high-strain-rate phenomena in metals* (Springer, Boston, MA, 1981), pp. 675–702.

[121]A. M. Marpaung, H. Kurniawan, M. O. Tjia, and K. Kagawa, "Comprehensive study on the pressure dependence of shock wave plasma generation under TEA CO_2 laser bombardment on metal sample", J. Phys. D **34**, 758–771 (2001).

[122]C. Vernay, L. Ramos, and C. Ligoure, "Free radially expanding liquid sheet in air: time- and space-resolved measurement of the thickness field", J. Fluid Mech. **764**, 428–444 (2015).

[123]F. E. C. Culick, "Comments on a Ruptured Soap Film", J. Appl. Phys. **31**, 1128–1129 (1960).

[124]A. Oron, S. H. Davis, and S. G. Bankoff, "Long-scale evolution of thin liquid films", Rev. Mod. Phys. **69**, 931–980 (1997).

[125]J. B. Keller and I. Kolodner, "Instability of liquid surfaces and the formation of drops", J. Appl. Phys. **25**, 918–921 (1954).

[126]A. Braslau, "Surface Roughness of Water Measured by X-Ray Reflectivity", Phys. Rev. Lett. **54**, 114–117 (1985).

[127]E. Villermaux, "Fragmentation", Annu. Rev. Fluid Mech. **39**, 419–446 (2007).

[128]H.-R. Kuhn, J. Koch, R. Hergenröder, K. Niemax, M. Kalberer, and D. Günther, "Evaluation of different techniques for particle size distribution measurements on laser-generated aerosols", J. Anal. At. Spectrom. **20**, 894–900 (2005).

[129]C. A. Stan, D. Milathianaki, H. Laksmono, R. G. Sierra, T. A. McQueen, M. Messerschmidt, G. J. Williams, J. E. Koglin, T. J. Lane, M. J. Hayes, S. A. H. Guillet, M. Liang, A. L. Aquila, P. R. Willmott, J. S. Robinson, K. L. Gumerlock, S. Botha, K. Nass, I. Schlichting, R. L. Shoeman, H. A. Stone, and S. Boutet, "Liquid explosions induced by X-ray laser pulses", Nat. Phys. **12**, 966–971 (2016).

[130]C. A. Stan, P. R. Willmott, H. A. Stone, J. E. Koglin, M. Liang, A. L. Aquila, J. S. Robinson, K. L. Gumerlock, G. Blaj, R. G. Sierra, S. Boutet, S. A. H. Guillet, R. H. Curtis, S. L. Vetter, H. Loos, J. L. Turner, and F.-J. Decker, "Negative pressures and spallation in water drops subjected to nanosecond shock waves", J. Phys. Chem. Lett. **7**, 2055–2062 (2016).

[131]A. Pirati, J. van Schoot, K. Troost, R. van Ballegoij, P. Krabbendam, J. Stoeldraijer, E. Loopstra, J. Benschop, J. Finders, H. Meiling, E. van Setten, N. Mika, J. Dredonx, U. Stamm, B. Kneer, B. Thuering, W. Kaiser, T. Heil, and S. Migura, "The future of EUV lithography: enabling Moore's Law in the next decade", Proc. SPIE **10143**, 101430G (2017).

[132]See Supplemental Material at `http://link.aps.org/supplemental/10.1103/PhysRevApplied.10.054005` for stroboscopic shadowgraphy movies.

[133]K. Sokolowski-Tinten, J. Bialkowski, A. Cavalleri, D. von der Linde, A. Oparin, J. Meyer-ter-Vehn, and S. I. Anisimov, "Transient states of matter during short pulse laser ablation", Phys. Rev. Lett. **81**, 224–227 (1998).

[134]D. von der Linde and K. Sokolowski-Tinten, "The physical mechanisms of short-pulse laser ablation", Appl. Surf. Sci. **154–155**, 1–10 (2000).

[135]S. R. Gonzalez-Avila, E. Klaseboer, B. C. Khoo, and C.-D. Ohl, "Cavitation bubble dynamics in a liquid gap of variable height", J. Fluid Mech. **682**, 241–260 (2011).

[136]K. Eidmann, J. Meyer-ter-Vehn, T. Schlegel, and S. Hüller, "Hydrodynamic simulation of subpicosecond laser interaction with solid-density matter", Phys. Rev. E **62**, 1202–1214 (2000).

[137]A. Vledouts, J. Quinard, N. Vandenberghe, and E. Villermaux, "Explosive fragmentation of liquid shells", J. Fluid Mech. **788**, 246–273 (2016).

[138]S. Chandrasekhar, *Hydrodynamic and hydromagnetic stability* (Oxford University Press, 1961).

[139]A. L. Klein, "Laser impact on flying drops", PhD thesis (University of Twente, June 2017).

List of Publications

Chapter 3:
D. Kurilovich, A. L. Klein, F. Torretti, A. Lassise, R. Hoekstra, W. Ubachs, H. Gelderblom, and O. O. Versolato, "Plasma propulsion of a metallic microdroplet and its deformation upon laser Impact," Phys. Rev. Appl. **6**, 014018 (2016).

Chapter 4:
D. Kurilovich, M. M. Basko, D. A. Kim, F. Torretti, R. Schupp, J. C. Visschers, J. Scheers, R. Hoekstra, W. Ubachs, and O. O. Versolato, "Power-law scaling of plasma pressure on laser-ablated tin microdroplets," Phys. Plasmas **25**, 012709 (2018).

Chapter 5:
S. A. Reijers, D. Kurilovich, F. Torretti, H. Gelderblom, and O. O. Versolato, "Laser-to-droplet alignment sensitivity relevant for laser-produced plasma sources of extreme ultraviolet light," J. Appl. Phys. **124**, 013102 (2018).

Chapter 6:
A. L. Klein, D. Kurilovich, H. Lhuissier, O. O. Versolato, D. Lohse, E. Villermaux, and H. Gelderblom, "Fragmentation of free-falling drops by laser-pulse impact," to be submitted.

Chapter 7:
D. Kurilovich, T. de F. Pinto, F. Torretti, R. Schupp, J. Scheers, A. S. Stodolna, H. Gelderblom, K. S. E. Eikema, S. Witte, W. Ubachs, R. Hoekstra, and O. O. Versolato, "Expansion dynamics after laser-induced cavitation in liquid tin microdroplets," Phys. Rev. Appl. **10**, 054005 (2018).

The author also contributed to the following publications:

1. R. Schupp, F. Torretti, R. A. Meijer, M. Bayraktar, J. Scheers, D. Kurilovich, A. Bayerle, K. S. E. Eikema, S. Witte, W. Ubachs, R. Hoekstra, and O. O. Versolato, "Efficient generation of extreme ultraviolet light from Nd:YAG-driven microdroplet-tin plasma," submitted (2018)

2. J. Scheers, A. Ryabtsev, A. Borschevsky, J. C. Berengut, K. Haris, R. Schupp, D. Kurilovich, F. Torretti, A. Bayerle, E. Eliav, W. Ubachs, O. O. Versolato, and R. Hoekstra, "Energy Level Structure of Sn^{3+} Ions," Phys. Rev. A **98**, 062503 (2018)

3. A. S. Stodolna, T. de Faria Pinto, F. Ali, A. Bayerle, D. Kurilovich, J. Mathijssen, R. Hoekstra, O. O. Versolato, K. S. E. Eikema, and S. Witte, "Controlling ion kinetic energy distributions in laser produced plasma sources by means of a picosecond pulse pair," J. Appl. Phys. **124**, 053303 (2018).

4. A. Bayerle, M. J. Deuzeman, S. van der Heijden, D. Kurilovich, T. de F. Pinto, A. Stodolna, S. Witte, K. S. E. Eikema, W. Ubachs, R. Hoekstra, and O. O. Versolato, "Sn ion energy distributions of ns- and ps-laser produced plasmas," Plasma Sources Sci. Technol. **27**, 045001 (2018).

5. F. Torretti, R. Schupp, D. Kurilovich, A. Bayerle, J. Scheers, W. Ubachs, R. Hoekstra, and O. O. Versolato, "Short-wavelength out-of-band EUV emission from Sn laser-produced plasma," J. Phys. B At. Mol. Opt. Phys. **51**, 045005 (2018).

Patent applications:

1. D. Kurilovich, O. O. Versolato, T. de Faria Pinto, S. Witte, "Radiation Source," ASML, Feb. 2018.

Acknowledgements

First of all, I would like to express my gratitude to my supervisors: Wim Ubachs, Ronnie Hoekstra, and Oscar Versolato, for the given opportunity to be the first PhD student in their EUV Plasma Processes group (EUV Plasma Dynamics, at that moment) at the Advanced Research Center for Nanolithography (ARCNL) in Amsterdam. I am extremely grateful for their guidance, help, and particular attention to the project. They encouraged me to broaden my scope by attending multiple conferences and summer schools. It was a great fortune to have such supervisors and I am looking forward to our new collaboration.

I had the pleasure to see how ARCNL grew over these four years. I would like to thank my colleagues, with whom we spent a lot of time in the lab and the office, went through our exhausting 'beamtimes' together, visited numerous conferences, and just had fun. I thank my colleagues in Amsterdam: Francesco Torretti, Joris Scheers, Ruben Schupp, Alex Bayerle, Jim Visschers, Tiago de Faria Pinto, Randy Meijer, Aneta Stodolna, Pavel Antonov, Laurens van Buuren, Bo Liu, Zoi Bouza, and the Groningen part of our group: Mart Johan Deuzeman and Subam Rai. It was always a great pleasure to spend time together. I would like to give special thanks to Francesco and Joris for agreeing to be my paranymphs and supporting me at the frontline of my defense.

I would like to thank Thomas Cohen Stuart, the group's technician, and Adam Lassise, researcher from ASML, who worked with me at the start of the project, for their assistance and for their knowledge that was particularly helpful in building the new setup and learning new techniques. Further, I would like to express my gratitude to the professionals from Mechanical Engineering, Precision Manufacturing, Electronics Engineering, Software Engineering, and ICT departments of AMOLF for their enduring technical support.

Collaborations with other research groups were vital for my project. Almost every chapter of this thesis reflects our work with the Physics of Fluids group of University of Twente. I would like to thank Hanneke Gelderblom, Alexander Klein, and Sten Reijers for our multiple discussions that resulted in several publications.

I would like to thank Mikhail M. Basko and Dmitrii A. Kim from Keldysh Institute of Applied Mathematics in Moscow for bringing their expertise to our work on the plasma propulsion. It was a great pleasure to work together.

The collaboration with the EUV Generation and Imaging group of ARCNL included our experiments with the custom-built picosecond laser system, as described in this thesis, and many more interesting physical observations that will be described elsewhere. For this, I thank Tiago de Faria Pinto, Randy Meijer, Aneta Stodolna, Stefan Witte, and Kjeld Eikema.

I highly acknowledge the support and inspiration from ASML, the industrial partner of ARCNL. Throughout the whole project I was lucky to communicate with scientists and engineers from ASML. Particularly, I would like to thank Wim van der Zande, Igor Fomenkov, Deniz van Heijnsbergen, Yezheng Tao, Rob Rafac, Alex Schafgans, Adam Lassise, Harry Kreuwel, Maarten van Kampen, Andrei Yakunin, and others, for their interest in my research and for sharing their knowledge. I thank the Technology Development of ASML/Cymer for hosting me for two weeks during the last year of my PhD.

I am grateful to my family, whose endless love and support, no matter where we were located on the map, helped me to start and complete this project.

For her love, continuous support and patience, for proofreading, I would like to thank Judith van Santen.

Dmitry Kurilovich
Amsterdam, 2018

This work aims to advance the understanding of the underlying physics of the laser target formation in state-of-the-art and future laser-produced plasma sources of extreme ultraviolet (EUV) light.

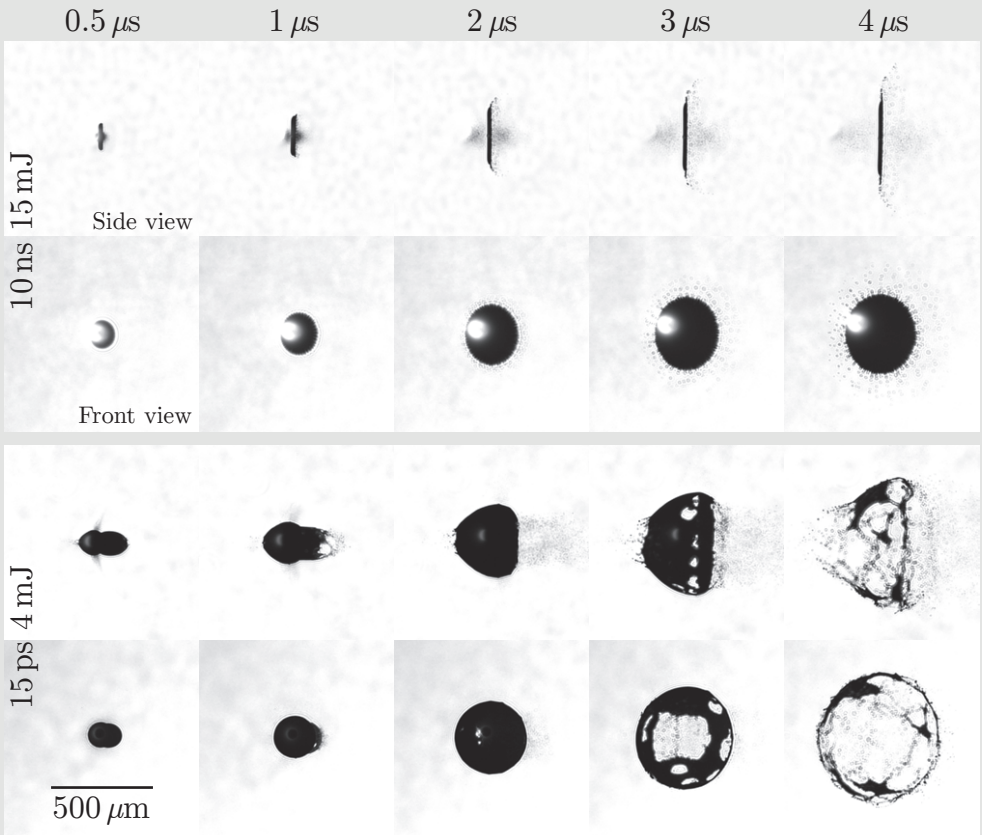

ARCNL

ADVANCED RESEARCH CENTER FOR NANOLITHOGRAPHY